

Finite temperature study of strongly correlated systems

By

Gour Jana

Enrolment No: PHYS11201504014

National Institute of Science Education and Research,
Bhubaneswar

*A thesis submitted to the
Board of Studies in Physical Sciences*

*In partial fulfillment of requirements
for the Degree of*

DOCTOR OF PHILOSOPHY

of

HOMI BHABHA NATIONAL INSTITUTE



December, 2021

Homi Bhabha National Institute

Recommendations of the Viva Voce Committee

As members of the Viva Voce Committee, we certify that we have read the dissertation prepared by **Gour Jana** entitled "Finite temperature study of strongly correlated systems" and recommend that it may be accepted as fulfilling the thesis requirement for the award of Degree of Doctor of Philosophy.

Chairman - Prof. Bedangadas Mohanty

Bedangadas Mohanty

Date

12/06/2022

Guide/Convener - Dr. Anamitra Mukherjee

Anamitra Mukherjee

Date

12/06/2022

Co-guide - (if any)

Date

Examiner- Prof. Sanjeev Kumar

Sanjeev Kumar

Date

Member 1- Prof. Pinaki Majumdar

Pinaki Majumdar

Date

Member 2- Dr. V. Ravi Chandra

V. Ravi Chandra

Date

09-06-22

Member 3- Dr. Sumedha

Sumedha

Date

11-06-22

Final approval and acceptance of this thesis is contingent upon the candidate's submission of the final copies of the thesis to HBNI.

I/We hereby certify that I/we have read this thesis prepared under my/our direction and recommend that it may be accepted as fulfilling the thesis requirement

Date: 12.06.2022

Place: NISER,
BHUBANESWAR Co-guide(if applicable)

Signature
Guide

A level
12/06/2022

STATEMENT BY AUTHOR

This dissertation has been submitted in partial fulfillment of requirements for an advanced degree at Homi Bhabha National Institute (HBNI) and is deposited in the Library to be made available to borrowers under rules of the HBNI.

Brief quotations from this dissertation are allowable without special permission, provided that accurate acknowledgement of source is made. Requests for permission for extended quotation from or reproduction of this manuscript in whole or in part may be granted by the Competent Authority of HBNI when in his or her judgment the proposed use of the material is in the interests of scholarship. In all other instances, however, permission must be obtained from the author.

Gour Jana

Signature

Gour Jana

DECLARATION

I, hereby declare that the investigation presented in the thesis has been carried out by me. The work is original and has not been submitted earlier as a whole or in part for a degree / diploma at this or any other Institution / University.

Gour Jana
Signature

Gour Jana

List of Publications arising from the thesis

Journal

Published:

1. *Frustration effects at finite temperature in the half filled Hubbard model, **Gour Jana** and Anamitra Mukherjee, J. Phys.: Condens. Matter **32** 365602 (2020)
2. *Emergent Half Metal at Finite Temperatures in a Mott Insulator, **Gour Jana**, Abhishek Joshi, Subhajyoti Pal, and Anamitra Mukherjee, Communications Physics **5**, 66 (2022)

Other Publications:

1. Intrinsic ferromagnetism in atomically thin two-dimensional organic-inorganic van der Waals crystals, Dipayan Sen, **Gour Jana**, Nitin Kaushal, Anamitra Mukherjee, Tanusri Saha-Dasgupta, Phys. Rev. B **102**, 054411 (2020)

Manuscript under preparation:

1. Interaction driven topological phase transition in the frustrated Lieb lattice, Sayan Jana, **Gour Jana**, Arijit Saha, Anamitra Mukherjee

*: Publications related to the thesis

Conference

1. **Gour Jana**, Discussion Meeting on Nonequilibrium Quantum Many-Body Physics, Harish-Chandra Research Institute (HRI), Allahabad, UP, India Nov. 21-25, 2016

2. **Gour Jana**, Young Investigator Meet On Quantum Condensed Matter Theory (YIMQCMT) S. N. Bose National Centre for Basic Sciences, Kolkata, WB, India Oct. 26-27, 2017

(Presented a poster, Title : "FINITE TEMPERATURE STUDY OF $t - t'$ HUB-

BARD MODEL AT HALF FILLING”)

3. **Gour Jana**, Young Investigator Meet On Quantum Condensed Matter Theory (YIMQCMT 2018) S. N. Bose National Centre for Basic Sciences, Kolkata, WB, India Nov. 20-22, 2018

(Presented a poster, Title : ”Magnetism, nematicity, pseudogap and Fermi liquid to non-Fermi liquid metal crossover in the $t - t'$ Hubbard model”)

4. **Gour Jana**, National Conference On Quantum Condensed Matter (QMAT), Indian Institute of Science Education and Research (IISER), Mohali, Punjab, India July 25-27, 2018

(Presented a poster, Title : ”Magnetism and non-Fermi liquid metal in the $t - t'$ Hubbard model: A Monte Carlo Mean-Field study ”)

5. **Gour Jana**, Mini-school on ”Topology and Interactions in Quantum Matter”, Indian Institute of Science Education and Research (IISER) Kolkata, WB, India Jan. 08-10, 2018

6. **Gour Jana**, National Conference On Quantum Condensed Matter (QMAT), Indian Institute of Science (IISc), Bangalore, India July 8-10, 2019

(Presented a poster, title: ”Mean Field-Monte Carlo study of half-filled ionic Hubbard model on 2D square and 3D cubic lattice”)

7. **Gour Jana**, Young Investigator Meet On Quantum Condensed Matter Theory (YIMQCMT 2020) National Institute of Science Education and Research (NISER), Bhubaneswar, Odisha, India Dec. 15-18, 2020

(Gave a talk, title: ”Half metallicity at finite temperature in a Mott insulator”)

8. **Gour Jana**, Young Investigator Meet On Quantum Condensed Matter Theory (YIMQCMT 2021) National Institute of Science Education and Research

(NISER), Bhubaneswar, Odisha, India

Nov. 16-19, 2021

(Presented a poster, title: "Emergent half-metal at Finite Temperatures in a Mott Insulator ")

Gour Jana
Signature

Gour Jana

DEDICATIONS

Dedicated to

My Family and Teachers

ACKNOWLEDGEMENTS

Completing Ph.D. is one of the precious achievements and exhilarating tasks of my life. It wouldn't have been possible without the ceaseless support and immeasurable help from a number of persons. I would like to note down my deep sense of gratitude to all of them, here. First and foremost, I am very much indebted to my Ph.D. supervisor Dr. Anamitra Mukherjee for his guidance and suggestions throughout this thesis work.

And, I want to express my profound gratitude to my doctoral committee members Prof. Bedangadas Mohanty, Prof. Pinaki Majumdar, Dr. V. Ravi Chandra and Dr. Sumedha for their valuable suggestions and critical analysis during the evaluation meetings.

I would like to offer my heartfelt gratitude to my teachers Dr. Tarun Kanti De and Dr. Pradipta Panchadhyayee for their continuous encouragement and support.

I am also thankful to my seniors Rita, Joydev, Subrata, Abhishek, Sanjukta and Abhilash for their help in academic and non-academic matters. I had great time with my friends Chandni, Jyothis, Sujith, Prabhakar and many others chatting over various topics, both Physics and others.

I am highly indebted to each and every family member for their never ending support at every step of my life.

Contents

Title page	i
SUMMARY	xxi
List of Figures	xxix
1 Introduction	1
1.1 Basics of Fermi liquid theory	6
1.1.1 Adiabaticity	6
1.1.2 Quasi-particle excitation and its lifetime	7
1.2 Hubbard model	8
1.2.1 Limiting cases of Hubbard model	9
1.3 Role of longer range hopping	11
1.4 Staggered potential in the $t - t'$ Hubbard model	17
2 Model and Numerical Methods	23
2.1 Inhomogeneous Mean Field theory	27
2.2 Semi classical Monte-Carlo Technique	28
2.2.1 Derivation of H_{eff} in the semi-classical approach	28
2.2.2 Details of the Monte-Carlo procedure	30
2.2.3 Travelling cluster approximation:	35
2.2.4 Benchmarks for s-MC	36

3 Frustration and temperature effects at half filling	39
3.1 Introduction	39
3.2 $t - t'$ Hubbard model	40
3.3 Emergent phases at low temperature	40
3.3.1 Description of the phase diagram	42
3.4 Magnetic phases at finite temperatures	43
3.5 Frustration induced phase transitions	46
3.5.1 Re-entrant metal-insulator transition at low T	46
3.5.2 Metal-insulator transition at finite T	48
3.5.3 Nature of the metal at finite T	52
3.5.4 Pseudogapped metal at $T = 0$	53
3.6 Conclusions	54
4 Temperature driven half metal from a Mott Insulator	57
4.1 Introduction	57
4.2 $t - t'$ Ionic Hubbard model	59
4.3 Transport response	59
4.3.1 Band insulator	59
4.3.2 Mott insulator	60
4.3.3 Low T half-meta	61
4.3.4 Finite-temperature half metal	63
4.4 Magnetism & metallicity	66
4.5 Phase diagrams	68
4.6 Candidates for experimental realization	71
4.7 Conclusions	73
A Appendix A: Momentum space mean-field theory	75
B Appendix B: Slater insulator at weak coupling	77
C Appendix C: Strong coupling Heisenberg limit	81

D Appendix D: Inhomogeneous mean-field theory	87
E Appendix E: Definitions of indicators	89
References	93

SUMMARY

Complex phenomena caused by collective excitations of interacting quantum degrees of freedom is at the heart of many non-trivial phenomena. In order to understand correlated materials and their applications, many-particle quantum mechanics is the standard paradigm. The Hubbard model is the simplest model that involves local electron interaction or correlation effects and has been investigated by a variety of tools. A common open issue is reliable study of finite temperature properties on large system sizes. In this thesis we present results of a recently developed semi-classical Monte-Carlo (s-MC) approach well suited to study finite temperature properties of the Hubbard model. We focus on two main problems: (i) effect of next nearest neighbor hopping (t') on the magnetic insulator in the half-filled Hubbard model at finite temperature (ii) thermal evolution of metals and insulators in the $t - t'$ 'ionic' Hubbard model – the Hubbard model in presence of staggered onsite potentials, at half filling.

Effect of longer range hopping in the half-filled Hubbard model

At half filling, the Hubbard model on a square lattice with a interaction strength U and nearest neighbor hopping parameter t , has a nesting-instability driven anti-ferromagnetic (Slater) insulator at small U and Mott insulator at large U due to strong suppression of double occupation. The ground state has long-range staggered (G-type) magnetic correlations and a finite charge gap for all U values. In this project [1] we investigate the effect of next nearest neighbor hopping t' , on the insulating phases over a wide temperature range. The motivation for looking into effects of longer range hopping is as follows: Particle-hole symmetry is broken by t' , weakening the nesting instability. Even for small t' , the small U Slater insulator

is likely to be destabilized. At large U , we expect t' to produce frustrated antiferromagnetic exchange couplings that suppress the G-type magnetic order. Our goal was to identify the phases arising out of the frustration effects induced by t' and investigate their thermal evolution. Using the s-MC approach, we determine the static magnetic structure factor, density of states, optical conductivity, and resistivity as a function of temperature. From these observables, we generate the interaction (U)-temperature (T)-frustration (t') phase diagram for the model.

i) Low-temperature properties: We find that t' destabilizes the Slater insulator at low U and prefers the paramagnetic metal below a t' dependent critical U . A G-type to A-type $[(\pi, 0)/(0, \pi)]$ magnetic transition is seen at $t' = 0.8t$ for large U . The locus of critical U for metal-to-insulator transition in the $U - t'$ plane is found to be non-monotonic in t' , with maximum critical U occurring at $t' = -0.8t$. Due to G-type/A-type phase competition, the magnetic and insulating order is weakened, necessitating the largest critical U for metal to insulator transition at $t' = -0.8t$. From this data, we construct a low temperature s-MC $U - t'$ phase diagram. We note that at low-temperature, s-MC tends to an unrestricted Hartree-Fock mean-field theory. Within this approximation, we find that the magnetic and metal-insulator boundaries reasonably agree with the literature as discussed in the thesis.

ii) Finite-temperature evolution: Next, we analyze the temperature evolution of the observables and metal-insulator transitions at finite temperature. In the Mott insulating phase, the magnetic transition temperature for G-type order (for $t'/t > -0.8$) and A-type order (for $t'/t < -0.8$) show a non-monotonic dependence on U . This trend agrees with DQMC results as shown in the thesis. We then investigate the nature of the metallic phase at finite temperature. We calculate transport properties within the Kubo-Greenwood formalism and construct $T - t'$ phase diagram at fixed U from this analysis. We find that for small $U \sim 4t$, the insulator at $t'=0$ weakens, with the critical temperature for the insulator to metal

transition monotonically decreasing with t' and eventually leads to a metallic phase. In contrast, for intermediate $U \sim 5.5t$, the metallic region becomes bounded by a G-type insulator at lower t' values and an A-type insulator at large $t'/t \sim 0.9$. With a further increase in U , the metallic regime reduces and closed for $U = 6t$. The phase diagram is reminiscent of at $T = 0$ quantum critical point with the metallic regime fanning out with increasing temperature. The observed phenomenology of unbounded to bounded metallic regime results from the non-monotonic dependence of critical U for the insulator to metal transition on t' .

iii) Pseudogapped metal at finite temperature: From the density of states, we find that for $U > 2t$ and $t' < -0.2t$, the metal in proximity to the insulator-metal boundary has a clear pseudogap structure. The pseudogap behavior is most pronounced at low temperatures and weakens with temperature increase, and gives way to a non-pseudo-gapped DOS at high temperatures. Thus, unlike the $t' = 0$ half-filling case where the finite local moments imply an insulator, our work reveals a finite-temperature metallic regime with local moments. From the power law of temperature dependence of resistivity ($\sim T^\alpha$), we demonstrate a clear deviation from the exponent value of $\alpha = 2$ (as expected from Fermi liquid prediction) in the pseudogapped phase. We demonstrate that the pseudogapped behavior and the deviation from the the Fermi liquid behavior originates from scattering of electrons from spatially inhomogeneous local moment distribution at finite temperatures. Our finite temperature semi-classical study suggests a phenomenology whereby with increasing U , a small U Fermi liquid evolves into finite T pseudogapped metal (violating Fermi liquid predictions) and finally into a Mott insulator at half-filling in the presence of frustration.

iv) Broader relevance: Our s-MC results show deviation from the Fermi liquid behavior at finite temperature, although dynamical fluctuations are explicitly absent in the semi-classical approach. Thus, the result should be interpreted as

a signature of a thermal fluctuation-driven deviation from Fermi liquid and not a quantum critical fluctuation-driven phenomenon. Indeed, the notion of quantum fluctuation controlling the non-Fermi liquid-like behavior at very high temperatures has remained controversial [2, 3]. There are recent experiments that indeed report finite T deviation from Fermi liquid behavior in disorder free cases that are not tied to $T = 0$ quantum critical points. Also as discussed in the thesis, many body analysis of the half filled Hubbard model with the longer range hopping indeed causes a non-Fermi liquid behavior at $T = 0$ aided by quantum fluctuations not necessarily tied to a quantum critical point [4]. Our results complement these work by showing that deviations from Fermi liquid can also occur in the temperature fluctuation dominated phase (much lower than the Fermi temperature). Hence, our result points to a possible crossover from a quantum fluctuation driven to thermal fluctuation driven metal that does not respect Fermi liquid behavior in the presence of frustration and interaction, but is not associated with a quantum critical point.

Effect of frustration and staggered potential in the half-filled Hubbard model

A rather unexpected metallic instability arising out of a band and Mott insulating tendencies in the square lattice Hubbard model was reported a few years ago, on introducing staggered onsite potentials (Δ)—the 'ionic' Hubbard model [5, 6]. Very recently [7], it was shown that introducing the next nearest neighbor hopping (t') stabilizes the metallic instability over a broad $U - \Delta$ parameter regime in addition to exhibiting half-metallic behavior at $T = 0$. Given our earlier study of the Hubbard model at half-filling as a natural extension of exploring finite temperature properties of strongly correlated systems, in this project [8], we applied s-MC to understand the fate of the $T = 0$ half metal at finite temperature. By this procedure, we constructed the complete phase diagram of the model for the first time that includes all other previously reported $T = 0$ phases.

i) Low-temperature properties: Our $U-T$ phase diagram at a fixed Δ and t' show a paramagnetic band insulator to a low T half-metal (HM1) and finally to a Mott insulator transition with increasing U . HM1, has a finite charge gap for one spin channel, while the other is gapless. This low T half metal results from an effective spin-dependent staggered potential within a mean-field. HM1 and the Mott state show staggered magnetic order. Remarkably, we also found that the charge gap for the two spin channels is spin asymmetric in the Mott state. Given this, a couple of interesting questions arise. Is it possible to close the charge gap of one spin channel before the other by admitting thermal fluctuations? If yes, will the resulting state be a half-metal as well? We answer these questions in the affirmative in our work.

ii) Finite-temperature transport: We compute the temperature-dependent spin resolved resistivity within the Kubo-Greenwood formalism and extract the transport spin polarization from this. For HM1, the thermal fluctuation induced gradual filling of the $T=0$ charge-gap (for the insulating spin channel) leads to a depolarization of the electronic current. We establish that the critical temperature (T_P) for complete depolarization increases monotonically with U , up to the critical U for Mott transition. Focusing on the thermal evolution of the Mott state, we find that for a window in U , in the vicinity of the metal to Mott transition, the slope of the spin-resolved resistivity for the two spin channels changes the sign from negative (insulator) to positive (metal) at two different temperatures. This behavior stabilizes a novel spin-polarized metal that emerges upon heating a Mott insulator. We show that the spin polarization starts below a temperature scale T_P and results from an imbalance of sub-lattice charge occupations due to the presence of Δ . The differential sub-lattice occupations and correlation effects lead to unequal sub-lattice magnetization (or a ferrimagnetic order) and net spin polarization of the system. We show that the imbalance in the sub-lattice occupations and the total spin polarization, which induces the spin-polarized metal, grow monotonically with reducing

temperature. Concomitantly, we find that the spin polarization of the metal grows with temperature decrease and reaches a maximum possible value of 100% at a temperature scale T_S . At T_S , the large occupation on the sub-lattice with $-\Delta$ potential becomes energetically untenable, and there is a first-order transition at T_S , from the 100% spin-polarized metal to a Mott insulator. We further demonstrate that T_S itself increases with increasing U . We thus have a new finite-temperature half-metal (HM2), where we can tune the window of half metallicity by changing U . Moreover, the spin polarization is 100% in the vicinity of T_S even when T_S is enhanced. We show that the novel phase is stable over wide parameter window and propose candidate materials where it can be realized.

iii) Broader relevance: Spin-polarized current sources or half-metals are vital in spintronic device applications. However, all known candidate half metals have 100% spin polarization close to zero temperature and lose their polarization with temperature increase. This behavior is due to the loss of quantum coherence on the admission of thermal fluctuations. Our work proposes a way to circumvent the expected thermal decoherence and sustaining a finite temperature half-metal with 100% spin polarization.

References

1. Gour Jana and Anamitra Mukherjee 2020 J. Phys.: Condens. Matter **32** 365602
2. N. Nagaosa and J.-i. Takimoto, Journal of the Physical Society of Japan **55**, 2735 (1986)
3. T. Egami, S. Ishihara, and M. Tachiki, Science **261**, 1307 (1993)
4. Emanuel Gull *et. al.* Phys. Rev. B **80**, 245102 (2009)
5. Arti Garg *et. al.* Phys. Rev. Lett. **97** 046403 (2006)
6. Bag *et. al.* Phys. Rev. B **91** 235108 (2015)
7. Bag *et. al.* Phys. Rev. B **103**, 155132 (2021)
8. Gour Jana, Abhishek Joshi, Subhajyoti Pal, and Anamitra Mukherjee, Commu-

Communications Physics **5**, 66 (2022)

List of Figures

1.1	(a) Schematic picture of the square lattice with nearest neighbor (nn) hopping t and next nearest neighbor (nnn) hopping t' . There are two kind of sub-lattice, black circles represent A sub-lattice with $+\Delta$ and red circles are for B sub-lattice with $-\Delta$ as shown. (b) Table of usual candidate of half metals, their Curie temperature, saturation magnetizations at 330K and spin polarization at room temperatures. (c) Magnetization (solid line, different solid symbols are from different measurement techniques) and spin polarization (solid symbols) as a function of temperature for CrO_2 [19].	4
1.2	Schematic picture of 1st Brillouin zone for non-interacting electrons on a square lattice in the tight binding model at half-filling. The shaded regime is the filled Fermi surface.	10

- 1.3 Left panel: Brillouin zone sectors with 8 clusters depicting the definition of the four inequivalent momentum sectors A, B, C, and D. The non-interacting Fermi surface for $t'=-0.15t$ at half-filling is shown by the gray line. Right panel: Sketch of the paramagnetic DCA phase diagram of the Hubbard model, calculated with the cluster definitions shown in the left panel, as a function of interaction strength U vs t' . Red region depicts a Fermi-liquid metal, a sector-selective intermediate phase in green shows non-Fermi liquid behavior and a completely gapped insulating phase on the right in blue. The figure is from reproduced literature, Emanuel Gull, Olivier Parcollet, Philipp Werner, and Andrew J. Millis, Phys. Rev. B **80**, 245102 (2009). . . . 12
- 1.4 This figure is reproduced from the Ref.[18]. In panel (a), the imaginary part of the self-energy is plotted against temperature (both are in log scale) for distinct r values. Panel (b) shows the exponent, n of temperature extracted from the plot in panel (a) against r 13
- 1.5 (a) This Gutzwiller $t' - U$ phase diagram at $T = 0$ is reproduced from the paper, L. Tocchio et al. Phys. Rev. B **78**, 041101(R) (2008). The phases are indicated in the phase diagram and discussed in the text. (b) The VCA $t' - U$ phase diagram at $T = 0$ obtained from the Ref.[44]. The blue regime in between superconducting (SC) and N'eel anti-ferromagnetic phase is the coexisting phase of SC and N'eel ordering and the red-white hatched area indicates the non-magnetic phase. 14

1.6	U-T phase diagram at half-filling found from the CDMFT study in the Ref.[46] is shown here for different frustraion value (t'). The black curve with squares is anti-ferromagnetic transition temperatures for $t' = 0$ case. As the t' destabilizes the insulating phase, the increase in t' values lead to suppression of magnetic transition temperatures as shown by the curves with red circles, blue uptriangles and green downtriangles for $t' = -0.1t$, $-0.3t$ and $-0.5t$ respectively. The amount of suppression increases with increase in t' values. The regions under each of curves are anti-ferromagnetic insulators.	15
1.7	The $\Delta - U$ phase diagram found from DMFT study of IHM in the Ref.[48] at $T = 0$. The line between band insulator and Mott insulator is the metallic instability.	19
1.8	The $t' - U$ phase diagram found from Hartree-Fock (HF) in panel (a) and DMFT in panel (b) in the Ref.[47] at $T = 0$. In the inset of panel (a), differential sublattice magnetization, δs (top inset) and uniform magnetization, s_u (bottom inset) obtained from HF calculation are plotted as a function of U/t for different t' and fixed $\Delta (= 1.0t)$ as indicated.	20
2.1	Imaginary time slice and temporal path for s-MC and DQMC shown by the red dashed arrow and black arrows respectively	27
2.2	Flow chart of the semi-classical Monte-Carlo scheme.	31
2.3	Flow chart of the Metropolis scheme.	32

- 2.4 This shows the average energy vs MC sweep data found from MC annealing for a 16^2 system size square lattice using 4000 MC sweeps for the case of half-filled Hubbard model for different interaction strengths $U = 2.0t$, $4.0t$ and $8.0t$ shown in panel (b), (a) and (c) respectively for $t' = 0$ and $t' \neq 0$ cases. Panel (a) is presented only for $t' = 0$ case at $T = 0.1t$. Where as panel (b) and (c) are shown for $t' = 0$ and $-0.3t$ indicated by the black and red colours for above mentioned correlation values at fixed temperature $T = 0.05t$ 34
- 2.5 Scematic diagram of TCA scheme. 35
- 2.6 Finite temperature $U - T$ magnetic phase diagram. The red solid squares and open squares are the anti-ferromagnetic Neel temperature T_N found from s-MC [89] and DQMC [92] study respectively. The blue dashed line is T_N line got from HF theory. The light blue regime is the preformed local moment regime. 37
- 3.1 Low temperature $U - t'$ phase diagram. The various phases obtained are a paramagnetic metal (PM-M), $\mathbf{q} = (\pi, \pi)$, (G-type) antiferromagnetic insulator AF1-I; $\mathbf{q} = (\pi, 0)/\mathbf{q} = (0, \pi)$, (A-type), antiferromagnetic insulator AF2-I; and a low T correlated paramagnet (C-PM) insulator at large U . For $5.2 < U/t < 6$, there is a re-entrant insulator to metal transition around $t'/t \sim -0.8$. The data was obtained on a 32^2 system. The open circles, crosses and open squares are data reproduced from L. Tocchio *et al.* Phys. Rev. B **78**, 041101 (2008). These are discussed in the text. The phase diagram is calculated at the lowest temperature $T = 0.005t$ 41

- 3.2 This plot shows finite temperature $U/t - T/t$ phase diagram at different t' values. The red with open circles, green with open up-triangles, blue with open down triangles and magenta with open diamonds are the curves of antiferromagnetic N'eel temperature T_N for $t' = 0.0, -0.4t, -0.6t$ and $-1.0t$ respectively, plotted against interaction value U/t which are found from the static magnetic structure factor calculation. The parameters are indicated with same colors in the figure. Out of four curves, red, green and blue ($t' = 0.0, -0.4t, -0.6t$) are for $q = (\pi, \pi)$ and the magenta ($t' = -1.0t$) is for $q = (\pi, 0)$ or $q = (0, \pi)$ magnetic ordering. The various dashed and dashed dotted lines are referring T^* scale which is associated with thermal fluctuation evolved Metal-Insulator transition indicted with respective colors. 43
- 3.3 In the figure, panel (a) shows static magnetic structure factor as function of temperature for $U = 4.0t$ for the frustration values as indicted in the panel with respective colors. Panel (b) represents also static magnetic structure factor plotted against T for $U = 8.0$. Here red, green and blue are for (π, π) magnetic ordering where as the magenta is for $(q = (\pi, 0)/q = (0, \pi))$ magnetic ordering. The parameters are mentioned in the panel with same color schemes. (c) shows the real space spin correlation $C(r)$ as a function of the Manhattan distance, $r = \sum_{i \in \hat{x}, \hat{y}} |r_i|$, between the spins, at $T = 0.005t$. The data is shown for $U/t = 2$ and 22 and $t'/t = -0.7$. (d) show the momentum space map of S_q for $U/t = 22$ at $T = 0.005t$. All results are shown for 32^2 real space system. 45
- 3.4 Enlarged form the low temperature phase diagram given in the fig-1. The three dashed lines are guide to the eye for different U/t values as 4.0 5.6 and 6.0 46

- 3.5 This figure shows the density of states (DOS) for three values of U , $4.0t$, $5.6t$, and $8.0t$ in the panels (a), (b), and (c) respectively. In (a), the DOS for $t' = 0$, $-0.4t$ are insulating and for $-0.8t$ is metallic as depicted by the black, red, and green lines respectively. In panel (b) the red and green are for $t' = -0.3t$ and $-1.0t$ respectively which are gapped but the magenta for $t' = -0.8t$ has a pseudo-gap at the chemical potential, referring to the re-entrant metallic phase. The panel (c) shows that DOS for $t' = 0$, $-0.6t$ and $-1.0t$ with black, red, and green solid lines respectively as indicated in the figure are all gapped and this refers to the MI phase. 47

- 3.6 (a) to (c) show $t' - T$ phase diagrams for $U = 4.0t$, $5.6t$ and $6.0t$. (d)-(f) show $\omega\sigma(\omega)$ vs ω plots for $t' = 0.6t$, $0.9t$ and $1.0t$ at fixed $U = 5.6t$ shown. In (a)-(c), the yellow regime is the (π, π) insulator (AF1-I) phase. In (b) and (c) the orange regions are paramagnetic insulator (PM-I) and the green regions indicate A-type insulator (AF2-I). The dotted regime is a paramagnetic metal (PM-M) in all three cases. $\omega\sigma(\omega)$ in (d) to (f) are plotted for two temperatures each as indicated. The solid lines are linear extrapolations starting from $\omega/t = 0$ in the lower three panels. 49

- 3.7 Panel (a) represents thermal evolution of the density of states (DOS) for $U = 5.6t$ at $t' = -0.8t$. The orange, blue, green and red curves represent DOS for $T = 0.3t, 0.1t, 0.05t$ and $0.04t$ respectively as indicated. (b) shows temperature dependent resistivity in units of $\frac{\pi e^2}{\hbar a}, \rho(T)$ at $t' = -0.8t$ for different U as shown in the plot. The green, magenta, violet and black curves are for $U = 6.0t, 4.0t, 3.0t$ and $1.0t$ respectively. In (c), the exponent, α of resistivity, $\rho(T)$ is plotted against U for $t' = -0.8t$ and $t' = -0.3t$ represented by the open squares and solid hexagons respectively. (d) shows the distribution of local moments $P(M)$ for different temperatures for $U = 5.6t$ and $t' = -0.8t$. The solid red line with diamonds, blue line with circles, orange line with up triangles and brown dashed line are for $T = 0.04t, 0.1t, 0.3t$ and $3.0t$ respectively. 51
- 3.8 Panel (a) shows the single particle DOS found from Lanczos on a 4×6 cluster at $T = 0$ for $t' = -0.8t$ and different U values. Panel (b) shows the local moment (M) as a function of U/t for the system for the same t' value. 53
- 4.1 The spin resolved resistivities are presented in panel (a) for $t' = -0.2t$ and $\Delta = 1.0t$ at fixed interaction $U = 2.6t$ in the panel. The blue line with up-triangles is the resistivity for up spin and red square with solid line depicts the down spin channel of the resistivity. The curves are on top of each other. Panel (b) shows the sublattice resolved density of states (DOS) for the same parameter values at low T. The green line and red lines are DOS for sublattice A and B as shown respectively. 60

4.2 In panel (a) spin resolved resistivity in the Mott phase at $U = 5.5t$ for fixed frustration and ionic potential $t' = -0.2t$ and $\Delta = 1.0t$ respectively. The resistivity for up spin and down spin are given by solid blue line with up triangle and solid line with square respectively. The low T spin resolved DOS is shown in panel (b) for the same U , t' , and Δ with blue line indicating the up spin channel and red one is for down spin channel as indicated by the arrows with same colours. . 61

4.3 In this figure, panel (a) shows the spin resolved resistivities as a function of temperature at $U = 3.2t$ for frustration $t' = -0.2t$ and ionic potential $\Delta = 1.0t$. Here, the blue up triangles with solid line resistivity for the up spin and the red one with solid squares is that for the down spin channel. Slope of the curve for the down spin is negative and hence refers to insulating behavior where as the up channel because of negative slope, gives metallicity . The point where both curves merge, polarization goes to zero (explained in the main text) the temperature scale is named as T_p . The panel (b) shows the low T spin resolved DOS at the same interaction value U and t' and Δ . The red dotted line is for the down spin channel and shows insulating behaviour whereas the blue solid line represents the up spin channel which shows metallic behaviour. 62

- 4.4 The panel (a) shows spin resolved resistivity ($\rho_\sigma(T)$, $\sigma = \uparrow\downarrow$) vs temperature (T) at $U = 4.8t$ for $\Delta = 1.0t$ and $t' = -0.2t$. The red line with solid squares and blue line with solid up-triangle represent T dependent resistivity for down and up spin respectively. The black arrows defining T_s and T_p are corresponds to on set metallic phase and polarization temperature. This is discussed in details in the main text. In the inset the total resistivity is plotted against T at the same parameters value. In panel (b) spin resolved DOS is plotted. The blue and red solid line represent the DOS for up and down spin channel respectively for $\Delta = 1.0t$ and $t' = -0.2t$ at $U = 4.8t$. The arrows with respective colours show the spin channels in panel. 64

- 4.5 The panel (a) shows the spectral weight of up and down spin channels at the chemical potential as a function of temperature. The red solid line with squares and blue solid line with up-triangles are the temperature evolution the zero frequency weight of the down and up spin channels respectively. The black thick arrows specifies the T_s and T_p as in the resistivity calculations. In panel (b), the polarization of conduction electrons, ($P(T)$) vs temperature (T) is plotted for three different interaction values $U = 3.2t$, $4.8t$ and $4.9t$ and corresponding curves are shown by solid blue line with uptriangles, solid red line with circles and solid black line with squares respectively. The arrows are indicating T_s and T_p with respective colours for these U values. 65

- 4.6 In this figure, the panel (a) shows the sub-lattice magnetization as a function of temperature for $U = 3.2t$ and $4.8t$ as indicated at fixed $t'(-0.2t)$ and $\Delta(1.0t)$. The red line with open squares and blue line with open circles are for A and B sub-lattices respectively for $U = 3.2t$. The curves with same colours but with solid symbols show the results for $U = 4.8t$. In panel (b), up and down spin density difference i.e. $\delta n = n_{\uparrow} - n_{\downarrow}$ is plotted as a function of T at $U = 4.8t, 4.9t, 4.95t$ indicated by solid gray line with uptriangles, green line with diamonds and blue line with circles respectively for $t' = -0.2t$ and $\Delta = 1.0t$. In panel (c), the local moment distributions in real space are plotted for different temperatures at $U = 4.8t$ for $\Delta = 1.0t$ and $t' = -0.2t$. The blue, orange, green, brown and black with solid and dashed lines are shown here for temperatures, $T = 0.01t, 0.03t, 0.07t, 0.1t$ and $1t$ respectively. Panel (d) shows the sub-lattice local moment difference, $\delta M = M_A - M_B$ plotted against temperature for the same U values as in panel (b) represented by solid gray line with open uptriangles, green line with open diamonds and blue line with open circles respectively for $t' = -0.2t$ and $\Delta = 1.0t$ 67
- 4.7 The sublattice resolved double occupation is plotted as a function of temperature in panel (a) for $t' = -0.2t$ and $\Delta = 1.0t$ at $U = 4.8t$. The blue and black lines are for A and B sub-lattices respectively. In the panel (b), the differences of local moment for sublattice A and B, obtained from cooling and heating procedure in s-MC method are plotted against temperature for $U = 4.9t$ at the same t' and Δ as in panel (a). The hysteresis in δM hints towards the first order transition at the onset of HM_2 phase. 68

- 4.8 Panel (a) shows the full $U-T$ phase diagram for fixed $t' (= -0.2t)$ and $\Delta (= 1.0t)$. In panel (b) magnified version of the full phase diagram is shown focusing into the HM_2 phase. In both the figures, same colours scheme are used for indicating different phases. The gray and yellow regimes show the HM_1 and $M-I$ phases respectively. The red region is the finite T half-metallic phase, HM_2 . The details are discussed in the text. 69
- 4.9 In this figure, panel (a) shows the tunneblity of HM_2 phase as a function of t'/t for fixed $U = 4.8t$ and $\Delta = 1.0t$. The solid blue line with uptriangles is the thermal scale T_s for onset of HM_2 and solid red line with squares denotes the polarization temperature T_p . In panel (b), the $\Delta-U$ phase diagram is shown at $t' = -0.2t$. The brown region is the $M-I$ phase and the window in between the black dashed line and the solid line is the HM_2 phase emerges up on heating the $M-I$ phase close to the Mott-metal transition. For simplicity the band and HM_1 phases are not shown here. 71

Chapter 1

Introduction

Condensed matter physics goes hand in hand with fascinating material discoveries and technological applications. Correlation physics of electrons in the heart of many non-trivial phenomena enriches the subject on its own and widens the path of realizing promising materials experimentally to meet technological purposes. One of the critical models to incorporate electron correlation is the Hubbard model [1]. The model has been studied for more than 80 years because it captures the physics of interacting electrons relevant to solid-state materials. Although the model approximates the long-range Coulomb interaction by local repulsion, it continues to unveil new physics like high- T_c superconductivity, non-Fermi liquid metal, half-metal, metal-insulator transition, spin liquids, among others.

Understanding the physics of the metallic state has remained a long-standing goal of condensed matter theory. The single-electron picture holds primarily due to screening effects in the usual metals. The standard paradigm for understanding metals is the Fermi liquid theory. The theory holds for interacting electrons when adiabatic continuity to the non-interacting limit survives. The excitations of such a theory are called quasiparticles, long-lived excitations at the Fermi surface.

With the advent of sophisticated experimental methods such as Angle-Resolved Photo Emission Spectroscopy (ARPES), quantum oscillation measurement techniques to map out Fermi surfaces coupled with transport measurements on near-

ideal (single crystal) samples have uncovered many materials that strongly violate of Fermi liquid theory including high- T_c cuprates[2][3], heavy fermion systems[4][5], oxide heterostructures[6] and in the parent compound of recently discovered iron based superconductors[7], to name a few. Experimental study for example, Neutron-Scattering result and NMR study of cuprate candidate, $La_{2-x}Sr_xCuO_4$ show that mass of the quasiparticle gains slightly higher mass with out strong magnetic interaction or polarizability and it shows marginal-Fermi liquid behavior for which the scattering rate goes linearly with thermal scale and frequency [Phys. Rev. B **48**, 487 (1993)]. Other candidate for cuprate, $Yb_{a_2}Cu_3O_{6+x}$ studied by Neutron-Scattering and NMR show d-wave pairing indicated by spin excitation as found theoretically in the small interaction limit for the two dimensional Hubbard model in the presence of next nearest neighbour hopping (t'). t' is naturally generated in the system, confirmed by spectral function found from Angle-Resolve Photoemission Spectroscopy (ARPES) as the next nearest neighbour hopping is needed to fit the data [Phys. Rev. B **49**, 4235 (1994)]. At present, a microscopic description of the transport and nature of excitations in such non-Fermi liquids remains elusive. Strong quantum fluctuations are the primary agency leading to non-Fermi liquid behavior. The origin of such quantum fluctuations is quantum critical points at zero temperature. We expect these fluctuations to not only destroy Fermi liquid-like behavior at zero temperatures but modify the finite temperature response of the metal. However, it is unclear how the low-temperature quantum fluctuations can modify the finite temperature behavior in the temperature-dominant regime. Recent experiments[8][9] show that, remarkably, non-Fermi liquids can indeed occur in situations where there are no zero temperature quantum critical points. These results go against traditional folklore and echo the views in theoretical literature as well[10][11]. In recent years, the study of single band Hubbard model using DQMC [12] [13] [14] and DCA [15][16] give various insights about the stripe order and superconduction pairing instability. Currently, development of the cold atomic system helps to realize Hubbard like model by Fermi gas in optical lattice and the energy scales are reliable to study at different temperature regime up to thermal scale $0.2t$

[Science **340** 6138 (2013)], in nearest neighbour hopping scale t (experimental scale $t/h \sim 174Hz$) [Phys. Rev. Lett. **115** 115303 (2015)] with tunable parameters. The set up can be employed to study quantum magnetism in different underlying lattice geometry and dimensionality like anisotropic cubic lattice, honeycomb lattice by local entropy redistribution scheme [Science **340** 1307 (2013)]. The interaction strength (U) can be tuned within the window $[0, 30t]$ [Phys. Rev. Lett. **115** 115303 (2015)]. The cold atomic set up also can give insight into many body physics such as anti-ferromagnetic correlation [Nature **519** 211 (2015)] and high- T_c superconductivity [Phys. Rev. Lett. **89** 220407 (2002)]. As the first project in this thesis, we use a semi-classical approach to study the Hubbard model that by design reduces to Hartree-Fock theory at zero temperature but gets progressively accurate with temperature increase. The technical details of the method are presented in chapter 2. Thus, there are no quantum-critical fluctuations in our work at zero temperature. We investigate the possibility of deviations from Fermi liquid theory purely driven by thermal fluctuations within this setup upon introducing longer range hopping. As discussed later in the chapter our study is motivated by zero temperature work within ‘dynamical cluster approximation’ [17] and self-consistent Random Phase Approximation (RPA) [18], which show that weak lifting of nesting instability in correlated systems and induce non-Fermi liquid behavior. We discuss our results of this project in chapter 3.

As a natural extension of the previous project, we add staggered onsite potential to the half-filled Hubbard model with next-nearest-neighbor hopping. The generalized model is called the ionic Hubbard model (IHM) and was first introduced to study charge transfer physics in organic salts [20] and for modeling ferroelectric perovskites [21]. This innocuous-looking additional term has since led to many questions, especially on the theoretical front. In the non-interacting limit, the model is a band insulator, while in the large interaction limit, we expect the usual Mott insulator at zero temperature, as discussed earlier. However, the interest in this model is as follows. As discussed below in detail, comparable correlation strength and charge transfer energy can stabilize a metallic state at zero temperature within a paramag-

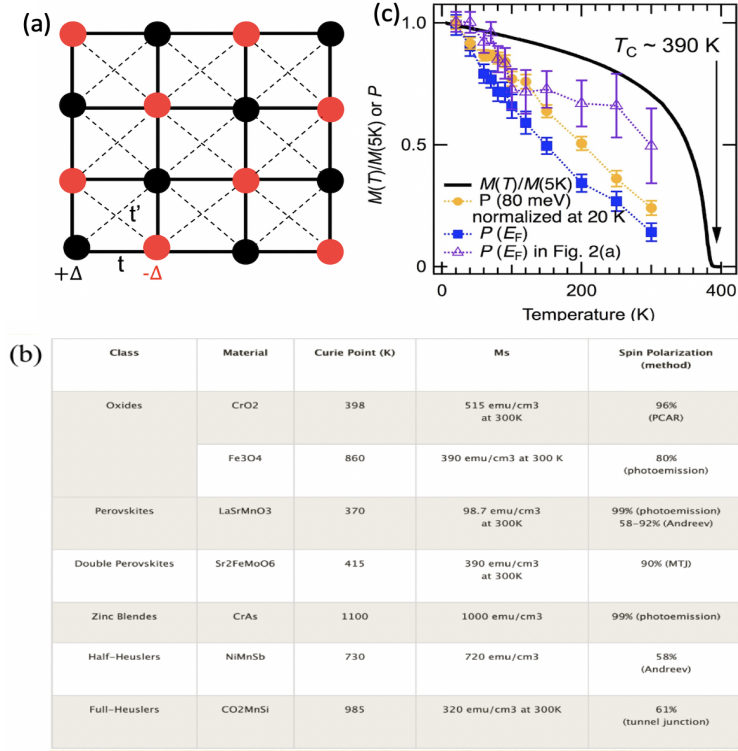


Figure 1.1: (a) Schematic picture of the square lattice with nearest neighbor (nn) hopping t and next nearest neighbor (nnn) hopping t' . There are two kind of sub-lattice, black circles represent A sub-lattice with $+\Delta$ and red circles are for B sub-lattice with $-\Delta$ as shown. (b) Table of usual candidate of half metals, their Curie temperature, saturation magnetizations at 330K and spin polarization at room temperatures. (c) Magnetization (solid line, different solid symbols are from different measurement techniques) and spin polarization (solid symbols) as a function of temperature for CrO₂ [19].

netic background. However, this so-called "correlated band insulator" to metal to Mott transition had remained controversial. We will discuss below that allowing for antiferromagnetic order suppresses the metallic state. More recently, the addition of next nearest neighbor (nnn) hopping in the IHM has revealed that the metal can indeed be stabilized in various magnetic backgrounds within dynamical-mean-field theory at zero temperature. We show the schematic of the lattice structure in Fig.1.1 (a). Among the various metallic states, an antiferromagnetic half metal appears. Given the semi-classical method we have already used in the previous project, it was a natural next step to study the fate of half metals at finite temperature. With this motivation, we briefly discuss the importance of half metals and why it is pertinent

to study their properties, in particular spin polarization with temperature.

Half metals are spin-polarized conductors that are of great importance for spintronics or spin-based electronics. This is because spin-based electronics rely on spin current sources. Thus half metals are vital. In a solid-state systems, finding the source of half-metal is one of the most active areas of recent theoretical research within model Hamiltonians [22] [23] [24] [25] [26] [27] [28] [29][30] and experiments[31][32][33]. In this regard materials like manganites[34] [35], double perovskites[23] [24] [25], Heusler alloys[26] [27] [28] [31][32][33] have been studied rigorously. Also creating different chemical environment in the solids, like incorporating vacancies in transition metal oxides for example in NiO , MnO [36], fluorinated BN , ZNO [37] and ferri-magnetic inverse spinels as in Fe_3S_4 [38] are believed to exhibit half-metallicity.

The above studies have shown that half metallicity is a purely quantum mechanical phenomenon where the spin polarization is 100% at $T=0$. The polarization degrades with temperature due to spin direction dephasing, non-quasiparticle states[39] near Fermi energy, and scattering from phonons. The table in Fig.1.1 (b) shows the current state of usual half metals and their spin polarization at room temperature. Also, in (c), we show a plot of magnetization and spin polarization with temperature for chromium dioxide, showing that the polarization degrades rapidly with temperature. Clearly, for the practical purpose of devise manufacturing, it is essential to realize the half-metal with large spin polarization over a wide-temperature regime. In chapter-4 we discuss our results on the thermal evolution of the zero temperature half-metal reported earlier and predict a novel half-metal that emerges from heating a Mott insulator and whose temperature domain of half metallicity can be tuned. We will also present possible material candidates for realizing the novel half-metal. With this introduction of the broad questions addressed in the thesis and their importance, we now discuss the necessary technical background materials needed for the results presented in subsequent chapters.

1.1 Basics of Fermi liquid theory

Landau Fermi liquid is the standard paradigm for understanding a large class of correlated materials. For non-interacting electrons, the absence of scattering implies that an added particle above the Fermi surface or a hole below the Fermi surface cannot decay. Landau's deep insight was to show that these long-lived excitations are adiabatically connected to the case of interacting electrons. In such cases, the electrons are dressed by interaction effects, and the single-particle excitations at the Fermi energy are called quasi-particle excitations. These excitations are unique because they are long-lived on experimental time scales. We briefly discuss the critical conditions for the validity of Fermi liquid theory and summarize some of its well-known properties below.

1.1.1 Adiabaticity

The adiabaticity is important in the Fermi liquid theory, through which we can establish a one-to-one correspondence between the non-interacting states and interacting states without losing the symmetries of the problem. Suppose, H_0 is the non-interacting Hamiltonian with ground state $|\phi_0\rangle$. Now, if we add a small perturbation in the system by switching on small interaction and evolve slowly H_0 to H_1 , the total Hamiltonian will be

$$H(t) = H_0 + H_1(t) \tag{1.1}$$

Now, the new ground state of H is $|\tilde{\phi}_0\rangle$. So, in the process of slowly turning on the interaction $|\phi_0\rangle$ evolves to $|\tilde{\phi}_0\rangle$. Suppose no level crossing happens in the adiabatic switching on of the interaction. In that case, the symmetries of $|\tilde{\phi}_0\rangle$ will be the same as $|\phi_0\rangle$ and also the charge, spin, and momentum remain the same, but dynamical characteristics like mass, magnetic moment will get renormalized in the new interacting situation. In addition, if level crossing happens in the adiabatic

switching on the interaction, symmetries of the ground states will not be preserved and show phase transition. So, some critical value of interaction strength may exist below which Fermi liquid will be stable.

1.1.2 Quasi-particle excitation and its lifetime

The notion of quasi-particle lets us carry through the physics of single-particle theory even in the interacting environment, provided the notion mentioned above of adiabatic connection remains valid. As mentioned before, the quasi-particle carry the same conserved quantum numbers like charge, spin, momentum of the bare electron but the dynamical properties like mass (m) and magnetic moment (g) get renormalized to m^* and g^* respectively. The quasi-particle lifetime can be determined from the imaginary part of the self-energy, which accounts for all the intermediate scattering of a propagating electron. The expression of self-energy is

$$\Sigma(k, \omega - i\delta) = \Sigma'(k, \omega) - i\Gamma(k, \omega)$$

The imaginary part of the self-energy, $\Gamma(k, \omega)$ ($\Gamma > 0$) represents the quasi-particle decay rate, and the inverse of that gives it its lifetime. The lifetime (τ) of quasi-particle is found from $\frac{1}{\tau} = Z_k \Gamma(k, \epsilon_k^*)$ [40] and it goes like ϵ_k^2 . This depends on the renormalized energy ϵ_k^* of the bare electron energy ϵ_k coming from the real part of the self-energy ($\epsilon_k^* = \epsilon_k + \Sigma'(k, \epsilon_k^*)$) at $T = 0$. In these expressions the energy is measured from the Fermi surface. Here Z_k is called quasi-particle weight, defined as the overlap between the quasi-particle state and the bare electron state. It is given by

$$Z_k = |\langle k\sigma | c_{k\sigma}^\dagger | \phi \rangle|^2$$

The renormalized mass, as mentioned before, also can be calculated using the quasi-particle weight as $m^* = m/Z_k$. From here we see that for Fermi liquid to be valid Z should be non zero, as it controls the overlap between the non interacting and the interacting ground states. We also see the effective or renormalized mass of the quasi-particle diverges as $Z \rightarrow 0$. We would like to mention that in the case of k -dependent self-energy, there is anisotropic mass renormalization [e.g. Phys Rev B

96, 125154 (2017)], unlike the isotropic case for k -independent self-energy.

The essential characteristics of the Fermi liquid are T^2 behavior of the temperature dependence of resistivity at low temperatures, i.e., $\rho(T) = \rho_0 + AT^2$; (A is called Kadowaki-Wood ratio.). Here, ρ_0 , residual resistivity comes from the impurity scattering of electrons. The quadratic behavior arises from the quadratic nature of the scattering rate $\Gamma \propto T^2$. Similarly from the expression of free energy for quasiparticles, it can be shown that the specific heat has a linear dependence on temperature. As opposed to non-interacting case, new collective excitations can be seen in the Fermi liquid, namely sound and zero sound. Zero sound was first observed in liquid ^3He [41].

1.2 Hubbard model

The Hubbard model on a square lattice is defined below:

$$H = -t \sum_{\langle ij \rangle, \sigma} c_{i\sigma}^+ c_{j\sigma} + U \sum_i n_{i\uparrow} n_{i\downarrow} - \sum_i \mu (n_{i\uparrow} + n_{i\downarrow}) \quad (1.2)$$

Here, we look at the Hartree-Fock (HF) mean-field band dispersion[42] in the momentum space. This will be useful for the small U analysis and for momentum space analysis of the Ionic Hubbard model. Since it is known that the half filled Hubbard model has a $q = (\pi, \pi)$ or G-type magnetic order, we allow for this antiferromagnetic order in the mean field analysis. For this, as usual, we consider

$$n_{i\uparrow} = \frac{1}{2}n + (-1)^{x_i+y_i}m \quad (1.3)$$

$$n_{i\downarrow} = \frac{1}{2}n - (-1)^{x_i+y_i}m \quad (1.4)$$

where, $n = \langle n_{i\uparrow} + n_{i\downarrow} \rangle$ and $m = \frac{1}{2} \langle n_{i\uparrow} - n_{i\downarrow} \rangle$.

The mean-field band dispersion of the Hubbard Hamiltonian (detailed calculation

is provided in Appendix A) will be

$$E_k^\pm = \frac{1}{2}Un - \mu \pm \sqrt{[4t^2(\cos k_x + \cos k_y)^2 + U^2m^2]} \quad (1.5)$$

'+' and '-' refer to the conduction and valance bands respectively and $m \neq 0$ implies G-type magnetic order.

1.2.1 Limiting cases of Hubbard model

We now consider two important limits of small interaction and very large interaction strengths and discuss why the Hubbard model is insulating for any finite U at half filling on the square lattice. These will be contrasted with our semi-classical results in chapter 3.

a. Weak coupling limit:

To understand the origin of the small U insulator and the concomitant G-type magnetic order, we rewrite the local interaction term in a slightly different form using the fact that $n_{i\uparrow}n_{i\downarrow} = n_i^2/4 - \mathbf{S}_i^2$ and use the mean field decomposition rule $\hat{A}\hat{B} \rightarrow \hat{A}\langle B \rangle + \langle A \rangle\hat{B} - \langle A \rangle\langle B \rangle$.

$$H^{HF} = -t \sum_{\langle ij \rangle, \sigma} c_{i\sigma}^+ c_{j\sigma} + \sum_i \left[\left(\frac{U}{2} \langle n_i \rangle - \mu \right) n_i - 2U \mathbf{S}_i \langle \mathbf{S}_i \rangle \right] \quad (1.6)$$

where the spin operator defined as $\mathbf{S}_i = \frac{\hbar}{2} \sum_{\alpha, \beta} c_{i, \alpha}^\dagger \boldsymbol{\sigma}_{\alpha, \beta} c_{i, \beta}$ and $\{\sigma^x, \sigma^y, \sigma^z\}$ are the Pauli matrices. At half filling, $\langle n_i \rangle = 1$ and then the chemical potential is $\mu = U/2$. By Fourier transforming of $c_{i\sigma}^+$ and $c_{j\sigma}$, we get the Hamiltonian in Fourier space as

$$H_{eff} = \sum_{q, \sigma} \epsilon_q n_{q\sigma} - 2UN \sum_q \mathbf{S}(\mathbf{q}) \langle \mathbf{S}(-\mathbf{q}) \rangle \quad (1.7)$$

Here, N indicates the number of sites, $\epsilon_q = -2t(\cos q_x + \cos q_y)$ is the 2D non-interacting dispersion and spin operator in momentum space is

$$S^\eta(q) = \frac{\hbar}{2N} \sum_{k+q} c_{k, \alpha}^\dagger \sigma_{\alpha, \beta}^\eta c_{k, \beta}$$

with $\sigma_{\alpha, \beta}^\eta$ being the Pauli spin matrices.

For small interaction at half-filling, the expectation value of $\mathbf{S}(q)$ in the ground state

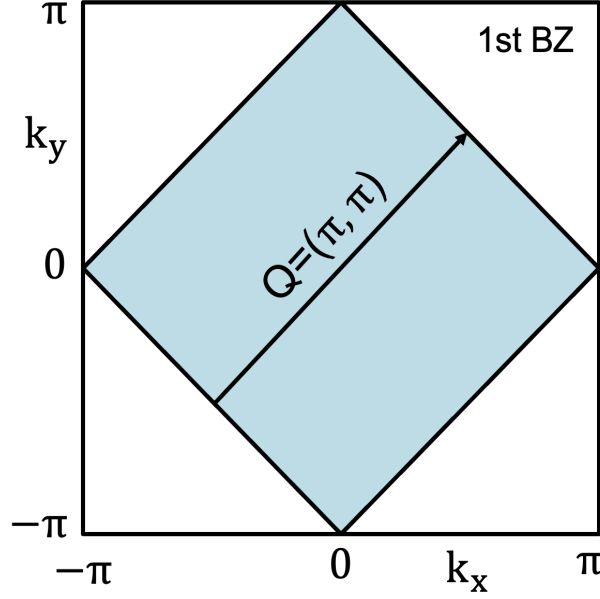


Figure 1.2: Schematic picture of 1st Brillouin zone for non-interacting electrons on a square lattice in the tight binding model at half-filling. The shaded regime is the filled Fermi surface.

is non-zero for the nesting vector $Q = (\pi, \pi)$ indicated by the arrow in Fig.1.2. This Q vector connects the opposite sides of the Fermi surface and the dispersion relation remains invariant through the relation $\epsilon_k = -\epsilon_{k+Q}$. This causes instability coming from the nesting of the Fermi surface and can be seen in the spin susceptibility calculation. We get rotational invariant ground state for the order parameter $\mathbf{S}(Q)$ and we assume that the ground state will be along the z -direction. Thus

$$\langle \Omega | S_Q^z | \Omega \rangle = S$$

Where, S denotes the staggered moment acting as a variational parameter and $|\Omega\rangle$ refers to the true ground state. Then we can write the effective Hamiltonian as follows.

$$H_{eff} = \sum_{k,\sigma} \epsilon_k n_{k\sigma} - US \sum_k (c_{k+Q\uparrow}^\dagger c_{k\uparrow} - c_{k+Q\downarrow}^\dagger c_{k\downarrow}) \quad (1.8)$$

Here, the sum over k vector which runs over the first Brillouin zone can be written as the sum over $k_<$ (inside the shade regime) and $k_>$ (outside of the shade regime) as in schematic picture in Fig.1.2. Hence, $K_> = k_< + Q$. From here onwards we use

$k_{<}$ as k for simplicity. Thus, we can rewrite H_{eff} as

$$H_{eff} = \sum_{k,\sigma} \epsilon_k (n_{k\sigma} - n_{k+Q\sigma}) - US \sum_k' (c_{k+Q\uparrow}^\dagger c_{k\uparrow} + c_{k\uparrow}^\dagger c_{k+Q\uparrow} - c_{k+Q\downarrow}^\dagger c_{k\downarrow} - c_{k\downarrow}^\dagger c_{k+Q\downarrow}) \quad (1.9)$$

The restricted sum in the second term means the summation over k vectors only inside the shaded region. In the first term we have used $\epsilon_k = -\epsilon_{k+Q}$. The detailed derivation (in Appendix B) shows that the nesting driven Spin Density Wave (SDW) gap in the weak coupling limit becomes

$$\Delta \sim t e^{-2\pi\sqrt{t/U}}$$

This sets the scale of anti-ferromagnetic transition temperature T_N in the small U limit.

b. **Strong coupling limit:** Here, we will look into the strong coupling limit of the Hubbard model and show how in this limit Hubbard model reduces to Heisenberg model. We demonstrate the derivation of the Heisenberg model in Appendix C.

$$H_{eff} = \frac{4t^2}{U} (\mathbf{S}_1 \cdot \mathbf{S}_2) \quad (1.10)$$

This is the Heisenberg Hamiltonian with anti-ferromagnetic coupling constant $J = \frac{4t^2}{U}$ derived from the Hubbard Hamiltonian in the large U limit at half-filling.

1.3 Role of longer range hopping

There are various studies of the Hubbard model and its variant in the context of metal-insulator transitions, pseudo-gapped phase, non-Fermi liquid, colossal magnetoresistance, high- T_c superconductivity, half-metal to name a few. Here, we discuss the most relevant works at zero as well as finite T to connect our investigations to previous studies for both the cases Hubbard model at half-filling on square lattice in the presence of frustration ($t - t'$ Hubbard model) and Ionic Hubbard model (IHM) on square lattice at half-filling.

a. **Non-Fermi liquid metal from imperfect nesting:**

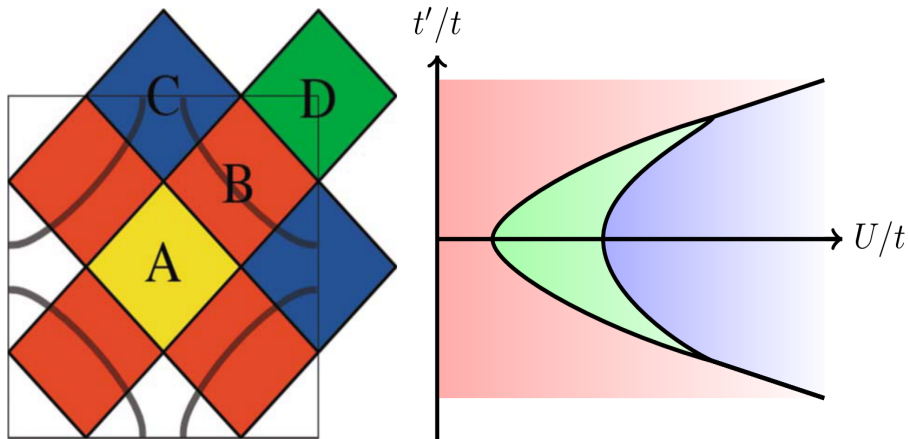


Figure 1.3: Left panel: Brillouin zone sectors with 8 clusters depicting the definition of the four inequivalent momentum sectors A, B, C, and D. The non-interacting Fermi surface for $t' = -0.15t$ at half-filling is shown by the gray line. Right panel: Sketch of the paramagnetic DCA phase diagram of the Hubbard model, calculated with the cluster definitions shown in the left panel, as a function of interaction strength U vs t' . Red region depicts a Fermi-liquid metal, a sector-selective intermediate phase in green shows non-Fermi liquid behavior and a completely gapped insulating phase on the right in blue. The figure is from reproduced literature, Emanuel Gull, Olivier Parcollet, Philipp Werner, and Andrew J. Millis, *Phys. Rev. B* **80**, 245102 (2009).

Investigation of the model done by Millis et al [17] hosted by Dynamical Cluster Approximation (DCA) on an eight site cluster reveals the intriguing physics of the metal-insulator transition at $T = 0$. There is a two stage transition from the metal (Fermi liquid) to Mott insulator through the selection of K-sectors of the Brillouin zone as a function of U . The figure in Fig.1.3 obtained from the study in Ref. [17] shows that at smaller U and at fixed t' in the range $0 \leq t' \leq -0.3t$, the inequivalent momentum sectors B and C have spectral weight at the Fermi energy and the system is Fermi liquid metal. As the interaction grows a spectral gap opens up in one sector C but the sector B remains gapless. With further increase in U , B sector also starts to show gapped behavior. In the regime of interaction where B is gapless and C has gapped Fermi surface which leads to pseudo-gapped DOS and the system shows non-Fermi liquid self-energy behavior and violates Luttinger's theorem. This is clearly an example of a non-Fermi liquid without quantum criticality. Another analysis for the same model at half filling within self-consistent Random Phase Approximation

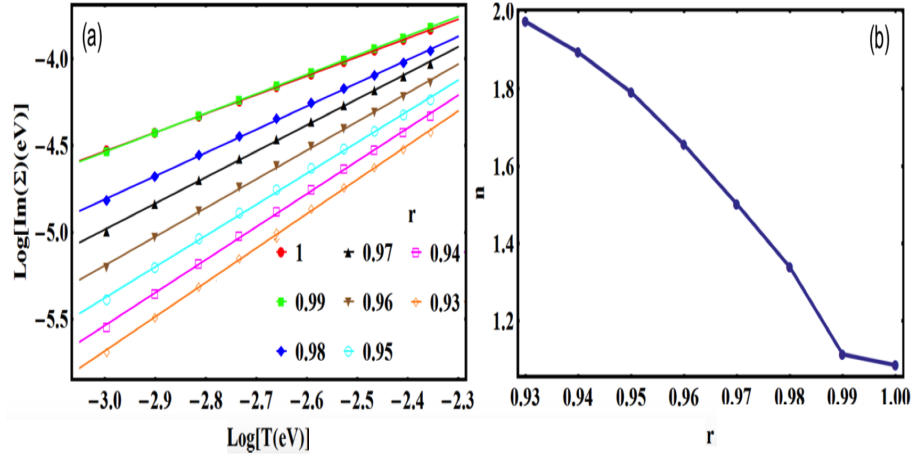


Figure 1.4: This figure is reproduced from the Ref.[18]. In panel (a), the imaginary part of the self-energy is plotted against temperature (both are in log scale) for distinct r values. Panel (b) shows the exponent, n of temperature extracted from the plot in panel (a) against r .

(RPA)[18] also demonstrates deviation from Fermi liquid behavior arising out of partial nesting in presence of interaction. In this calculation the deviation of the nesting was parameterized by a parameter r , by defining the bare dispersion as $\epsilon(\mathbf{k}) = t(\cos(k_x) + \cos(k_y)) + (t' - r)(\cos(k_x)\cos(k_y)) - (\mu - 2r)$. The values of $t = 1.0$, $t' = 1.0$ and $\mu = 2.0$ were chosen in the study, while $r = 1$ (implies perfect nesting). The imaginary part of the self energy vs temperature in the log-log plot is shown in Fig.1.4 (a) for different values of r . The slope provides the exponent of T^n , with imaginary part of the self energy scaling with temperature as T^n . The data is shown for the imaginary part of the self energy evaluated at $\mathbf{k} = (\pi/2, \pi/2)$ and close to the Fermi level $\omega/t = 2$. Panel (b) shows the evolution of the exponent as a function of r . We see a clear deviation of the exponent from the Fermi liquid value of 2 as r approaches 1.

b. Emergent magnetism:

(i) *Magnetism at $T = 0$:* A study of the $t - t'$ Hubbard model by Lin and Hirsch[42] showed that a critical U exist to occur metal to insulator (antiferromagnet) transition in the presence of frustration at half-filling. Another zero temperature study of this model at half-filling using Gutzwiller projected wavefunction method, a variational based calculation showed that there is metal-insulator

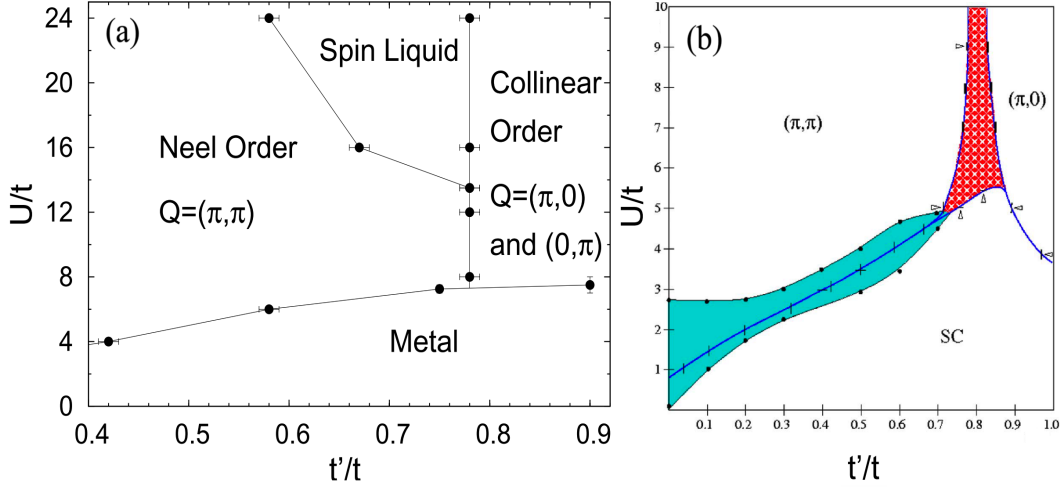


Figure 1.5: (a) This Gutzwiller $t' - U$ phase diagram at $T = 0$ is reproduced from the paper, L. Tocchio et al. Phys. Rev. B **78**, 041101(R) (2008). The phases are indicated in the phase diagram and discussed in the text. (b) The VCA $t' - U$ phase diagram at $T = 0$ obtained from the Ref.[44]. The blue regime in between superconducting (SC) and Neel anti-ferromagnetic phase is the coexisting phase of SC and Neel ordering and the red-white hatched area indicates the non-magnetic phase.

transition due to interplay of Hubbard interaction and frustration comes due to the second nearest neighbor hopping (t')[43]. In chapter 3 we will show that our semiclassical calculation reproduces the phase boundaries shown in the $U - t'$ phase diagram in Fig. 1.5 (a), except the spin liquid phase. There are two kind of anti-ferromagnetic phases, $q = (\pi, \pi)$ (Neel order) in the small t' regime and $q = (\pi, 0)/(0, \pi)$ (co-linear order) for the larger t' values and both the magnetic phase appears beyond a finite critical U (U_{crit}) that depends on t' . In the larger U values and for moderate t' , a spin liquid phase is reported as indicated in the Fig.1.5. The metallic phase is bracketed by the U_{crit} and $U = 0$ for entire t' window $[0, 0.9]$. However the nature of the metal was not reported in the study.

In contrary, Variation Cluster Approximation (VCA) study on an eight site cluster by Tremblay et al[44] of the same model shows that the co-linear order for the larger t' is separated from the Neel order by the non-magnetic phase. Allowing for superconducting solution in the calculation, they found d-wave superconductivity (SC) below the critical values U of magnetic transitions and also a regime

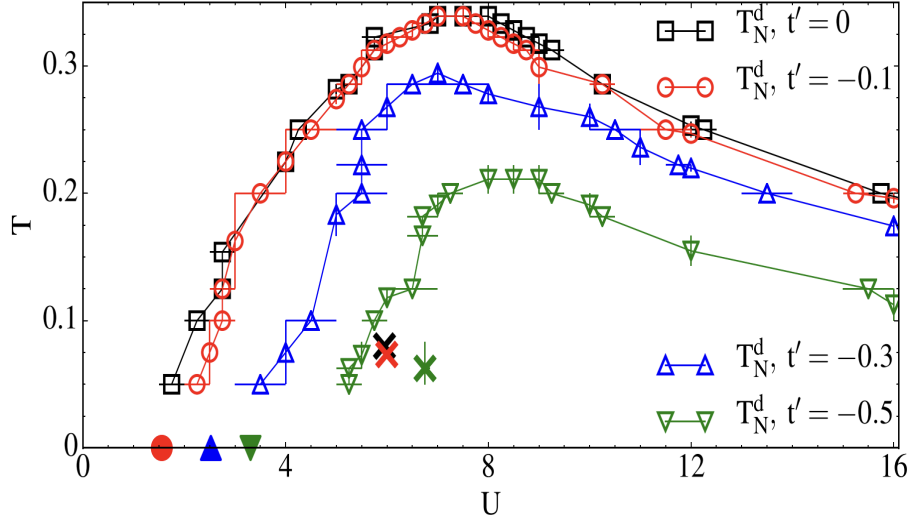


Figure 1.6: U-T phase diagram at half-filling found from the CDMFT study in the Ref.[46] is shown here for different frustration value (t'). The black curve with squares is anti-ferromagnetic transition temperatures for $t' = 0$ case. As the t' destabilizes the insulating phase, the increase in t' values lead to suppression of magnetic transition temperatures as shown by the curves with red circles, blue uptriangles and green downtriangles for $t' = -0.1t$, $-0.3t$ and $-0.5t$ respectively. The amount of suppression increases with increase in t' values. The regions under each of curves are anti-ferromagnetic insulators.

of coexisting phases of SC and Néel magnetic ordering. While we do not consider superconductivity in the present thesis, for completeness we have reproduced the phase diagram from Ref.[44] in Fig.1.5 (b). The model studied by Yokoyama et al. using Path Integral Renormalization Group approach[45] also reported the same phases as in Ref.[44], but the phase boundaries are different.

(ii) *Magnetism at finite temperature:* Due to the fermion sign problem in presence of particle-hole symmetry breaking nnn hopping there are only sporadic study of the model at finite temperature. Here we summarize the most relevant recent work. The cellular dynamical mean-field theory (CDMFT) study of the model by Fratino *et. al.* [46] shows that the magnetic transition temperatures (T_N) are non-monotonic with interaction U for $t' = 0$ up to $-0.5t$ and there is a overall suppression of T_N with t' increase as shown in Fig.1.6. The degree of reduction of T_N , depends on the value of frustration. In this CDMFT study, continuous time quantum Monte Carlo (CTQMC) is used as the impurity solver. As CTQMC suffers from fermion

sign problem, the calculation is limited up to temperature around $T/t = 0.05$ and frustration value $t' = -0.5t$. In chapter 3 we will contrast our semi-classical $U - T$ phase diagram with the data in Fig.1.6.

With this background on the status of the literature prior to our work, we now move on the to ionic Hubbard model.

1.4 Staggered potential in the $t - t'$ Hubbard model

The Ionic Hubbard model has the form given below. While we provide the analysis with the nnn hopping included, historically the model was first studied for only nearest neighbor hopping case as will be discussed below. We will also present the reason why adding nnn hopping became necessary. We begin with the mean field analysis of the model as was done in a very recent work [47]. The work also compared the mean field results with cluster dynamical mean field theory at $T=0$.

$$\begin{aligned}
H = & -t \sum_{\langle i,j \rangle, \sigma} (c_{i\sigma}^\dagger c_{j\sigma} + h.c) - t' \sum_{\langle\langle i,j \rangle\rangle, \sigma} (c_{i\sigma}^\dagger c_{j\sigma} + h.c) \\
& + \Delta \sum_{i \in A} n_i - \Delta \sum_{i \in B} n_i + U \sum_i n_{i\uparrow} n_{i\downarrow} - \mu \sum_i n_i
\end{aligned} \tag{1.11}$$

The notations carry usual meaning defined before. Here the two body Hubbard interaction term can be written in the mean-field language as given below.

$$U n_{i\uparrow} n_{i\downarrow} \simeq U (\langle n_{i\uparrow} \rangle n_{i\downarrow} + n_{i\uparrow} \langle n_{i\downarrow} \rangle - \langle n_{i\uparrow} \rangle \langle n_{i\downarrow} \rangle) \tag{1.12}$$

Here i is the site index and $n_{\alpha\sigma} = c_{\alpha\sigma}^\dagger c_{\alpha\sigma}$ is the number operator with spin σ and $\alpha \in \{A, B\}$ sub-lattices. We will Fourier transform of the IHM using $c_{i\alpha\sigma} \equiv \sum_k c_{\alpha k\sigma} e^{-i\mathbf{k}\cdot\mathbf{r}_{i\alpha}}$.

Then the mean-field Hamiltonian in k -space will have the following form.

$$H^{HF} = -t \sum_{k, \sigma} [\epsilon_k (c_{Ak\sigma}^\dagger c_{Bk\sigma} + h.c) + a_{k\sigma} c_{Ak\sigma}^\dagger c_{Ak\sigma} + b_{k\sigma} c_{Bk\sigma}^\dagger c_{Bk\sigma}] \tag{1.13}$$

Where, $a_{k\sigma} \equiv \Delta - \mu + e_k + U n_{A\sigma}$ and $b_{k\sigma} \equiv -\Delta - \mu + e_k + U n_{B\sigma}$ with $e_k = -4t' \cos k_x \cos k_y$ and $\epsilon_k = -2t(\cos k_x + \cos k_y)$

If the one particle eigenstates of the Hamiltonian are $|f_{k\sigma}^\pm\rangle = (g_{Ak\sigma}^\pm c_{Ak\sigma}^\dagger + g_{Bk\sigma}^\pm c_{Bk\sigma}^\dagger)|0\rangle$

with associated eigenvalues $E_{k\sigma}^\pm$, then we can write eigenvalue equation as

$$\begin{bmatrix} a_{k\sigma} & \epsilon_k \\ \epsilon_k & b_{k\sigma} \end{bmatrix} \begin{bmatrix} g_{Ak\sigma}^\pm \\ g_{Bk\sigma}^\pm \end{bmatrix} = E_{k\sigma}^\pm \begin{bmatrix} g_{Ak\sigma}^\pm \\ g_{Bk\sigma}^\pm \end{bmatrix}.$$

Therefore, the HF band energies $E_{k\sigma}^\pm$ will be

$$\begin{aligned} E_{k\sigma}^\pm &= \frac{1}{2}(a_{k\sigma} + b_{k\sigma} \pm \sqrt{(a_{k\sigma} - b_{k\sigma})^2 + 4\epsilon_k^2}) \\ g_{Ak\sigma}^\pm &= h_{k\sigma}^{\pm 2}/(1 + h_{k\sigma}^{\pm 2}) \\ g_{Bk\sigma}^\pm &= 1/(1 + h_{k\sigma}^{\pm 2}) \end{aligned} \quad (1.14)$$

Here, $h_{k\sigma}^{\pm 2} = -\epsilon_k/(a_{k\sigma} - E_{k\sigma}^\pm)$. Now, we will define the order parameters δs , s_u , and δn representing differential sub-lattice magnetization, uniform magnetization and differential sub-lattice occupation respectively and then write the band energies in terms of the order parameters. The definition of the order parameters are given below.

$$\begin{aligned} \delta s &= (s_{zA} - s_{zB}) \\ s_u &= (s_{zA} + s_{zB}) \\ \delta n &= (n_B - n_A)/2 \end{aligned} \quad (1.15)$$

Where, $s_{z\alpha} = \frac{1}{2}(n_{\alpha\uparrow} - n_{\alpha\downarrow})$ and $n_\alpha = (n_{\alpha\uparrow} + n_{\alpha\downarrow})$ with $\alpha \in \{A, B\}$ in the sub-lattices.

$$\begin{aligned} E_{k\sigma}^\pm &= -4t' \cos k_x \cos k_y + \frac{U}{2} - \frac{\sigma U s_u}{2} - \mu \\ &\pm \sqrt{[\Delta - U(\frac{\delta n + \sigma \delta s}{2})]^2 + \epsilon_k^2} \end{aligned} \quad (1.16)$$

So, this is the band dispersion HF mean-field Hamiltonian. The signs, '+' and '-'

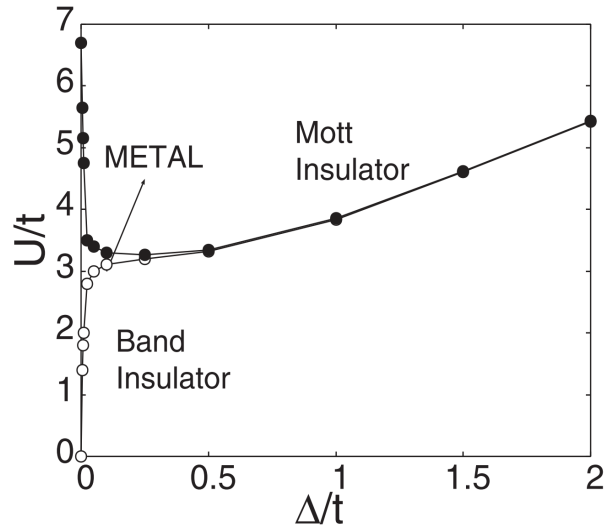


Figure 1.7: The $\Delta - U$ phase diagram found from DMFT study of IHM in the Ref.[48] at $T = 0$. The line between band insulator and Mott insulator is the metallic instability.

refer to the conduction and valance band respectively. The ionic Hubbard model (IHM) which is the extension of the Hubbard model was introduced by Nagaosa *et. al.* and used to study the charge transfer physics in organic crystals [20] as mentioned in the beginning of the chapter. Then the model was studied examining various aspects of physics.

(i) $t' = 0$ studies: The first DMFT study of half-filled IHM on square lattice by Garg *et. al.* showed that correlation can actually drive the band insulating phase induced by the staggered potential to metal and then to a Mott insulator at $T = 0$ [48]. This investigation shows that interaction leads to closing of single particle charge gap instead of opening a gap which typically happens in the most cases. It is important to mention that the metal emerging out of the interplay of correlation and ionic potential is an instability in between Band and Mott insulator as seen from the phase diagram in Fig.1.7 obtained in Ref.[48]. The Determinantal Quantum Monte Carlo (DQMC) study of the model at half-filling on square lattice by Scalettar *et. al.* also confirms the existence of the intermediate metal[49]. But in their investigation they found a wide metallic window rather than sliver as seen in Fig.1.7. This however could be due to the fermion sign problem that limited

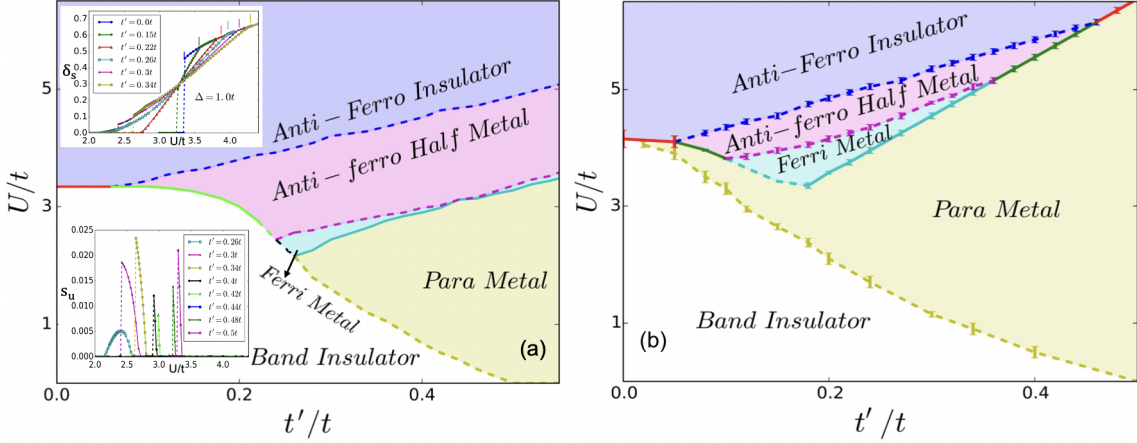


Figure 1.8: The $t' - U$ phase diagram found from Hartree-Fock (HF) in panel (a) and DMFT in panel (b) in the Ref.[47] at $T = 0$. In the inset of panel (a), differential sublattice magnetization, δs (top inset) and uniform magnetization, s_u (bottom inset) obtained from HF calculation are plotted as a function of U/t for different t' and fixed $\Delta (= 1.0t)$ as indicated.

the DQMC calculations to $0.05t$. The window could have narrowed down at lower temperatures. The metallic state remained controversial as CDMFT study[50] found a bond ordered solid instead of a metal. At present the consensus is that the metal is preempted by an antiferromagnetic insulator (provided magnetic order is allowed in the calculation.)[51]. Thus new avenues were looked into for stabilizing the metallic state.

(ii) *Stabilizing the metal* : The first attempt to stabilize the metallic state was by means of doping. The study of IHM has been done by Garg *et. al.* within the DMFT framework showed that indeed one can not only stabilize the metal, in fact a ferrimagnetic half-metallic window was found by doping the system[52]. More recently, in the presence of nnn hopping which acts as source of frustration, the IHM was investigated on a square lattice at half-filling by Bag *et. al.* [47]. In their combined study using Hartree-Fock mean field theory and DMFT with CTQMC as impurity solver, they found three kind of metallic phase, paramagnetic, ferrimagnetic and anti-ferromagnetic in between the band and Mott insulator at $T = 0$ for intermediate t' regime as shown in the panel (a) and (b) in Fig.1.8 in the HF and DMFT respectively. The mean field phase diagram can be constructed

by tracking δ_s , s_u and δn defined in Eq.1.38 as a function of U, Δ and t' after a standard self consistency procedure. δ_s and s_u plotted against U/t for $\Delta = 1.0t$ for different t' values as indicated, are shown in the top and bottom insets respectively in panel (a). We clearly see that beyond a critical t' , the a metallic window opens up, but is a lot richer than a simple paramagnetic metal as was found in the original study [48]. We also observe that remarkably the Hartree-Fock and the DMFT phase diagrams match qualitatively, quite well.

In the above investigations of IHM using various numerical techniques, the finding was that of a half-metal at $T = 0$ sandwiched between the small U band and large U Mott insulator. The 100% spin polarization of half-metal occurs absolutely at zero temperature. Although finite temperature study of IHM has been performed but still its not clear about the thermal depolarization of the $T = 0$ half-metal. This is particularly true because of analytic continuation issues with imaginary time impurity solvers at finite temperatures in calculating real frequency quantities such as spin dependent density of states and conductivity. Thus, our semi-classical approach is ideally suited for the finite T study, particularly given the good qualitative match of the T=0 Hartree-Fock and DMFT phase diagrams. While we started out with the modest goal to study the finite temperature fate of the half metallic state reported above, we discovered a novel half metal what is obtained by heating the Mott insulator. We discuss our results for the IHM in chapter 4.

Chapter 2

Model and Numerical Methods

As discussed in the previous chapter, the Hubbard model being the prototypical model for strong correlation physics has been investigated purely from a theoretical standpoint as well as has remained as one of the most active playgrounds to study a number of non-trivial many body phenomena in strongly correlated materials.

Study of the model and its variants have shed light on phenomenon like the pseudogapped phase in doped cuprates [53] [54] and high- T_c superconductivity [55] [56], Mott-metal transition[57] [58], half-metals [51], non-Fermi liquid behavior in the heavy fermionic systems [59] [60], rare earth nickelates [61] [62] [63] and layered dichalcogenides [64], name a few. For these studies a plethora of techniques have been employed. In this chapter we will briefly summarize a number of such techniques and end with a detailed discussion of a recent semi-classical Monte-Carlo approach that has been used in this thesis. The Hubbard model has been studied using various techniques such as Hartree-Fock Mean-Field theory (HF)[42]-[44] , Exact Diagonalization (ED)[65] [66], Lanczos[67][68], Density Matrix Renormalization Group theory (DMRG)[69] [70], Determinantal Quantum Monte Carlo (DQMC)[71] [42], variational calculation[72][73], Dynamical Mean Field Theory (DMFT)[74][17][75][76][77], slave boson theory[78], Gutzwiller projected wave-function method[43][79], many-body perturbation theory[80] [81] [82] . As it is well known that all the listed techniques have there respective advantages and shortcomings.

We summarize the most popular ones below:

(i) *Exact Diagonalization*: In ED the matrix representation in the many body Hamiltonian is diagonalized by brute force. But as the Hilbert space grows exponentially (4^N) with the system size N increase for spin half fermions, it is impossible to handle reasonable system sizes using current computing resources. Hence, the method is restricted to small system size for one orbital Hubbard model. For multi-orbital systems, the size limitation becomes even more severe. For Lanczos, the many body ground state is iteratively approximated by dropping insignificant states. Its system size limitations is less severe compared to ED but the method typically loses out on the excitation spectrum.

(ii) *Hartree-Fock mean field theory*: Hartree-Fock mean field theory is one of the easiest approaches to get some insight into characteristics of the system by the study this kind of model. In this minimal theory, the actual many body interaction is approximated by a one body theory coupled to the mean fields by dropping all quantum fluctuations[83], as we have discussed in the introductory chapter. Hence the theory becomes an effective one body problem. It gives a mean-field ground state of the system after minimization of the energy or within a self consistency scheme. It has different flavors of approximation like restricted and unrestricted mean field theories. For the case of restricted Hartree-Fock mean field theory, the average values of the order parameters are considered to be same for all the sites. Whereas in the unrestricted case those are distinctly calculated for all the sites. Hence the unrestricted theory is a better approximation to the many particle ground state at zero temperature as it incorporates spatial fluctuations. Use of the approach at finite T , where the temperature enters through the Fermi function for computing average values gives incorrect results. For example, it can not capture the non-monotonic dependence of T_N with U , preformed local moment, Mott insulator, physics of doped Mott insulator for one band Hubbard model.

(iii) *Dynamical Mean Field Theory*: DMFT is a non-perturbative impurity+bath based approach to study strongly correlated systems[84]. Unlike Hartree-Fock mean field theory, DMFT contains charge and spin fluctuations at the impurity site.

It has been used extensively for studying a large class of strong interacting electron systems, with no limitation of the interaction strength or filling and over a wide temperature ranges. The method is exact for lattice with infinite coordination or infinite dimensions. However, the impurity based method cannot capture momentum resolved quantities and extensions such as DCA(Dynamical Cluster Approximation) and CDMFT (Cluster DMFT) (K-space and real space cluster generalizations) are comparatively very expensive. But currently, in DCA, the cluster size can be increased up to 64 sites[16] which was a limitation few years back. Also as in any quantum impurity based method, a good impurity solver is essential. These are numerically costly and are typically formulated in imaginary frequency. The analytic continuation to real frequency for real frequency dependent quantities such as density of states is troublesome , as is well known in the use of the Maximum Entropy method.

(iv) *Density Matrix Renormalization Group*: DMRG approach is based on efficient truncation of Hilbert space using quantum entanglement[85]. It is restricted to low (one or quasi one) dimensional systems of strongly correlated electrons. Although the truncation of Hilbert space allows to access larger system, it becomes inefficient except for one dimension or ladder like systems due to the area law of growth of entanglement entropy. In a bipartite system the entanglement between the sub-parts is proportional to the boundary area. In 1 dimensional lattice the ‘area’ is simply a link and a line in 2D and so on. This growth of entanglement proportional to the boundary rather than the volume of the bulk of the sub-system is called to area-law of entanglement and is measured in terms of the entanglement entropy [Rev. Mod. Phys. **77** (1 2005), pp. 259–315].Although, the technique is usually restricted to zero temperature but progress of the field made it possible to go finite temperature[86][87].

(v) *Determinantal Quantum Monte Carlo*: DQMC incorporates both quantum and thermal fluctuation. It is based on the Hubbard-Stratonovich (HS) transformation of the Hubbard interaction which is exact and a Monte Carlo procedure to anneal the HS auxiliary fields[88]. Also in this method, the system size can be

accessed reasonably larger compared to ED. Hence it can be deployed for one as well as multi-orbital Hubbard model. Along with these advantages, DQMC has a serious limitation. DQMC based Monte-Carlo suffers from the infamous fermion sign problem where the probability of acceptances of HS fields becomes negative, except for special cases like the half-filled Hubbard model. Away from half-filling and the cases when longer range hopping which breaks the particle-hole symmetry, the sign problem is severe. The fermion sign problem becomes more severe at low temperatures and for large system size. Owing to antisymmetry of the many-fermion wave-function, the Monte-Carlo acceptance rate in DQMC can turn negative. This can be quantified by the average sign of the acceptance rate. When the average sign approaches zero, the Monte-Carlo becomes unstable. This is known as the fermion sign problem, which increases with system size and with lowering temperature [Brazilian Journal of Physics, **33**, 1, (2003)]. The method is otherwise exact in the absence of sign problem. However, the sign problem limits the investigations of Hubbard model to high and intermediate temperatures.

(vi) Semi-classical Monte Carlo: In this thesis we have used a recently developed numerical technique called semi-classical Monte-Carlo approach (s-MC)[89] [90] to study the Hubbard model and its variants at finite temperatures. Like DQMC in s-MC the two body Hubbard interaction term is decoupled through Hubbard-Stratonovich transformation that allows us to write the interaction term as non-interacting fermion coupled to auxiliary fields. But unlike DQMC, in this scheme we only retain the spatial fluctuations of the auxiliary fields, as shown in the schematic Fig.2.1. In the figure, the constant red dashed arrow is the temporal path for auxiliary fields in s-MC, as opposed to in DQMC represented by the black arrows that allows non-trivial time evolution for the auxiliary fields. We will discuss this approximation in detail later in this chapter. Dropping of the fluctuation over time allows to extract effective one body spin-fermion Hamiltonian. The many body effect and thermal fluctuation enter in the calculation through the spatial distribution of auxiliary fields. The method at $T = 0$ tends towards unrestricted Hartree-Fock mean field theory. But at finite temperature, it exhibits qualitatively good result and it

progressively becomes accurate as temperature increase in the thermally dominated regime. s-MC compares well with DQMC in a wide temperature window. It is numerically inexpensive and allows access to large system sizes.

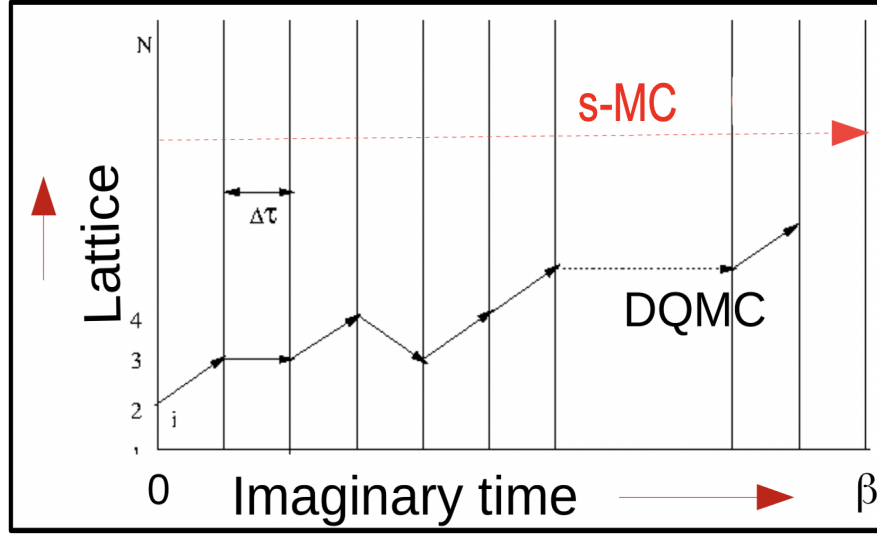


Figure 2.1: Imaginary time slice and temporal path for s-MC and DQMC shown by the red dashed arrow and black arrows respectively

2.1 Inhomogeneous Mean Field theory

Since s-MC reduces to unrestricted Hartree-Fock at low temperatures, we derive (in Appendix D) the inhomogeneous mean-field Hamiltonian in real space. This complements the k-space mean-field theory discussed in chapter 1. This also will be useful to contrast the Hartree-Fock Hamiltonian and the closely related effective Hamiltonian of the semi-classical Monte-Carlo approach.

The Mean-Field (MF) Hubbard Hamiltonian in real space have the following form, found from Appendix D.

$$H^{HF} = -t \sum_{\langle ij \rangle, \sigma} c_{i\sigma}^+ c_{j\sigma} + \frac{U}{2} \sum_i [n_i \langle n_i \rangle + 2 \langle \vec{S}_i \rangle^2 - 4 \vec{S}_i \cdot \langle \vec{S}_i \rangle - (1/2) \langle n_i \rangle^2] \quad (2.1)$$

2.2 Semi classical Monte-Carlo Technique

Our goal in this thesis is to study the Hubbard model at finite temperatures and extract the physics of the model for different circumstances like incorporation of frustration and staggered potential. For the derivation of the semi-classical Monte-Carlo approach we follow recent literatures[89] [90]. The detailed derivation to get to the effective one body spin-fermion Hamiltonian is given below followed by the exact diagonalization + classical Monte-Carlo scheme (ED+MC) for solving the s-MC effective Hamiltonian. To reduce the numerical cost and access larger system size we use Travelling Cluster Approximation (TCA)[91]. The details of TCA are discussed after we present the s-MC scheme.

2.2.1 Derivation of H_{eff} in the semi-classical approach

The Hubbard Hamiltonian is

$$H = H_0 + H_U = -t \sum_{\langle ij \rangle, \sigma} (c_{i\sigma}^\dagger c_{j\sigma} + hc) + U \sum_i n_{i\uparrow} n_{i\downarrow} - \mu \sum_i n_i \quad (2.2)$$

Where, t is the nearest neighbor hopping amplitude (which sets the energy scale, so we take $t=1$ throughout this thesis), U is the on site Hubbard interaction and i runs over the sites on the two dimensional square lattice and μ is the chemical potential introduced to fix the particle number in the system. Here $c_{i\sigma}^\dagger$ ($c_{i\sigma}$) is the electron creation (annihilation) operator and $n_{i\sigma}$ is the number operator for σ spin at a site i .

Now, our goal is to simplify the two body Hubbard interaction term. For setting up the formalism we write the interaction term through the exact transformation as the square of number n and spin \mathbf{S} operator as the following rotational invariant form.

$$n_{i,\uparrow} n_{i,\downarrow} = \frac{1}{4} (n_i^2) - (\mathbf{S}_i \cdot \hat{\Omega}_i)^2. \quad (2.3)$$

Where, the spin operator is $\mathbf{S}_i = \frac{\hbar}{2} \sum_{\alpha,\beta} c_{i,\alpha}^\dagger \sigma_{\alpha,\beta} c_{i,\beta}$, $\hbar = 1$, $\{\sigma^p; p = x, y, z\}$ are three Pauli matrices, and $\hat{\Omega}$ is an unit vector along arbitrary direction. To reach to the above identity, use the identity: $(\mathbf{S}_i \cdot \hat{\Omega}_i)^2 = (S_{i,x})^2 = (S_{i,y})^2 = (S_{i,z})^2$. The above identity simplified by the Hubbard-Stratonovich (HS) transformation gives the proper Hartree-Fock saddle point. The partition function for Hamiltonian, H is $Z = Tr e^{-\beta H}$. The trace is taken over the occupation number basis. The inverse temperature is $\beta = 1/T$, where k_B is 1. The window $[0, \beta]$ is sliced to M number of segment having interval width $\Delta\tau$, or equivalently $\beta = M\Delta\tau$. In the limit $\Delta\tau \rightarrow 0$ by using Suzuki-Trotter decomposition, we can write $e^{-\beta(H_0+H_1)} = (e^{-\Delta\tau H_0} e^{-\Delta\tau H_1})^M$ to the first order in $\Delta\tau$. For a given time slice 'l' the exponential of $(-\Delta\tau)$ times the interaction term is written by using HS transformation to the following form:

$$const. \times \int d\phi_i(l) d\Delta_i(l) d^2\Omega_i(l) \times \\ e^{-\Delta\tau[\sum_i(\frac{\phi_i(l)^2}{U} + i\phi_i(l)n_i + \frac{\Delta_i(l)^2}{U} - 2\Delta_i(l)\hat{\Omega}_i(l)\cdot\mathbf{S}_i)]}$$

Here the auxiliary fields $\phi_i(l)$ and $\Delta_i(l)$ are introduced through the HS transformation which couple to the charge density and spin operator respectively at every site i . We define a new vector auxiliary field $\mathbf{m}_i(l)$ which is the product $\Delta_i(l)\hat{\Omega}_i(l)$ at each site. Then we can rewrite the full partition function as following

$$Z = const. \times Tr \prod_{l=M}^1 \int d\phi_i(l) d^3\mathbf{m}_i(l) e^{-\Delta\tau[H_0 + \sum_i(\frac{\phi_i(l)^2}{U} + i\phi_i(l)n_i + \frac{\mathbf{m}_i(l)^2}{U} - 2\mathbf{m}_i(l)\cdot\mathbf{S}_i)]} \quad (2.4)$$

In the above equation the integrals are taken over $\{\phi_i(l), \mathbf{m}_i(l)\}$ and a time order product of M time slices from M^{th} to 1 is used. The differential for the vector auxiliary field $\mathbf{m}_i(l)$ is written as $d^3\mathbf{m}_i(l)$. At this stage the partition function is exact. We now make approximation by dropping time dependence and keeping only spatial fluctuation of the auxiliary fields. By doing so and using the saddle point value of the auxiliary field $\phi_i(l)$ we extract the effective one body Hamiltonian H_{eff} . If we keep ϕ_i and treat as the auxiliary field in the Monte-Carlo, it is clear from

Eq.2.4 that it breaks the Hermiticity of the Hamiltonian as the term with ϕ_i linearly coupled to n_i is imaginary. Further we also re-scale $\mathbf{m}_i(l)$ as $\frac{U}{2}\mathbf{m}_i$. From here on we will refer to auxiliary field as (Aux. F) which basically refers to m_i . Finally, the form of the effective Hamiltonian looks like following

$$H_{eff} = H_o + \frac{U}{2} \sum_i (\langle n_i \rangle n_i - \mathbf{m}_i \cdot \sigma_i) \quad (2.5)$$

$$+ \frac{U}{4} \sum_i (\mathbf{m}_i^2 - \langle n_i \rangle^2) - \mu \sum_i n_i$$

We would like to point out that if we replace the Aux. F m_i in the Eq.2.5 by the average value of the spin operator, we would get back the HF mean field Hamiltonian given in the Eq.2.1. Hence at $T = 0$ our effective Hamiltonian H_{eff} reduced to HF theory. In s-MC, the Aux. F are variables that, at finite temperature can take arbitrary values and not restricted to the mean-field values, we obtain in a Hartree-Fock theory.

The summary of the scheme of the semi-classical approach is given in the flowchart in Fig.2.2.

2.2.2 Details of the Monte-Carlo procedure

Now, to solve the effective Hamiltonian H_{eff} found above, we use ED coupled with classical Monte-Carlo (MC) in the background of classical auxiliary fields $\{\mathbf{m}_i\}$ randomly generated from the random number generator. We use the Metropolis scheme to update auxiliary fields sequentially on the lattice and generate thermalized configurations. The Metropolis algorithm is given in the steps below.

1. We initialize the Aux. F m_i background randomly and an uniform $\langle n_i \rangle$ distribution.
2. We diagonalize the Hamiltonian in the background of the random Aux. F. and compute energy E_p .
3. We propose an update at a site i for the Aux. F m_i .
4. We rediagonalize the Hamiltonian (with the update) and calculate energy

Semi-classical Monte-Carlo technique

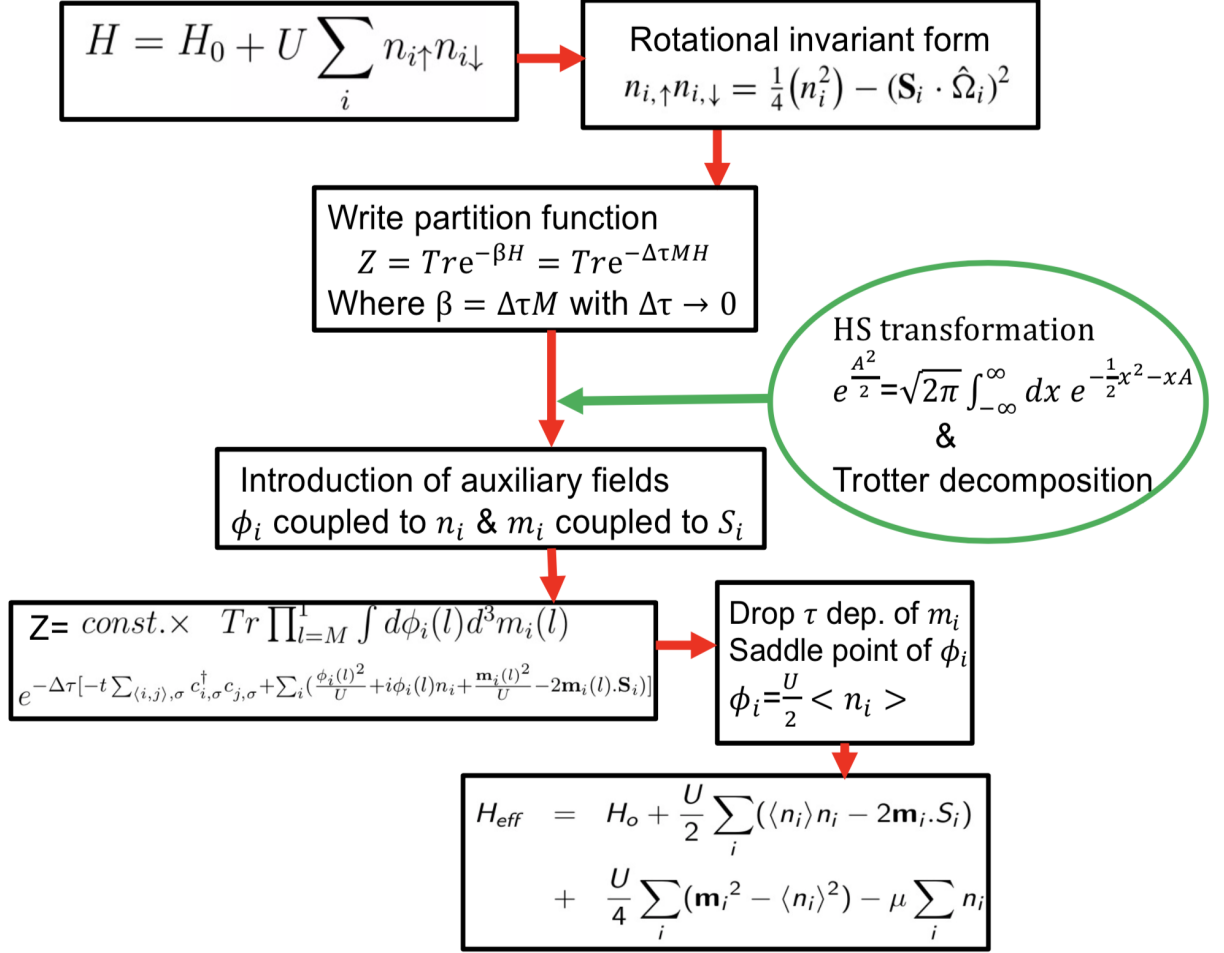


Figure 2.2: Flow chart of the semi-classical Monte-Carlo scheme.

E_c .

- Now if $\Delta E (= E_c - E_p) \leq 0$ then the changed Aux. F will get accepted.
- If $\Delta E (= E_c - E_p) > 0$, the update is accepted with the probability $\exp(-\beta \Delta E)$
- We repeat the steps 3-6 by visiting each site of the system sequentially until we cover all the sites (one Monte-Carlo system sweep).

8. We calculate $\langle n_i \rangle$ self-consistently in the fixed MC configuration for every 10th MC sweep to allow the charge to distribute to readjust to the change of the Aux. F.

Let us elaborate this step in some detail. In the Monte-Carlo calculation the Hamiltonian is a functional of the $\{m_i\}$ fields and the average local densities $\{\langle n_i \rangle\}$.

The Monte-Carlo update of the $\{m_i\}$ fields is split into two parts at any given temperature, say T_k . The average local densities $\{\langle n_i \rangle\}$ are either chosen randomly at the highest temperature (T_h) starting point of the calculation or inherited from the previous (immediate higher temperature point) if $T_k < T_h$. We first perform 10 Monte-Carlo system sweep keeping the local densities $\{\langle n_i \rangle\}$ s fixed. We then stop the update of the $\{m_i\}$ fields and perform a self-consistency in the local densities. Once the local densities have converged, we then hold these densities fixed and perform another 10 Monte-Carlo sweeps. This slow two-stage process is continued for all thermalization Monte-Carlo system sweeps. We have checked that continuing the process beyond thermalization does not modify observables calculated.

9. We perform sufficiently large number of Monte-Carlo sweep (repeat the steps from 3-8) until the system gets thermalized for a given temperature.

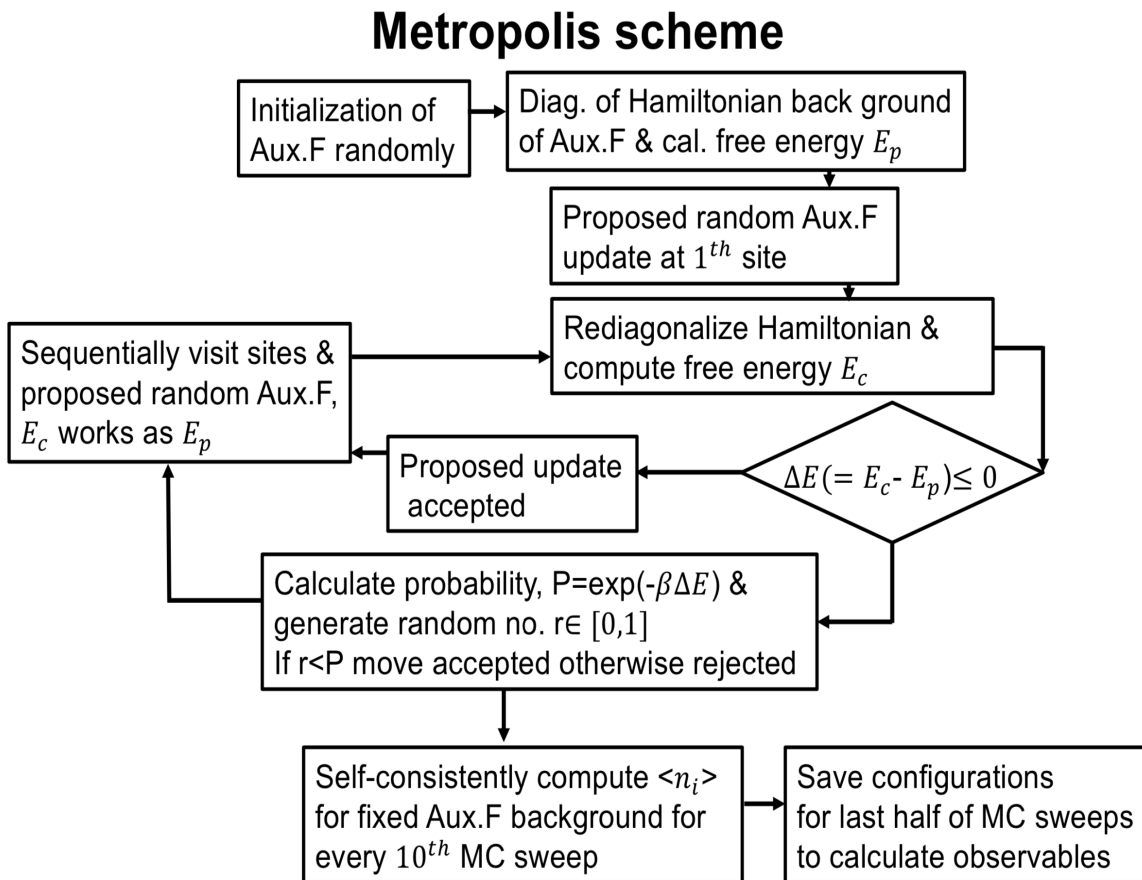


Figure 2.3: Flow chart of the Metropolis scheme.

We start the MC from high T and reduce the temperature in small steps so that the system doesn't get trapped in local minima up to very small T. The information of the thermal fluctuation gets encoded in the equilibrium classical auxiliary field configurations. To get the thermalized configurations we first leave half of the Monte-Carlo sweep annealing for a given temperature and the last half of MC sweep configurations will be saved for calculations. To avoid auto correlation between the configurations due to the pseudo-random number generator that is to generate independent auxiliary field distribution we use every 10^{th} configuration of the 2^{nd} half of the MC sweeps to compute thermal averages.

We use single flipping scheme in the Metropolis algorithm in our Monte-Carlo procedure. There are various cluster flipping schemes to basically avoid critical slowing down close to phase transition such as the Wolf algorithm, Swendsen and Wang algorithm and so on. We have checked that our single flip protocol is sufficient to equilibrate the Aux.F.

In our study, we use 4000 MC sweeps out of which the first 2000 are utilized for thermalization of the system and for every 10^{th} MC sweeps we have self-consistently calculated $\langle n_i \rangle$ in the fixed Aux. F background. The last half (2000) configurations are employed for computing physical observables. We use every 10^{th} configuration of the later 2000 MC sweeps for evaluating thermodynamic quantities to avoid auto correlation. Here, the equilibration is determined by plotting the average energy of the system as a function of Monte-Carlo system sweeps, where equilibration corresponds to the MC steps at which the average energy settles to a constant value (within numerical accuracy). In all typical cases the equilibrium is achieved earlier than 2000 MC sweeps as seen in the Fig.2.4. In panel (a), the average energy as a function of MC sweep is plotted for half-filled Hubbard model for $U = 4.0t$ and $t' = 0$ at $T = 0.1t$ on a 16^2 square lattice with 4000 MC sweeps. We have also presented for correlations, $U = 2.0t$ in panel (b) and $U = 8.0t$ in panel (c) in Fig.2.4 at temperature, $T = 0.05t$ for the same system size using same MC sweeps. The data are shown for $t' = 0$ with black and finite t' ($t' = -0.3t$) with red colour. We see that the burn in time for small U is lesser than for large U in the unfrus-

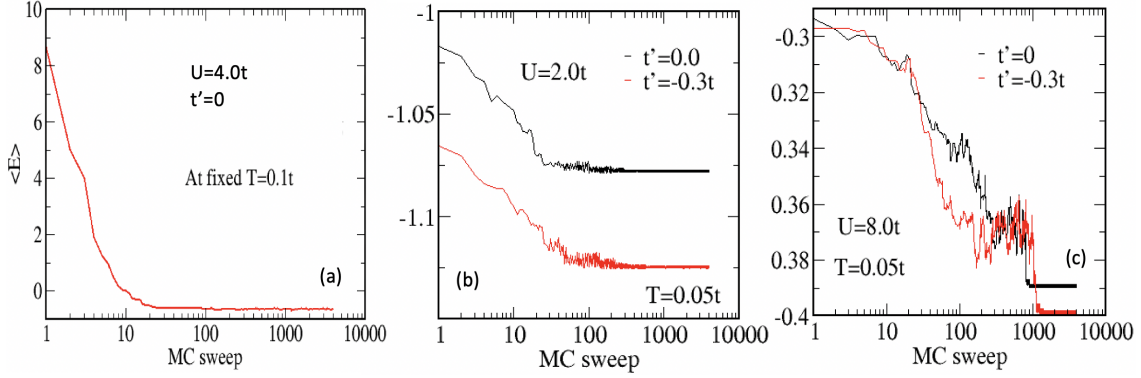


Figure 2.4: This shows the average energy vs MC sweep data found from MC annealing for a 16^2 system size square lattice using 4000 MC sweeps for the case of half-filled Hubbard model for different interaction strengths $U = 2.0t$, $4.0t$ and $8.0t$ shown in panel (b), (a) and (c) respectively for $t' = 0$ and $t' \neq 0$ cases. Panel (a) is presented only for $t' = 0$ case at $T = 0.1t$. Whereas panel (b) and (c) are shown for $t' = 0$ and $-0.3t$ indicated by the black and red colours for above mentioned correlation values at fixed temperature $T = 0.05t$.

trated case. The burn in times are larger in the case of frustration as expected. As we increase temperature number of MC steps to thermalize will be less comparable to low temperature, as at low T the acceptance rate decreases due to small Boltzmann weight which is used as probability of acceptance in the Monte-Carlo procedure. Also it should be mentioned that when the system is highly frustrated for around $t' = -0.8t$ and $U < 20t$ where paramagnetic insulating phase with short range correlation (possibly candidate for spin-liquid (SL)) appears, we have done 40,000 Monte-Carlo sweeps but the result does not change from 4000 Monte-Carlo sweep calculation.

We begin the Monte-Carlo run at $T = 100t$ and decrease T with interval $\Delta T/t = 10$ up to 1. Then, we make the spacing $1.0t$ to reach $T = 1.0t$ from the value $10t$. Then gradually T is lowered to $0.3t$ from $1.0t$ in the step of $0.1t$ and then from that value it is decreased to $0.1t$ with $\Delta T/t = 0.05$. The temperature is reduced to $0.01t$ by an amount of $0.01t$ in every step. Finally, T is further decreased to $0.005t$ with interval $0.001t$ from $T = 0.01t$.

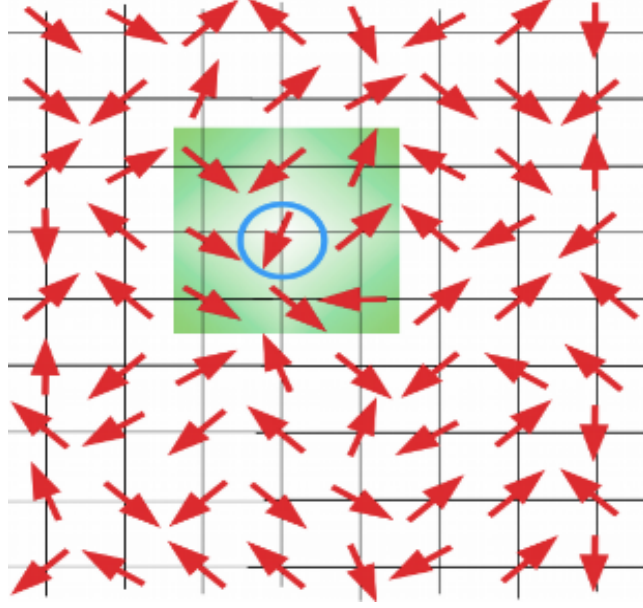


Figure 2.5: Schematic diagram of TCA scheme.

2.2.3 Travelling cluster approximation:

As discussed above in the s-MC approach we need to do exact diagonalization in the background of the Aux. F m_i and $\langle n_i \rangle$ mean field to calculate free energy which is used to accept or reject a proposed update. The diagonalization cost for a system with the total number of sites N goes like N^3 for every diagonalization. Further, a sequential system sweep costs a factor of N . This makes the cost of a single system sweep N^4 which increases up to $10N^4$ for 10 $\langle n_i \rangle$ self-consistency loops, performed after a system sweep. The typical size accessible by this method is $\sim 10^2$ - 12^2 . The Travelling Cluster Approximation (TCA)[91] and its parallelized version [90] allows one to access larger system sizes. In TCA we assume that the effect of a local update (or at a site) for Aux. F does not propagate very far. Thus the Monte-Carlo acceptance/rejection can be decided based on a cluster Hamiltonian built around the site where the update is proposed for the Aux. F. For example, we choose a reference site at which we propose a change of Aux. F as shown by the blue circle around a red arrow in the schematic picture in Fig.2.5. We form the cluster around that central site represented by the green regime. The cluster size N_c is chosen to be smaller than system. Then we get the energy after diagonalizing the cluster

Hamiltonian. This reduces the numerical cost to $N \times N_c^3$. We would like to mention that in our calculation, we have used periodic boundary condition (PBC) for the cluster under TCA scheme following literature [S. Kumar and P. Majumdar Eur. Phys. J. B **50** 571 (2006); Anamitra Mukherjee *et. al* Phys. Rev. E **91** 063303 (2015).]

Using TCA we can access very large system size and till now 40^2 for 2D lattice for the single orbital Hubbard model. In our calculation, we have used 32^2 system size and kept the cluster size as 8^2 . This significantly reduces the cost comparable to the direct (without TCA) 32^2 calculation.

2.2.4 Benchmarks for s-MC

As we have mentioned that the effective Hamiltonian extracted from the formalism becomes unrestricted Hartree-Fock mean field Hamiltonian at $T = 0$. At a finite value of T , the thermal fluctuation is imprinted in the Aux. F and the method exhibits results which is not only qualitatively but quantitatively in agreement with the DQMC study[92].

Fig.2.6 shows the finite temperature $U - T$ magnetic phase diagram found from the half-filled Hubbard model for cubic lattice[89]. The red solid squares are the anti-ferromagnetic $\mathbf{q} = (\pi, \pi, \pi)$ or G-type magnetic order transition temperatures T_N at different U/t values. It is clear that s-MC method captures the non-monotonic behavior of the Neel temperatures, T_N qualitatively matches with the result of DQMC shown by the open squares. It should be also mentioned that this approach captures large U perturbative scaling of T_N of $\sim -O(t^2/U)$ [93]. It also captures the non-trivial preformed local moment region where moments are formed but they are not ordered, obtained upon heating the long range anti-ferromagnetic order. This region is shown in blue. The local moment insulator to paramagnetic metal crossover is shown by the boundary between the blue and the gray regions. In contrast, the finite temperature Hartree-Fock results produce a T_N which grows monotonically with U (blue dashed line) and the entire region below it would be a G-type antiferromag-

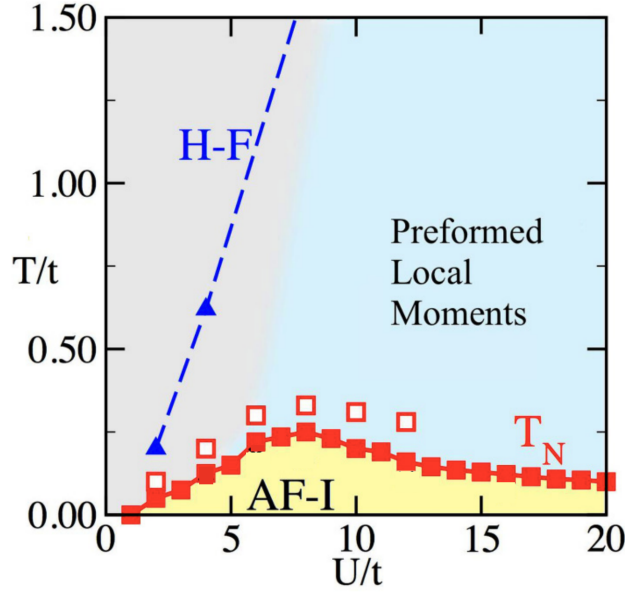


Figure 2.6: Finite temperature $U - T$ magnetic phase diagram. The red solid squares and open squares are the anti-ferromagnetic Neel temperature T_N found from s-MC [89] and DQMC [92] study respectively. The blue dashed line is T_N line got from HF theory. The light blue regime is the preformed local moment regime.

netic insulator. It also does not capture the regime of preformed local moment. Because of the power of capturing rich physics the method is successfully employed for various systems such as one [94] and two orbital Hubbard model[95], Anderson-Hubbard model[96], frustrated[97] and attractive Hubbard model for studying BEC to BCS crossover[98].

we would like to emphasize here, that the Auxiliary fields are sampled through a Monte-Carlo (Metropolis algorithm) that includes the quantum one-body Hamiltonian containing the same Auxiliary fields. Thus a single update at any Monte-Carlo step is not an uncorrelated update, but a correlated one. This is a case of annealed disorder rather than a quenched one. As is well-known in literature, [Phys. Rev. B **49**, 147 (1994); Phys. Rev. Lett. **95**, 126602 (2005)] Anderson localization (localization of single particle states in low dimensions in the presence of random potentials) is suppressed in such cases.

In the next two chapters we will present results for the finite temperature properties of the Hubbard model using s-MC under introduction of longer range hopping

and staggered onsite potentials.

Chapter 3

Frustration and temperature effects at half filling

3.1 Introduction

In this chapter, we will discuss the results of our study of the Hubbard model in the presence of frustration on the square lattice at half-filling. Next nearest neighbor hopping can act as a source of frustration that disrupts long range staggered magnetic order, destabilizes insulating tendency, and can induce new paramagnetic metallic state. In chapter 1 we saw that this deviation from perfect nesting can lead to non-Fermi liquid behavior. In our work, we focus on the finite T metal-insulator and magnetic properties of the $t - t'$ Hubbard model. We will also demonstrate deviations from Fermi liquid behavior and a pseudogapped regime in nnn hopping induced metallic states in the following sense: Since our approach is semi-classical that goes over to the Hartree-Fock approximation as $T \rightarrow 0$, ‘non-Fermi liquid’ behavior in this thesis refers to *deviation from Fermi-liquid driven by thermal fluctuations*. We will however show some exact diagonalization results at $T=0$, that provides clues to the $T=0$ limit.

3.2 $t - t'$ Hubbard model

The $t - t'$ Hubbard model on a square lattice is defined as

$$H = -t \sum_{\langle i,j \rangle, \sigma} (c_{i\sigma}^\dagger c_{j\sigma} + h.c.) - t' \sum_{\langle\langle i,j \rangle\rangle, \sigma} (c_{i\sigma}^\dagger c_{j\sigma} + h.c.) + U \sum_i n_{i\uparrow} n_{i\downarrow} - \mu \sum_i n_i$$

where, $c_{i\sigma}^\dagger$ ($c_{i\sigma}$) are electron creation (annihilation) operators at the site i with spin σ . t and t' are respectively the nearest and nnn hopping amplitudes. We choose $t'/t < 0$ in our study inspired from cuprates. $n_{i\sigma} = c_{i\sigma}^\dagger c_{i\sigma}$ is the number operator for spin σ at a site i and n_i is the spin summed local number operator. U is the local Hubbard repulsion. μ denotes the chemical potential, and is adjusted to maintain half filling. To study the finite temperature properties of the model we use the following observables: static magnetic structure factor S_q , density of states $N(\omega)$, resistivity $\rho(T)$ within the Kubo-Greenwood formalism, local moment distribution in real space $P(M)$, spin-spin correlation in real space, $C(r)$, These indicators are defined in Appendix E.

3.3 Emergent phases at low temperature

The low temperature $U/t - t'/t$ phase diagram is shown in the Fig.3.1 at $T = 0.005t$ obtained by cooling down within the Monte-Carlo protocol discussed in chapter-2. This phase diagram should to thought of as a good approximation to the $T=0$ unrestricted Hartree-Fock phase diagram. As we have discussed in chapter 1, the $\vec{Q} = (\pi, \pi)$ nesting instability is disrupted in presence on t' , so the insulating phase is pushed to finite U_{crit} that depends of the value of t' . There are also interesting magnetic transitions driven by the nnn hopping in the insulating regime. These are discussed below. We would like to emphasize that in 2-dimensions with continuous spin rotation symmetry, there is no true long range order in the thermodynamic limit

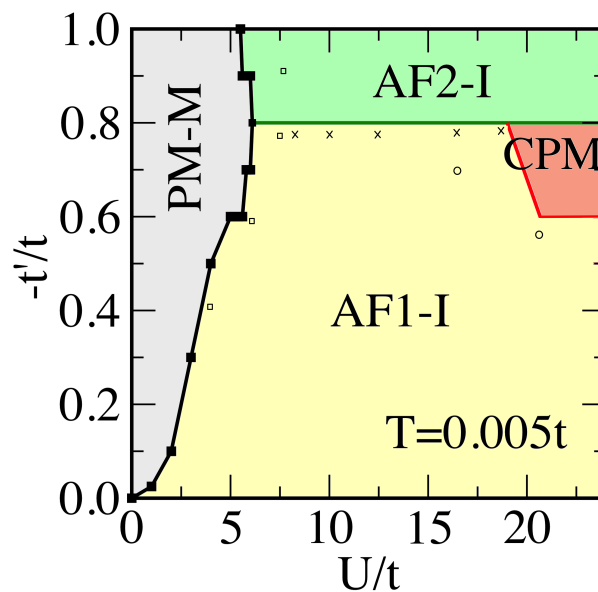


Figure 3.1: Low temperature $U - t'$ phase diagram. The various phases obtained are a paramagnetic metal (PM-M), $\mathbf{q} = (\pi, \pi)$, (G-type) antiferromagnetic insulator AF1-I; $\mathbf{q} = (\pi, 0)/\mathbf{q} = (0, \pi)$, (A-type), antiferromagnetic insulator AF2-I; and a low T correlated paramagnet (C-PM) insulator at large U . For $5.2 < U/t < 6$, there is a re-entrant insulator to metal transition around $t'/t \sim -0.8$. The data was obtained on a 32^2 system. The open circles, crosses and open squares are data reproduced from L. Tocchio *et al.* Phys. Rev. B **78**, 041101 (2008). These are discussed in the text. The phase diagram is calculated at the lowest temperature $T = 0.005t$.

due to the well known Mermin–Wagner theorem[99]. The various T_N , the magnetic ordering scales should be interpreted at the temperature at which magnetic correlation extends over the system size, as is routinely done in 2-dimensional studies of magnetic order[100]. We will however show some data in 3-dimensions to show that our 2-dimensional magnetic scales are reliable indicators of systematics of magnetic tendencies with variation in U and t' .

3.3.1 Description of the phase diagram

The locus of critical values of the interaction (U_{crit}) for transition to a insulator is shown in Fig.3.1 by solid line with filled squares. The dependence on t'/t is evident from the plot. The left side of the line is the region where the metallic phase exists i.e for $U < U_{crit}$ and the right side is the insulating phase ($U > U_{crit}$). The metal-insulator boundary has a non-monotonic dependence on t'/t , with the maximum value of the critical value of the U_{crit} is $6t$ at $t'/t = -0.8$. The insulating phase has magnetic ordering that depends on the value of the frustration (t'). The regime below $t'/t = -0.8$ is a G-type (π, π) anti-ferromagnetic ordering which is shown by the yellow shade. In contrast, the region above $t'/t = -0.8$ has A-type $(\pi, 0)$ or $(0, \pi)$ which is shown in green color. As mentioned above this boundary is constructed based on finite temperature behavior of resistivity. We will discuss this later in the chapter.

The earliest study of the current model by Lin and Hirsch[42] using Hartree-Fock and quantum Monte-Carlo (QMC) numerical techniques says that indeed there exist finite critical values of U in the presence of t' instead of $U = 0$ unlike for case $t' = 0$. The critical value is $U_{crit} = 2.1t$ as found from Hartree-Fock (HF) study but DQMC technique at $t' = 0.2t$ on a system having system size $N = 64$ (8×8 lattice) gives the value $U_{crit} = 2.5t \pm 0.25t$ at half-filling. So, there is a reasonable agreement with HF and DQMC. Also it has been found using HF method that U_{crit} increases with t' within the regime $0 > t'/t > -0.45t$. In our study, we found $2.6t$ as the critical interaction value at the same magnitude next nearest neighbor hopping

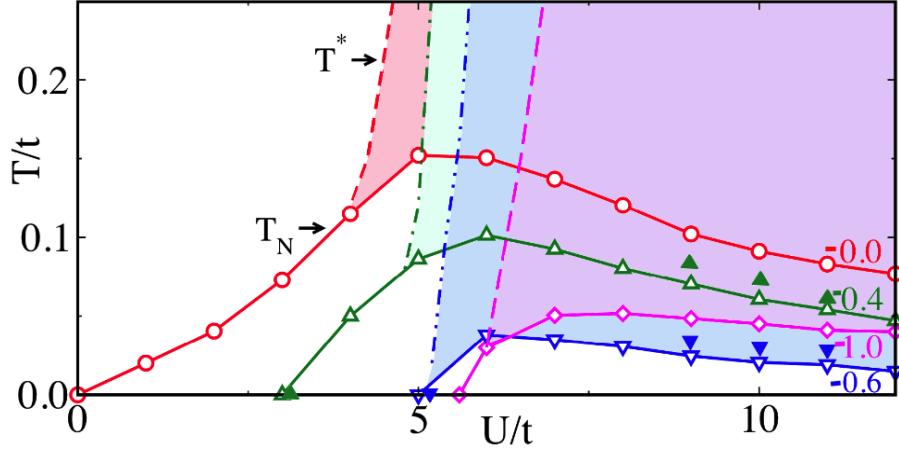


Figure 3.2: This plot shows finite temperature $U/t - T/t$ phase diagram at different t' values. The red with open circles, green with open up-triangles, blue with open down triangles and magenta with open diamonds are the curves of antiferromagnetic Neel temperature T_N for $t' = 0.0, -0.4t, -0.6t$ and $-1.0t$ respectively, plotted against interaction value U/t which are found from the static magnetic structure factor calculation. The parameters are indicated with same colors in the figure. Out of four curves, red, green and blue ($t' = 0.0, -0.4t, -0.6t$) are for $q = (\pi, \pi)$ and the magenta ($t' = -1.0t$) is for $q = (\pi, 0)$ or $q = (0, \pi)$ magnetic ordering. The various dashed and dashed dotted lines are referring T^* scale which is associated with thermal fluctuation evolved Metal-Insulator transition indicated with respective colors.

value. Finally in Fig.3.1 we have added the phase boundaries obtained in literature using Gutzwiller variational approach (L. Tocchio *et al.* Phys. Rev. B **78**, 041101 (2008)). These agree remarkably well with the low T s-MC magnetic and metal insulator phase boundaries. In the Gutzwiller study a possible spin liquid phase (in the region where we find a low-T correlated paramagnet shown in orange) was also reported, unfortunately ascertaining whether our C-PM is a spin liquid or not is beyond the semi-classical approach. However, we will discuss its properties in the next section.

3.4 Magnetic phases at finite temperatures

Now we concentrate on the finite temperature magnetic phases found from our s-MC study. The $U/t - T/t$ phase diagram is presented in the Fig.3.2 for different

t' values. The solid red line with open circles is the anti-ferromagnetic ($q = (\pi, \pi)$) Neel temperature (T_N) for the corresponding U/t values for the $t' = 0$ case. T_N has a non-monotonic dependence on U which agrees with the weak and strong correlation limits as found from the study of the model using perturbation theory[101]. In the strong coupling limit, $\sim O(t^2/U)$ scaling of T_N has been found in our study. For the weak interaction strength, nesting in the Fermi surface for the wave vector $q = (\pi, \pi)$ leads to G-type anti-ferromagnetic ordering in the system at half-filling. The perfect nesting happens for $t' = 0$ when the system exhibits particle-hole symmetry. And T_N for this case goes like the gap $\Delta \sim te^{-2\pi\sqrt{t/U}}$ as in chapter 1. However due to finite lattice and the resulting energy gap in the spectrum, exact form of the nesting induced T_N unfortunately cannot be captured within our approach.

When next nearest neighbor hopping is switched on then not only does the U_{crit} become finite at low T, but also the Neel temperature is suppressed from the case with $t' = 0$ as shown for the green solid line with up-triangle and blue solid line with down-triangle for $t' = -0.4t$ and $t' = -0.6t$. We should note that for $0 > t'/t \geq -0.8$ the system shows $q = (\pi, \pi)$ anti-ferromagnetic correlation. For $t' > -0.8t$ the A-type or $q = (\pi, 0)/(0, \pi)$ anti-ferromagnetic correlations emerge in the system as mentioned before. The solid magenta curve with open diamond is shown as a representative curve of T_N as a function of U for $t' = -1.0t$, for A-type magnetic order. For $t' \neq 0$ case, the scaling of T_N will have both t and t' dependence. Presence of both t and t' leads to nearest neighbor (J_1) and next nearest neighbor (J_2) anti-ferromagnetic super-exchange interactions with $J_1 \sim -\frac{4t^2}{U}$ and $J_2 \sim -\frac{4t'^2}{U}$ [51][47]. The reduction in T_N in comparison to $t' = 0$ case is due to the frustrating J_2 interaction scale. The solid symbols correspond to the structure factor ($S(\pi, \pi, \pi)$) for 3D lattice (8^3 system) that are free of Mermin-Wagner issues.

As typical examples, the static magnetic structure factor is presented at various t' values are shown for $U = 4.0t$ in Fig.3.3 (a) and for $U = 8.0t$ in Fig.3.3 (b). The red line with circle in the Fig.3.3 (a) shows $S(\pi, \pi)$ with the magnetic transition temperature ($T_N = 0.125t$) for $U = 4.0t$ and $t' = 0$. Now, if we switch on the t' , T_N gets suppressed as for the case $t' = -0.4t$ shown by the green line with up

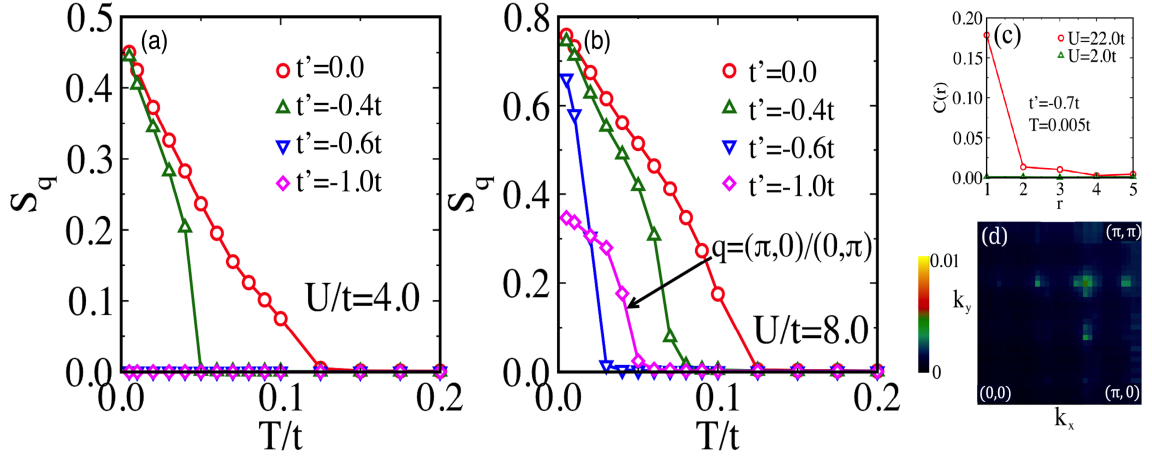


Figure 3.3: In the figure, panel (a) shows static magnetic structure factor as function of temperature for $U = 4.0t$ for the frustration values as indicated in the panel with respective colors. Panel (b) represents also static magnetic structure factor plotted against T for $U = 8.0$. Here red, green and blue are for (π, π) magnetic ordering whereas the magenta is for $(q = (\pi, 0)/q = (0, \pi))$ magnetic ordering. The parameters are mentioned in the panel with same color schemes. (c) shows the real space spin correlation $C(r)$ as a function of the Manhattan distance, $r = \sum_{i \in \hat{x}, \hat{y}} |r_i|$, between the spins, at $T = 0.005t$. The data is shown for $U/t = 2$ and 22 and $t'/t = -0.7$. (d) shows the momentum space map of S_q for $U/t = 22$ at $T = 0.005t$. All results are shown for 32^2 real space system.

triangle. Further increase in the frustration value shown here for $t' = -0.6t$ and $-1.0t$ with blue triangle and magenta diamond, leads to complete collapse of the magnetic ordering. Whereas for $U = 8.0t$ in Fig.3.3 (b) T_N for zero frustration value is $\sim 0.125t$ given by the red curve with circles. The (π, π) order is lost for $t'/t < -0.8$. Typical data is presented for $t' = -0.4t$ and $t' = -0.6t$ by green line with up triangle and the blue line with down triangle respectively. These have the transition temperatures $0.08t$ and $0.02t$ respectively. Beyond $t' = -0.8t$, A-type ($q = (\pi, 0)$ or $q = (0, \pi)$) magnetic ordering emerges in the system, the corresponding structure factor for $t' = -t$ is shown by magenta line with diamond in Fig.3.3 (b). (c) shows the real space correlation between spins $C(r)$ at low temperature for $U = 2t$ and $U = 22t$ at $t' = -0.7t$. $C(r)$ is defined in the Appendix E. (d) shows the structure factor map for all \mathbf{q} values in the first Brillouin zone at low temperature for $U = 22t$. The corresponding map for $U = 2t$, the usual paramagnetic state is homogeneous (not shown). We clearly see that the C-PM phase has short range

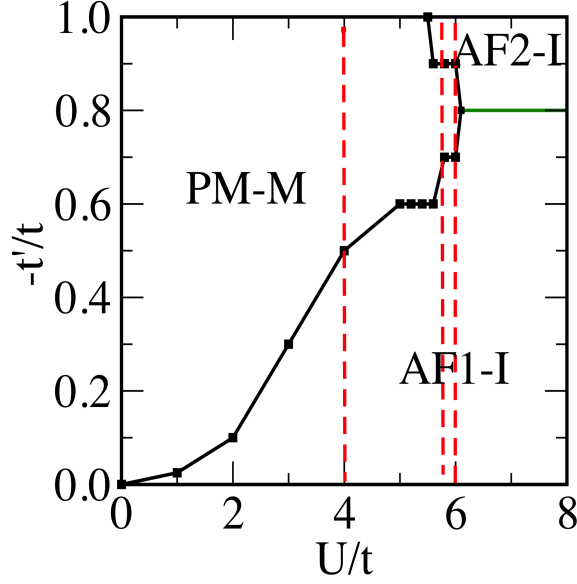


Figure 3.4: Enlarged form the low temperature phase diagram given in the fig-1. The three dashed lines are guide to the eye for different U/t values as 4.0 5.6 and 6.0.

spin correlations but no long range order.

3.5 Frustration induced phase transitions

3.5.1 Re-entrant metal-insulator transition at low T

The magnified version of the low temperature phase diagram with smaller window over U/t and keeping t'/t range fixed, reproduced from the full phase diagram in Fig.3.1, is presented in the Fig.3.4. The phase diagram shows a PM-M phase on the left side of the solid line. On the right side of the line, there are two magnetic insulating phases. The AF1-I is the G-type anti-ferromagnetic insulating phase for $0 > -t'/t \geq 0.8$ and for $-0.8 > t'/t \geq -1.0$ the is AF2-I, A-type anti-ferromagnetic insulator. The red dashed lines are the guide to the eye, representing fixed U cross-sections of the phase diagram at $U = 4.0t$, $5.6t$, and $6.0t$. We will discuss the metal-insulator transition with the help of density of states (DOS) for these U/t values. We start with $U = 4t$ for which DOS is presented in Fig.3.5 (a). When

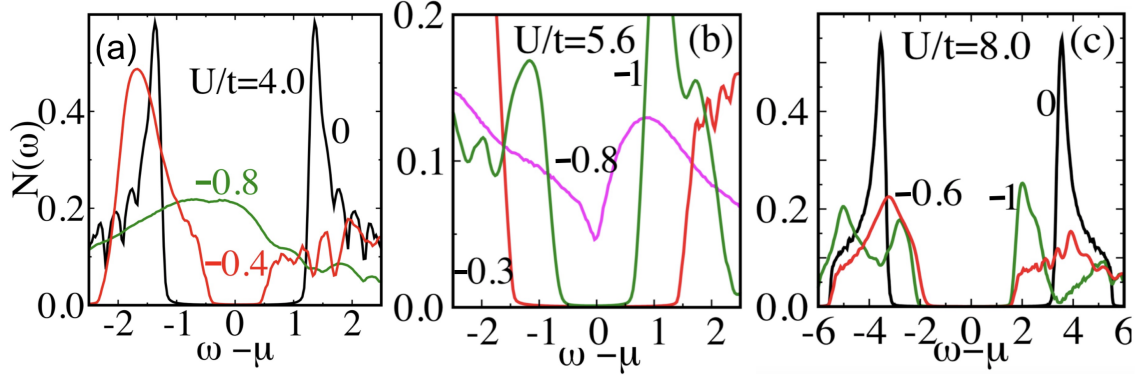


Figure 3.5: This figure shows the density of states (DOS) for three values of U , $4.0t$, $5.6t$, and $8.0t$ in the panels (a), (b), and (c) respectively. In (a), the DOS for $t' = 0$, $-0.4t$ are insulating and for $-0.8t$ is metallic as depicted by the black, red, and green lines respectively. In panel (b) the red and green are for $t' = -0.3t$ and $-1.0t$ respectively which are gapped but the magenta for $t' = -0.8t$ has a pseudo-gap at the chemical potential, referring to the re-entrant metallic phase. The panel (c) shows that DOS for $t' = 0$, $-0.6t$ and $-1.0t$ with black, red, and green solid lines respectively as indicated in the figure are all gapped and this refers to the MI phase.

$0 \geq t'/t > -0.5$, in the yellow regime the DOS is gapped as shown by representative black and red curves at $-t'/t = 0.0$ and 0.4 respectively (corresponding phase is Mott insulating with G-type magnetic order) and in the window $-0.5 > t'/t \geq -1$ (gray region) the DOS is gapless which is shown by the green curve at $t'/t = -0.8$ (metallic phase). At low T for $U = 5.6t$ in Fig.3.5 (b), DOS shows gapped behavior below $t'/t = -0.7$ which lies under the solid line (the Mott phase shown in the phase diagram in Fig.3.4) given by the red line at $t'/t = -0.3$. With increasing the $|t'/t|$, the Mott gap decreases and becomes zero (close to $t'/t = -0.7$), and beyond that value of frustration, a pseudo-gapped DOS develops which is indicated by the magenta curve at $t'/t = -0.8$. Further increase of frustration makes the DOS gapped again, as shown by the green curve for $t' = -t$. This leads to 're-entrant' insulator-metal-insulator transition. The two gapped DOS are for (π, π) and $(\pi, 0)/(0, \pi)$ magnetic ordering for $t'/t < -0.7$ and $t'/t \sim -1$ respectively. The intermediate metal is a pseudo-gapped metal which we will discuss later. For $U = 6.0$ the metallic phase closes (within numerical accuracy) at $t' = -0.8t$. On the both sides of this t'/t value, the system exhibits insulating phase with different magnetic orders (smaller t' shows G-type magnetic order where as larger value give

A-type magnetic order). The re-entrant metal-insulator transition we obtained is in agreement with the previous study[102]. For larger value of the U/t for example 8.0, the DOS is always gapped for any $-t'/t$ as indicated by the representative values 0, 0.6 and 1.0 in the Fig.3.5 (c). The previous study of $J_1 - J_2$ Heisenberg model for $S = \frac{1}{2}$ shows that the G-type and A-type magnetic ordering occur for $J_2/J_1 < 0.4$ and $J_2/J_1 > 0.6$ respectively[103][104]. The intermediate phase in the window between $0.4 \leq J_2/J_1 \leq 0.6$ is a paramagnetic phase (probably a spin liquid state). In our semi-classical approach at large U , we find that the transition from AF1 to C-PM occurs at $t'/t = -0.6$ and then to AF2 occurs at $t'/t = -0.8$ as seen from Fig.3.1 at the largest $U = 22t$ in our calculation. Then using with $J_1 \sim -4t^2/U$ and $J_2 \sim -4t'^2/U$, this implies the AF1 to C-PM transition occurs at $J_2/J_1 \sim 0.36$ and that from C-PM to AF2 happens at $J_2/J_1 \sim 0.64$. These are in close agreement with the above mentioned J_2/J_1 ratios for the same transitions for the $J_1 - J_2$ Heisenberg model.

3.5.2 Metal-insulator transition at finite T

At low T we have seen that U_{crit} for Mott transition depends non-trivially on t' that includes a non-monotonic dependence. We will now focus on the finite temperature metal-insulator transition by presenting $t' - T$ phase diagrams in the top row of Fig.3.6 from panel (a) to (c) for $U = 4.0t$ $5.6t$ and $6.0t$ respectively.

In Fig.3.6 (a) for $U = 4.0t$, at $t' = 0$ the phase is G-type anti-ferromagnetic insulating phase with a sizable Néel temperature. As t'/t grows in magnitude, the magnetic transition temperature which is found from the static magnetic structure factor, decreases monotonically as shown by the solid line and finally goes to zero at $t'/t = -0.6$. Here the metal-insulator transition that is also indicated by the solid line, follows the critical T for magnetic transition temperature. The metal-insulator boundary is found from the optical conductivity $\sigma(\omega)$ calculated using the Kubo-Greenwood formula which is given in detail in Appendix E.

It is well known that thermal fluctuation induced filling of the charge gap in

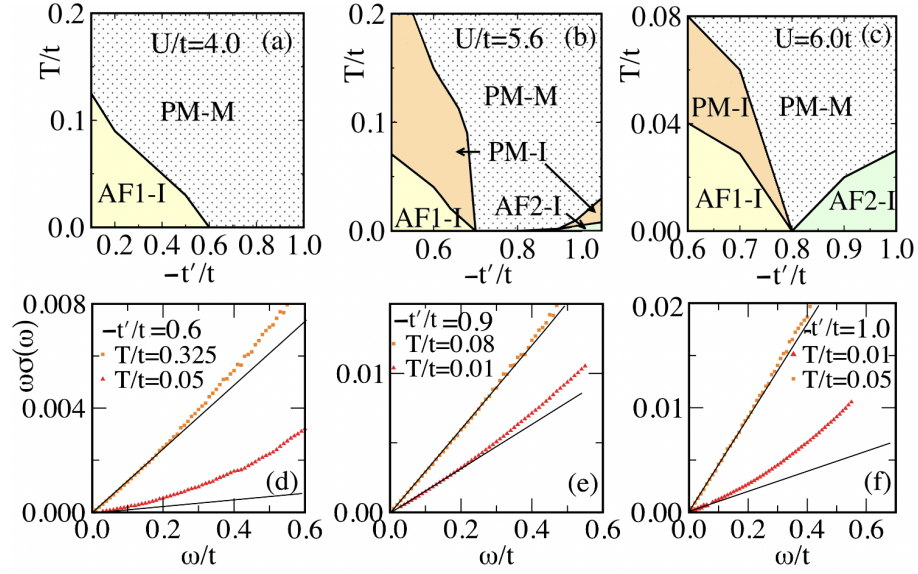


Figure 3.6: (a) to (c) show $t' - T$ phase diagrams for $U = 4.0t$, $5.6t$ and $6.0t$. (d)-(f) show $\omega\sigma(\omega)$ vs ω plots for $t' = 0.6t$, $0.9t$ and $1.0t$ at fixed $U = 5.6t$ shown. In (a)-(c), the yellow regime is the (π, π) insulator (AF1-I) phase. In (b) and (c) the orange regions are paramagnetic insulator (PM-I) and the green regions indicate A-type insulator (AF2-I). The dotted regime is a paramagnetic metal (PM-M) in all three cases. $\omega\sigma(\omega)$ in (d) to (f) are plotted for two temperatures each as indicated. The solid lines are linear extrapolations starting from $\omega/t = 0$ in the lower three panels.

DOS for a Mott insulator does not necessarily imply metallization. For example, the preformed local moment regime above the T_N in the half filled Hubbard model is gapless but insulating. For crossover to metal, the local moments have to collapse. For ascertaining insulator to metal transition driven by temperature we use the low frequency behavior of the optical conductivity. For a metal $\omega\sigma(\omega)$ should behave linearly with ω indicating a constant conductivity as $\omega \rightarrow 0$. This analysis is discussed in detail for the specific case of $U = 5.6t$ is discussed below. For the present case of $U = 4.0t$, the insulator-metal boundary is determined by similar analysis.

For $U = 5.6t$, the G-type anti-ferromagnetic (AF1-I) ordering appears in the window of $t' \in [0, -0.7t]$ at low-T. In the $t' - T$ phase diagram in Fig.3.6 (b), AF1-I is shown by the yellow regime in the t' starting from $-0.5t$ up to $-0.7t$. In this case unlike $U = 4.0t$ in Fig.3.6 (a), magnetic transition and metal-insulator transition do not happen at the same temperature as a function of t'/t . The magnetic ordering temperature shown by the solid black line separating the yellow (AF1-I) to the

orange (paramagnetic insulator, PM-I) regime is smaller compared to the metal-insulator crossover defined by the solid black line in between the orange (PM-I) and the dotted regime. Both the temperature scales decrease monotonically with t'/t and go to zero at $t' = -0.7t$. At higher frustration values, in the window $-0.9t \geq t'/t \geq -1.0t$ a new magnetic phase which has $(\pi, 0)/(0, \pi)$ anti-ferromagnetic order or the A-type magnetic phase (AF2-I) emerges. The critical magnetic and insulator to metal crossover temperatures for this phase have smaller values comparable to the (AF1-I) phase but this scale increases with t'/t going from -0.9 to -1.0. The transition from the AF2-I to PM-M is also not direct but goes a PM-I shown by the orange region. The intervening t' window, $-0.7t > t'/t > -0.9t$ is metallic at low T in s-MC and fan out with temperature increase. In the low temperature $U - t'$ phase diagram in Fig.3.4, the metallic phase closes at the largest value of $U_{crit} = 6.0t$ for $t' = -0.8t$. The finite temperature extension of the phase is shown in the $t' - T$ phase diagram in Fig.3.6 (c). It is similar to that for $U = 5.6t$ except that the metallic region closes within the numerical accuracy at low T . This overall behavior is due to the re-entrant I-M-I transition at low temperature.

Determining metal insulator boundary at finite temperatures: We close this subsection by briefly discussing the approach for determining insulator-metal boundary at finite temperature. As mentioned before to extract the metal-insulator phase boundaries, we compute the optical conductivity and check the linearity and non-linearity of $\omega\sigma(\omega)$ in the limit $\omega \rightarrow 0$. Therefore, $\omega\sigma(\omega)$ vs ω are plotted at three t'/t values -0.6 , -0.9 and -1.0 shown in the panels from (d) to (f) respectively in Fig.3.6 for different temperatures one below and other above of the metal-insulator transition temperature, for fixed $U = 5.6t$ as the representative curves. In (d) $\omega\sigma(\omega)$ as a function of ω for two temperatures, one for $0.05t$ and another for $0.325t$ are plotted. For $T = 0.05t$, $\omega\sigma(\omega)$ shows non-linear behavior in the low frequency regime with ω and hence results insulating behavior. But as we heat up, at $T = 0.325t$ $\omega\sigma(\omega)$ vs ω exhibits linear dependence and hence becomes metallic. This temperature point shown here lies in the PM-M phase. In Fig.3.6 (e) for $t' = -0.9t$ $\omega\sigma(\omega)$ vs ω is plotted at two temperatures $T = 0.01t$ and $0.08t$. Both the curves show linear

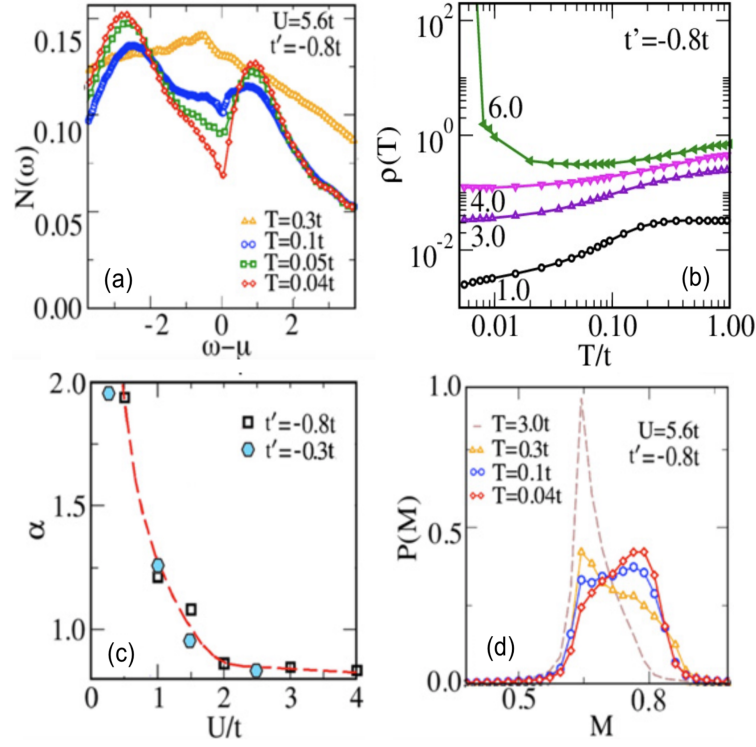


Figure 3.7: Panel (a) represents thermal evolution of the density of states (DOS) for $U = 5.6t$ at $t' = -0.8t$. The orange, blue, green and red curves represent DOS for $T = 0.3t$, $0.1t$, $0.05t$ and $0.04t$ respectively as indicated. (b) shows temperature dependent resistivity in units of $\frac{\pi e^2}{ha}$, $\rho(T)$ at $t' = -0.8t$ for different U as shown in the plot. The green, magenta, violet and black curves are for $U = 6.0t$, $4.0t$, $3.0t$ and $1.0t$ respectively. In (c), the exponent, α of resistivity, $\rho(T)$ is plotted against U for $t' = -0.8t$ and $t' = -0.3t$ represented by the open squares and solid hexagons respectively. (d) shows the distribution of local moments $P(M)$ for different temperatures for $U = 5.6t$ and $t' = -0.8t$. The solid red line with diamonds, blue line with circles, orange line with up triangles and brown dashed line are for $T = 0.04t$, $0.1t$, $0.3t$ and $3.0t$ respectively.

behavior in the small ω regime and both imply metallic phases. These points lie in the dotted paramagnetic metallic phase in the finite temperature phase diagram in the Fig.3.6 (b). For higher t'/t value -1.0 shown in Fig.3.6 (f), at the same U , the product of frequency and the optical conductivity as a function of ω exhibits non-linear behavior for $T = 0.01t$ and gives insulating phase, whereas at higher T , $0.05t$ it is linear and hence it represents metallicity. We note that these results are consistent with the usual way of using the sign of $d\rho/dT$ as an indicator of insulator to metal transition.

3.5.3 Nature of the metal at finite T

We now discuss the nature of the frustration induced metal at finite T . For this we chose $U = 5.6t$ at $t' = -0.8t$. We have already seen in Fig.3.5 (b) that at low T , s-MC shows that the DOS has a pseudo-gap. In Fig.3.7 (a) we show the DOS for the same parameter point for different temperatures. We find that the pseudo-gap (PG) feature reduces with temperature increase and is absent for $T = 0.36t$. Such PG is also seen for $U = 6.0t$ and $U = 4.0t$ as well. In Fig.3.7 (b) we show that the $\rho(T)$ in units of $\pi e^2/\hbar a$ for $t' = -0.8t$ and different values of U . We see a metallic behavior for $U < 6t$. For $U = 6t$ resistivity diverges signaling the closing of the metallic window. We fit the $\rho(T)$ to $AT^\alpha + B$ for the metallic cases and extract α . For $t'/t = -0.8$. We find $\alpha = 2$ only for small U values. From $U = 0.5t$, the exponent drops sharply and eventually saturates to a sub-linear value with U increase as shown in Fig.3.7 (c). From there α remains constant till the Mott state is reached. We show the exponent calculated at $t'/t = -0.3$ as well with hexagons to show the same evolution with U .

The reason of deviation of the exponent of resistivity and pseudo-gapped (PG) density of states (DOS) lies in the real space distribution of local moment $P(M)$ at different temperatures presented in the Fig.3.7 (d) for $U = 5.6t$ at $t' = -0.8t$. It shows a single dominant peak at very high T (as for $T = 3.0t$). At these temperatures, the effect of U is highly suppressed and the $P(M)$ peaks at values close

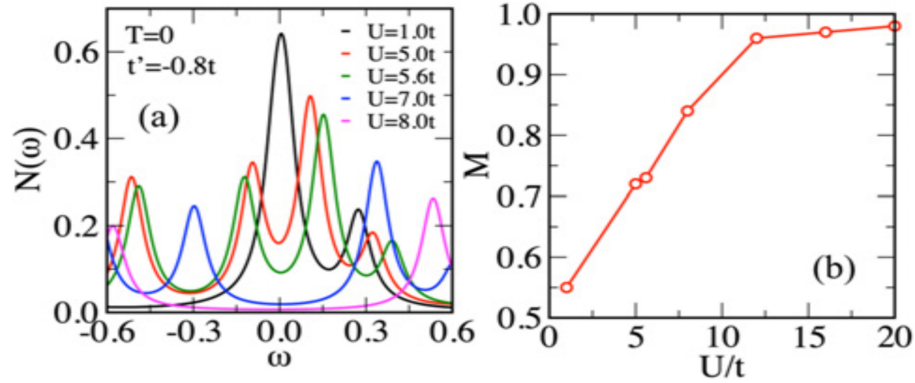


Figure 3.8: Panel (a) shows the single particle DOS found from Lanczos on a 4×6 cluster at $T = 0$ for $t' = -0.8t$ and different U values. Panel (b) shows the local moment (M) as a function of U/t for the system for the same t' value.

to 0.5. The corresponding DOS is non-PG. With the reduction in T , at $0.3t$ for example a shoulder develops at $M \sim 0.7$, signaling local moment formation. Below this temperature, the DOS develops a PG and is correlated with the formation of a broad distribution of local moments. Thus we infer the PG as a result of electron scattering from spatially inhomogeneous local moments and is also the cause of Fermi liquid (FL) to non-Fermi liquid (non-FL) crossover.

3.5.4 Pseudogapped metal at $T = 0$

So, we have already shown the existence of the finite temperature PG. We have discussed that its origin is due to the scattering of electrons from the inhomogeneous distribution of local moments in the real space. At low temperatures, the quantum fluctuation will take over the thermal fluctuations. As the s-M technique can not capture quantum fluctuation in this regime, it produces static solution with uniform moments over the system. So, it can not exhibit PG state. Hence, we show Lanczos based ED density of states for different U values and local moment length as a function of U at $T = 0$ in panels (a) and (b) of Fig.3.8 respectively. The data are shown for $t' = -0.8t$ on a small 4×6 cluster. In panel (a), it can be seen that at small U , the DOS is non-PG (normal) but a pseudo-gap feature develops as we increase U/t values from 5 – 7. In this interval of U , the moment length increase

from 0.5 (uncorrelated value) to 0.8. The increase of the local moment size as a function of U is shown in Fig.3.8 (b). This indicates the correlation between the moment size and the PG DOS at $T = 0$. The PG becomes robust and then goes to Mott gap when the moment size exceeds 0.8. This $T = 0$ PG induced by quantum fluctuation meets the PG driven by the thermal fluctuation at finite T in s-MC calculation as discussed before.

3.6 Conclusions

Here, we have studied the effect of correlation and frustration in the half-filled Hubbard model using the semi-classical Monte-Carlo approach on a square lattice at finite temperature. We have investigated the temperature evolution of magnetic phases, metal-insulator transitions. We have also calculated the thermal scale (T^*) of the crossover of the PG regime to normal metal. The results found from the finite temperature s-MC and $T = 0$ Lanczos are consistent. They exhibit that the transition of the small U Fermi liquid to large U Mott in the large frustration t' regime is not a direct transition, but through an intermediate PG metallic state. Although we have concentrated at the frustration value $t' = -0.8t$, we have found that this holds for the t' regime from $-0.2t$ to $-1.0t$.

As we have pointed out in the model and method chapter (chapter 2) that in s-MC technique our goal is to generate thermally equilibrium Aux. F configurations by means of classical Monte-Carlo at a given temperature. The acceptances or rejections of a proposed update of Aux. F depends on both the classical Aux. F background and the quantum mechanical fermion part. We have noticed that away from the metal-insulator phase boundary, the uniformly distributed Aux. F thermalize the system and show Fermi liquid metallic behavior in the small U regime or spatial uniform distribution of local moment gives thermal equilibrium state in the large U region which leads to Mott phase. But at finite T and close to the metal-insulator boundary, thermal fluctuation helps the Aux. F to access the free energy minima for both the Fermi liquid and Mott insulator. This leads to the

inhomogeneous spatial distribution of local moments and electrons scatter from them give rise to PG state at finite temperature. The Aux. F get decoupled from the fermions at very high temperature ($T > T^*$) that was discussed in our previous work on the unrestricted Hubbard model [89] and as a result, the PG state goes away. As a complementary to the s-MC study, $T = 0$ Lanczos calculation on a 4×6 cluster shows that there is a frustration driven PG phase arises between the Fermi liquid and Mott insulator. We finally note that our finite T deviation from Fermi liquid expectations is qualitatively similar to the renormalized RPA results discussed in chapter 1, and importantly shows that is such behavior survives in the thermal fluctuation dominated regime.

Comparison with quantum approaches: In the chapter 2, in the sub-section “Benchmarks of s-MC” we have discussed that in previous study for the unfrustrated case, Phys. Rev. B **90**, 205133 (2014), the magnetic phase boundary found from s-MC calculation show good qualitative agreement with DQMC. Quantitatively, s-MC underestimates the T_N due to lack of quantum coherence when compared with DQMC, as seen in Fig.12 (a) and (c) in [Phys. Rev. B **90**, 205133 (2014)]. For the case with frustration, as shown in Fig.3.1 of the present thesis, the $T \rightarrow 0$ limit of s-MC, again has good qualitative agreement with Gutzwiller variational approach study [Tocchio *et al.* Phys. Rev. B **78**, 041101 (2008)] with regards to the various phase boundaries. The quantitative agreement is however found to be better for smaller frustration cases. In particular the critical U for PM-M to AF1-I and AF2-I are again underestimated in s-MC. Similarly the large frustration driven CPM phase occurs for larger critical U in s-MC than for the quantum calculation. Similarly, the T_N in the frustrated case is systematically underestimated in s-MC, as seen by comparing Fig.1.6 and Fig.3.2 in the thesis. Thus as a general conclusion, s-MC quantitatively underestimates the finite T phase boundaries due to lack of quantum coherence. At $T = 0$, the same lack of quantum fluctuations favours magnetic ordered phases over a paramagnet at smaller U values, particularly at larger frustrations, where such quantum fluctuations are significantly greater.

Chapter 4

Temperature driven half metal from a Mott Insulator

4.1 Introduction

The subject of this chapter is to study the impact of staggered onsite potential (Δ) on the half filled Hubbard model in two dimensions in addition to the effect of next nearest neighbor (nnn) hopping (t') discussed in the previous chapter. The motivation for this work is to investigate the physics of half metallicity (conductors with carriers of only one spin channel) at finite temperatures. As seen in the previous chapter, the half filled Hubbard model has a nesting driven Slater insulating ground state at $T = 0$ (with nearest neighbor hopping) at small correlation strength. At large interaction strength U we have a Mott insulating ground state. We have also shown that nnn hopping lifts the nesting instability and destabilizes the Slater insulator. In the large interaction Mott limit, nnn hopping acts as a frustrating agency when examined within the Heisenberg limit and causes a G-type to A-type change in the magnetic order. Thus, nnn hopping is one way for metallizing the half filled Hubbard model. In earlier work [48] on the half filled Hubbard model with staggered onsite potential, also known as the Ionic Hubbard model (IHM), a curious correlation driven metallization was reported within a paramagnetic DMFT

calculation. The intuitive picture for this phenomena is as follows. In the non interacting IHM, the presence of onsite energies opens up a band gap, with the sublattice with lower onsite energy being doubly occupied. In the other limit of only interaction, and nearest neighbor kinetic energy, we have the original Mott state with singly occupied sites. In the third limit of both agencies are present but no kinetic energy, it is easy to see that doubly occupied sites with $-\Delta$ potential are preferred for $U < 2\Delta$ and for $U > 2\Delta$, we have singly occupied sites. The single particle charge gap is $U - 2\Delta$. Clearly if $U = 2\Delta$, the charge gap vanishes. Thus a metal may be expected when hopping is switched on. However, on allowing magnetic order to set in the metallic state was shown to be preempted by an antiferromagnetic insulating ground state[50].

Very recently[47], it was shown that inclusion of nnn hopping that weakens insulating tendency and frustrates G-type magnetic order as discussed above, can allow a metallic state even in presence of magnetic order. More interestingly as discussed in the introduction chapter, the state can be a half metal or paramagnetic metal depending on the parameters at $T = 0$. In this chapter we investigate the finite temperature evolution of the IHM. The study of half metals are of great relevance for spintronic device applications which are based on electron spin based electronics as discussed in chapter 1.

We will show that our semiclassical method can capture the DMFT results[47] at low temperatures qualitatively. We will present the transport response of the model at finite temperature, in the band insulator, Mott insulator and half metallic regime. We will show that a novel half metal can emerge out of a Mott insulating state up on heating in the vicinity of the Mott-metal boundary. We will characterize this ‘finite-T’ half metal by conduction electron polarization, sub-lattice magnetization and local moment systematics to provide a clear microscopic phenomenology of the novel half metal. We will show that the temperature window of half metallicity can be tuned by varying the model parameters. We will conclude with a brief discussion of materials where this phase can be realized and plausibility of constructing the same in cold atomic systems.

4.2 $t - t'$ Ionic Hubbard model

The IHM on a square lattice is defined as follows:

$$\begin{aligned}
 H = & -t \sum_{\langle i,j \rangle, \sigma} (c_{i\sigma}^\dagger c_{j\sigma} + h.c) - t' \sum_{\langle\langle i,j \rangle\rangle, \sigma} (c_{i\sigma}^\dagger c_{j\sigma} + h.c) \\
 & + \Delta \sum_{i \in A} n_i - \Delta \sum_{i \in B} n_i + U \sum_i n_{i\uparrow} n_{i\downarrow} - \mu \sum_i n_i
 \end{aligned} \tag{4.1}$$

where, $c_{i\sigma}^\dagger$ ($c_{i\sigma}$) are electron creation (annihilation) operators at the site i with spin σ . t and t' are respectively the nearest and nnn hopping amplitudes. We choose $t'/t < 0$ in our study. $n_{i\sigma} = c_{i\sigma}^\dagger c_{i\sigma}$ is the number operator for spin σ at a site i and n_i is the spin summed local number operator. Δ is the magnitude of ‘ionic’ potential and takes positive (negative) values on the A (B) sub-lattice. U is the local Hubbard repulsion. μ denotes the chemical potential, and is adjusted to maintain half filling. All indicators used in this chapter are defined in Appendix E.

4.3 Transport response

Here we present the resistivity vs temperature behavior at fixed $t'/t = -0.2$ and $\Delta = 1.0t$ but by varying U . We will later discuss the effect of varying t' and Δ .

4.3.1 Band insulator

As we discussed already that in the presence of Δ , the model gives band insulating phase in the small interaction regime at low T . The conductivity, $\sigma(\omega)$ is calculated using Kubo-Greenwood formalism along x-direction. The spin resolved conductivity in the small frequency regime, integrated over small window is used to evaluate spin resolved resistivity, $\rho_\sigma(T)$ at different temperatures T which is plotted at fixed U , $2.6t$ for $\Delta = 1.0t$ and frustration caused by the second nearest neighbor hopping $t' = -0.2t$ in the Fig 4.1 (a). The red solid line with square is $\rho_\downarrow(T)$ for the down spin channel. The resistivity for the up spin species, $\rho_\uparrow(T)$ is represented by the blue

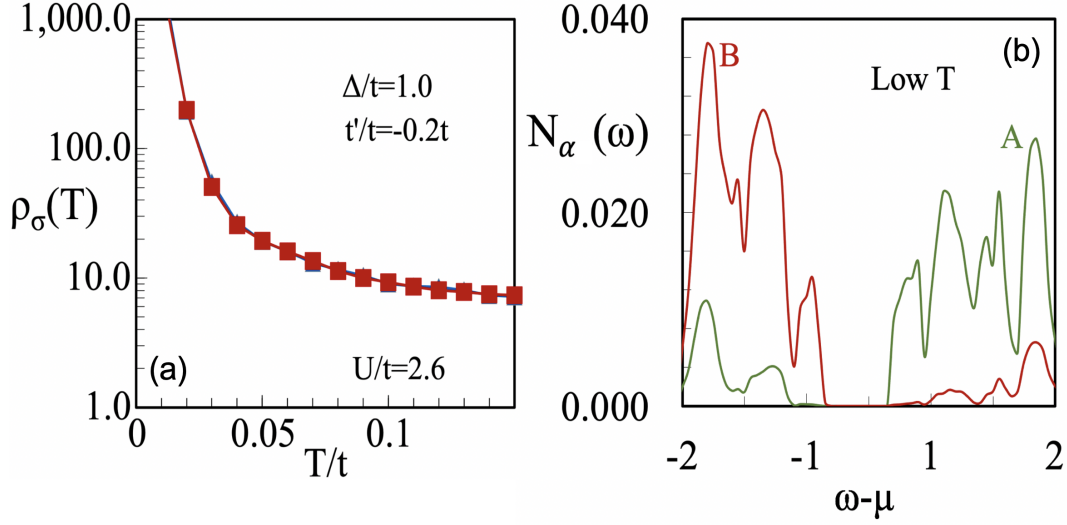


Figure 4.1: The spin resolved resistivities are presented in panel (a) for $t' = -0.2t$ and $\Delta = 1.0t$ at fixed interaction $U = 2.6t$ in the panel. The blue line with up-triangles is the resistivity for up spin and red square with solid line depicts the down spin channel of the resistivity. The curves are on top of each other. Panel (b) shows the sublattice resolved density of states (DOS) for the same parameter values at low T . The green line and red lines are DOS for sublattice A and B as shown respectively.

line with up-triangles lie below the curve of $\rho_{\downarrow}(T)$. Both the curves show negative slope ($d\rho_{\sigma}(T)/dT < 0$) with the temperature axis at all T . Therefore, the system exhibits weakly correlated band insulating property as Δ dominates over U/t in this parameter space. The band insulating phase exist in the window $0 \leq U/t \leq 2.8$ at the chosen values of Δ and t' . The sublattice-resolved density of states (DOS) shown in (b) shows a gapped spectra at low T . The B sub-lattice is filled, while the sub-lattice A is primarily empty, apart from small admixtures due to kinetic energy.

4.3.2 Mott insulator

In the regime when U dominates over Δ , Mott insulating phase appears in the system. For $\Delta = 1.0t$ and $t' = -0.2t$, the Mott phase starts beyond $U = 4.75t$. A representative spin resolved transport characteristics at finite T are shown in the Fig 4.2 (a) for $U = 5.5t$ at the above mentioned ionic potential and frustration values. The red solid line with squares and the blue solid line with up triangles

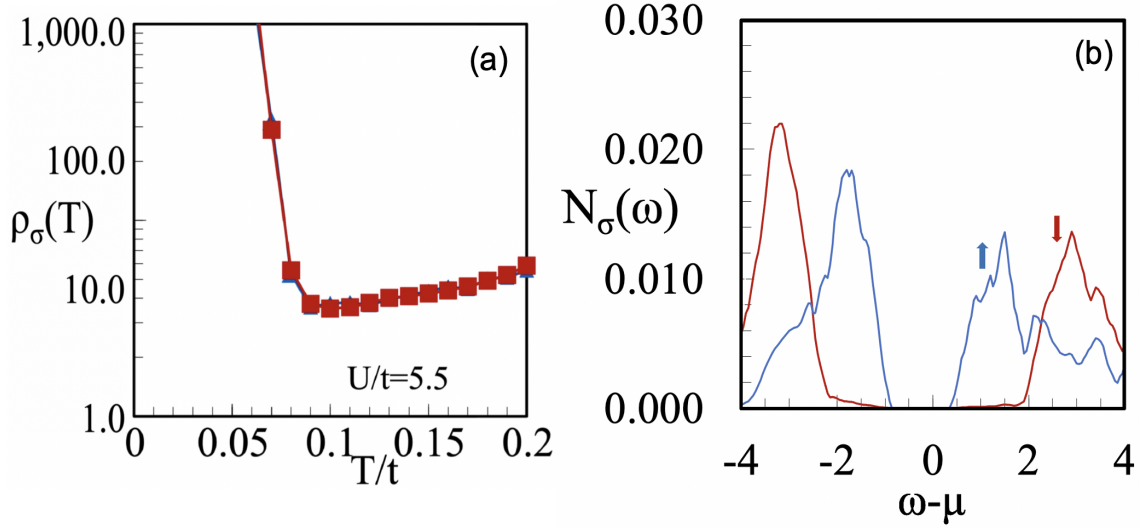


Figure 4.2: In panel (a) spin resolved resistivity in the Mott phase at $U = 5.5t$ for fixed frustration and ionic potential $t' = -0.2t$ and $\Delta = 1.0t$ respectively. The resistivity for up spin and down spin are given by solid blue line with up triangle and solid line with square respectively. The low T spin resolved DOS is shown in panel (b) for the same U , t' , and Δ with blue line indicating the up spin channel and red one is for down spin channel as indicated by the arrows with same colours.

are the spin resolved resistivity for down and up spin respectively plotted against temperature. The up and down channel resistivities ($\rho_\uparrow(T)$ and $\rho_\downarrow(T)$) are on top of each other. We find $d\rho_\sigma(T)/dT$ changes sign from negative to positive at $T \sim 0.1t$ for both spin channels. This insulator to metal crossover scale is denoted by T^* and is the analog of the same scale in the Hubbard model discussed in the previous chapter. It is important to point out here that below T^* , preformed local moments appear without any magnetic order (which sets in below T_N). The spin-resolved DOS in (b) shows a gapped ground state. However, we clearly see that the charge gap for the two spin species are not equal. This observation will play a vital role in stabilizing the novel ‘finite- T ’ half metal to be discussed later.

4.3.3 Low T half-metal

At low temperature when the effect of ionic potential Δ is screened exactly by the Hubbard interaction U , the system has metallic instability which is enhanced and made stable by the frustration caused by the second nearest neighbor hopping t' .

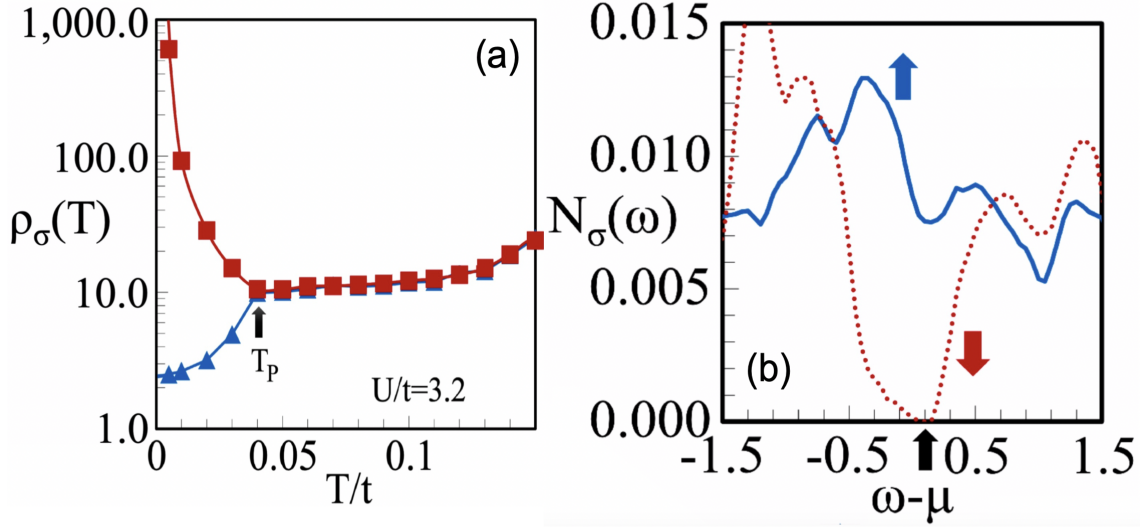


Figure 4.3: In this figure, panel (a) shows the spin resolved resistivities as a function of temperature at $U = 3.2t$ for frustration $t' = -0.2t$ and ionic potential $\Delta = 1.0t$. Here, the blue up triangles with solid line resistivity for the up spin and the red one with solid squares is that for the down spin channel. Slope of the curve for the down spin is negative and hence refers to insulating behavior whereas the up channel because of negative slope, gives metallicity. The point where both curves merge, polarization goes to zero (explained in the main text) the temperature scale is named as T_p . The panel (b) shows the low T spin resolved DOS at the same interaction value U and t' and Δ . The red dotted line is for the down spin channel and shows insulating behaviour whereas the blue solid line represents the up spin channel which shows metallic behaviour.

The metallic phase arises in the window of interaction $2.8t \leq U \leq 4.57t$. A typical thermal evolution of spin resolved resistivity data is presented in Fig.4.3 (a) at $U = 3.2t$ at fixed ionic potential, $\Delta = 1.0t$ and frustration value $-0.2t$. Red solid line with square and blue solid line with up triangle show the down and up resistivity respectively. The diverging characteristic at low T of the resistivity of down spin channel, $\rho_{\downarrow}(T)$ having negative slope ($d\rho_{\downarrow}/dT < 0$), decreases as temperature increases. The curve changes slope at the temperature indicated by the arrow and then remains positive ($d\rho_{\downarrow}/dT > 0$) at higher temperatures. In contrast, the resistivity for the up spin channel has positive slope, $d\rho_{\uparrow}/dT > 0$ for all temperatures. We refer to the lowest temperature where the down and up channel resistivity meet as the polarization temperature T_p , indicated by the arrow. As will be shown below for $T \leq T_p$, the system shows spin polarized conduction, with the spin polarization

being 100% at low T and decreasing gradually with temperature increase. At and above T_P , the spin polarization goes to zero and both spin species take part in the conduction process. In this case T_P is $0.04t$.

The spin-resolved DOS for the same parameters point is shown in Fig.4.3 (b) at low T . The blue solid line and red dotted lines are for up and down spin respectively as designated by the solid up and down arrows with same colors used in the curves. It is clear from the figure that the up channel has finite weight at the chemical potential shown by the black thick arrow and makes the system metallic for this particular spin. But the DOS for down spin is gapped and makes the system insulating. Therefore as at low T only one spin channel (up here) participate in the conduction process, the system shows half-metallicity which also found from the transport calculation discussed above. Increase in temperature causes a gradual filling up of the charge gap for the down spin channel which eventually kills off the polarization beyond T_P .

4.3.4 Finite-temperature half metal

In Fig.4.4 (a) we show the resistivity vs temperature for the two spin channels for a $U(= 4.8t)$ value close to the low temperature Mott-metal boundary of $U = 4.75t$. As expected at low T the resistivity of the two spin channels diverge. However in remarkable contrast to the previous three cases, at a low temperature scale (defined as T_S), $d\rho_{\uparrow}/dT$ for the up spin channel switches sign, while the down spin channel continues to evolve as an insulator with temperature. The resistivity for the two spin channels eventually merge at T_P . The inset shows the total resistivity, clearly showing the transition to a metal at the temperature scale T_S . This gives a strong indication of an insulator to a spin polarized metal to a paramagnetic metal evolution with temperature. The low temperature spin-resolved DOS Fig.4.4 (b), shows an unequal charge gap for the two spin channels, much like the DOS at large U Mott insulator. To understand the thermal evolution, in Fig.4.5 (a) we show the spectral weight at the chemical potential ($N(0)$) as a function of temperature for the two

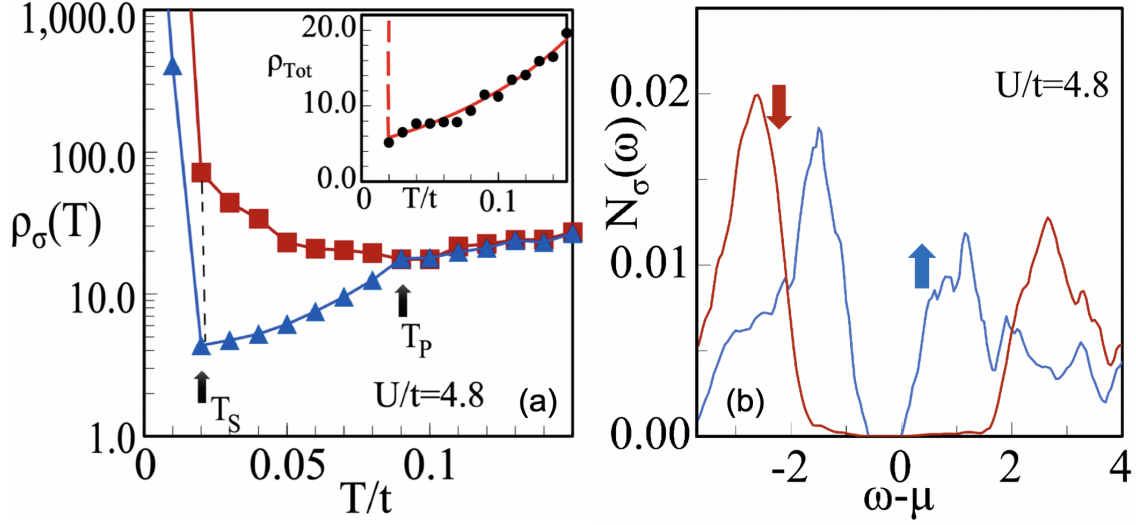


Figure 4.4: The panel (a) shows spin resolved resistivity ($\rho_\sigma(T)$, $\sigma = \uparrow\downarrow$) vs temperature (T) at $U = 4.8t$ for $\Delta = 1.0t$ and $t' = -0.2t$. The red line with solid squares and blue line with solid up-triangle represent T dependent resistivity for down and up spin respectively. The black arrows defining T_S and T_P are corresponds to on set metallic phase and polarization temperature. This is discussed in details in the main text. In the inset the total resistivity is plotted against T at the same parameters value. In panel (b) spin resolved DOS is plotted. The blue and red solid line represent the DOS for up and down spin channel respectively for $\Delta = 1.0t$ and $t' = -0.2t$ at $U = 4.8t$. The arrows with respective colours show the spin channels in panel.

spin channels. We see that the temperature induced gap filling is lot more rapid for the up spin channel (the one with the smaller charge gap at low T). The two spectral weights finally become equal at T_P . The location of T_S is also marked in the figure. Since, as discussed in the previous chapter thermally induced gap filling does not guarantee a metal, we rely on the resistivity (extracted from the conductivity data as explained above) to decide on metallic and insulating states. For this reason we do not define the polarization using the usual definition $(N_\uparrow(0) - N_\downarrow(0))/(N_\uparrow(0) + N_\downarrow(0))$. Instead, we compute conduction electron polarization or transport polarization $P(T) \equiv (J_\uparrow^x(0) - J_\downarrow^x(0))/(J_\uparrow^x(0) + J_\downarrow^x(0))$. The current is easily read off from the low frequency conductivity using the relation $J^x = \sigma^{xx} E^x$. $P(T)$ computed in this manner is shown in Fig.4.5 (b). The data is shown for the low temperature half metal at $U = 3.2t$ in blue triangles and for two other cases $U = 4.8t$ and $4.9t$. These two later U values are close to the low temperature Mott-

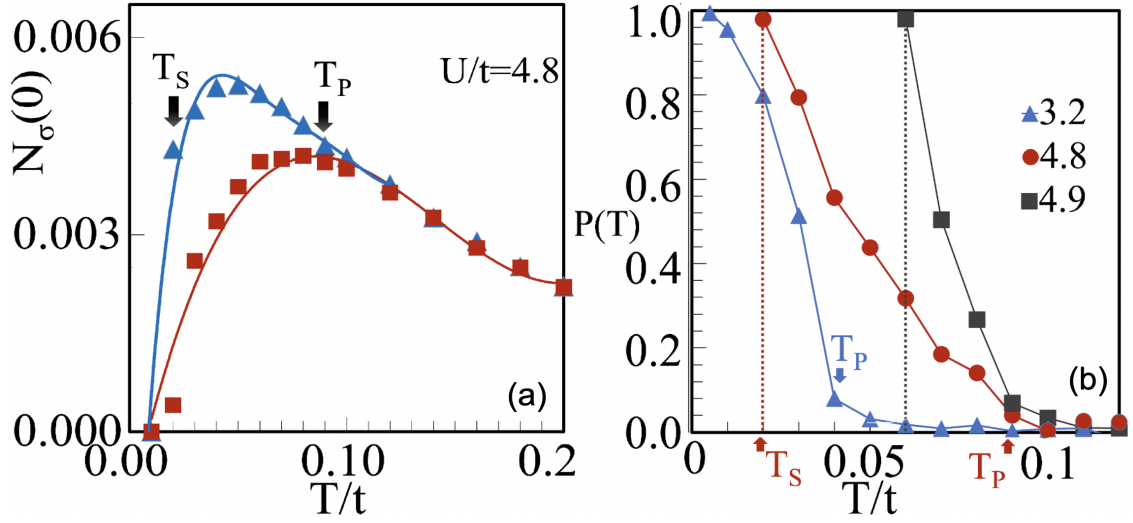


Figure 4.5: The panel (a) shows the spectral weight of up and down spin channels at the chemical potential as a function of temperature. The red solid line with squares and blue solid line with up-triangles are the temperature evolution the zero frequency weight of the down and up spin channels respectively. The black thick arrows specifies the T_s and T_p as in the resistivity calculations. In panel (b), the polarization of conduction electrons, ($P(T)$) vs temperature (T) is plotted for three different interaction values $U = 3.2t$, $4.8t$ and $4.9t$ and corresponding curves are shown by solid blue line with uptriangles, solid red line with circles and solid black line with squares respectively. The arrows are indicating T_s and T_p with respective colours for these U values.

metal boundary and are representative of the ‘finite-T’ half metal. The location of T_P for the low- T half metal ($U = 3.2t$) and that of T_S and T_P for the ‘finite -T’ half metal ($U = 4.8t$) are indicated in the figure. The low- T half metal has 100% spin polarization or $P(T) = 1$ at low temperature, while in contrast the spin polarization for $U = 4.8t$ is zero up to T_S . The onset of ‘finite-T’ half metallicity is triggered at T_S , where $P(T)$ abruptly jumps to 1. The subsequent thermal evolution sees a gradual decrease in $P(T)$ up to T_P . The polarization is zero for $T > T_P$. We see that for a small increase in U from $4.8t$ to $4.9t$, T_S is pushed up from $0.02t$ to $0.06t$, showing that the onset of half metallicity can be tuned by changing U .

4.4 Magnetism & metallicity

The temperature dependent sublattice magnetization is $\langle S_\alpha^z(T) \rangle$, where α being the sub-lattices A and B i.e $\alpha \in \{A, B\}$. For a particular temperature it is defined as $\langle S_z^\alpha \rangle = (\langle n_\alpha^\uparrow \rangle - \langle n_\alpha^\downarrow \rangle)/2$. Here, the angular bracket stands for both quantum and thermal averages. In Fig. 4.6 (a) we show the sub-lattice magnetization for $U = 3.2t$ and $U = 4.8t$, as a function of temperature. For $U = 3.2t$ we find that the half metal has staggered magnetic order with $|S_z^A| = |S_z^B|$ at all temperatures below T_P . This implies an antiferromagnetic half metal (which agrees qualitatively with the DMFT results[47]). For $U = 4.8t$, however the evolution is rather non-trivial. At low T , in the Mott insulator with unequal charge gap for the two spin channels, $|S_z^A| = |S_z^B|$ and has a staggered orientation. This shows antiferromagnetic order in the Mott state, again in agreement with DMFT. However at T_S , there is an abrupt jump in the sub-lattice magnetizations leading to a magnetic state with $|S_A^z| > |S_B^z|$. It can be easily seen that in this state the system is forced to generate a net spin polarization, due to the relation $\delta n/2 = S_z^A + S_z^B$. The δn is shown in Fig. 4.6 (b) for $U = 4.8t, 4.9t$ and $4.95t$.

Due to the unequal sub-lattice magnetizations we refer to this phase as a ferromagnetic ‘finite-T’ half metal. Finally since the ground state is a Mott insulator, it is relevant to ask if local moments survive in the the metallic state. In panel (c) we show the system averaged local moment distribution in real space for $U = 4.8t$ as a function of temperature. The sublattice local moment difference is shown in (d) as a function of temperature. Analogous to the definition in the previous chapter, we define the sub-lattice local moment M_α , as $M_\alpha = \langle n_\alpha \rangle - 2\langle n_{\alpha\uparrow}n_{\alpha\downarrow} \rangle$ with $\langle n_\alpha \rangle = \langle n_{\alpha\uparrow} + n_{\alpha\downarrow} \rangle$. Finally system averaged local moment shown in (c) is averaged over the two sub-lattice moments and δM shown in (d) is $M_A - M_B$.

To comprehend the above temperature-driven behavior, consider that finite Δ imposes a double occupancy penalty of $U + 2\Delta$ ($U - 2\Delta$) on the A (B) sub-lattice in the zero hopping limit. For finite hopping, this differential penalty exists, but with a renormalized value. Fig. 4.7 (a) depicts the typical temperature evolution

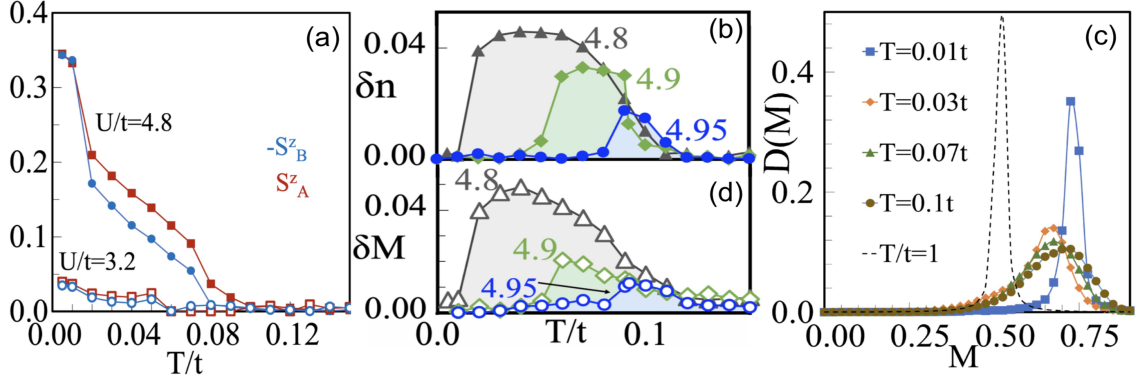


Figure 4.6: In this figure, the panel (a) shows the sub-lattice magnetization as a function of temperature for $U = 3.2t$ and $4.8t$ as indicated at fixed $t'(-0.2t)$ and $\Delta(1.0t)$. The red line with open squares and blue line with open circles are for A and B sub-lattices respectively for $U = 3.2t$. The curves with same colours but with solid symbols show the results for $U = 4.8t$. In panel (b), up and down spin density difference i.e. $\delta n = n_\uparrow - n_\downarrow$ is plotted as a function of T at $U = 4.8t, 4.9t, 4.95t$ indicated by solid gray line with uptriangles, green line with diamonds and blue line with circles respectively for $t' = -0.2t$ and $\Delta = 1.0t$. In panel (c), the local moment distributions in real space are plotted for different temperatures at $U = 4.8t$ for $\Delta = 1.0t$ and $t' = -0.2t$. The blue, orange, green, brown and black with solid and dashed lines are shown here for temperatures, $T = 0.01t, 0.03t, 0.07t, 0.1t$ and $1t$ respectively. Panel (d) shows the sub-lattice local moment difference, $\delta M = M_A - M_B$ plotted against temperature for the same U values as in panel (b) represented by solid gray line with open uptriangles, green line with open diamonds and blue line with open circles respectively for $t' = -0.2t$ and $\Delta = 1.0t$.

of the sublattice double occupations $\langle n_{\alpha\uparrow}n_{\alpha\downarrow} \rangle$ with $\alpha \in (A, B)$ for the ‘finite-T’ half metal. It clearly illustrates that, at all temperatures, $\langle n_{B\uparrow}n_{B\downarrow} \rangle > \langle n_{A\uparrow}n_{A\downarrow} \rangle$. Fig. 4.6 (a) shows that the higher cost of double occupation at A initially causes a finite magnetization S_z^A at $T_P (= 0.09t)$, whereas S_z^B becomes non-zero only at a lower temperature. It also keeps $|S_z^B| < |S_z^A|$ and, as a result, a finite δn following $S_z^A + S_z^B = \delta n/2$ for $T_S < T < T_P$. The unequal sublattice local moments in Fig. 4.6 (d) in the same temperature range has the same cause.

At low temperatures, however, the large build-up of doublons ($\langle n_{B\uparrow}n_{B\downarrow} \rangle$) becomes unsustainable energetically. Below T_S , a first-order transition reduces the difference in sublattice double occupations, making the sublattice magnetizations equal, quenching δn and limiting the half-metallic state to a finite temperature. In the temperature window of the finite temperature half metal, the conduction elec-

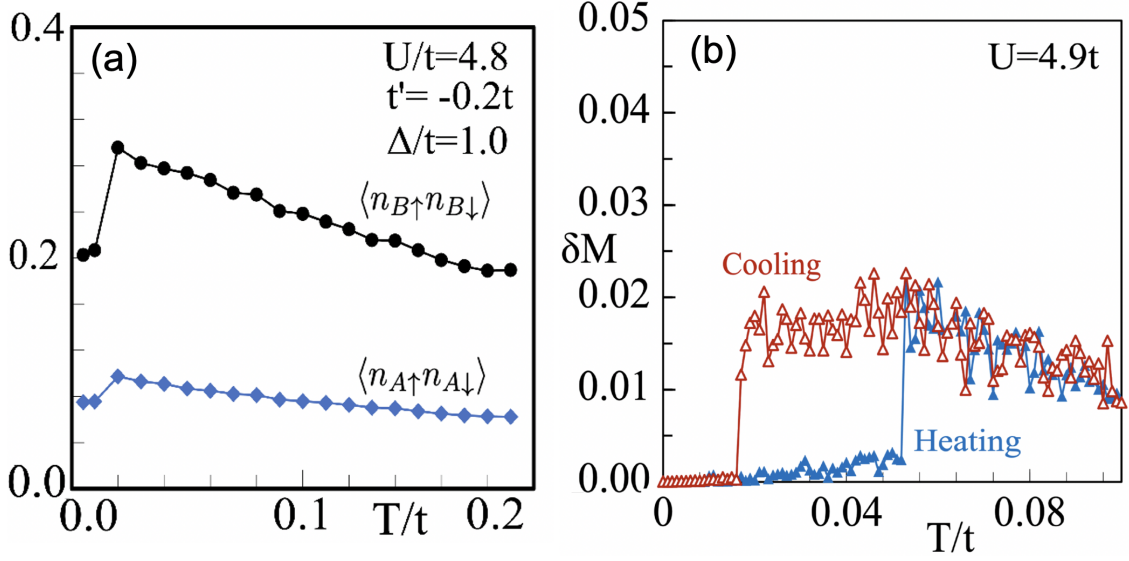


Figure 4.7: The sublattice resolved double occupation is plotted as a function of temperature in panel (a) for $t' = -0.2t$ and $\Delta = 1.0t$ at $U = 4.8t$. The blue and black lines are for A and B sub-lattices respectively. In the panel (b), the differences of local moment for sublattice A and B, obtained from cooling and heating procedure in s-MC method are plotted against temperature for $U = 4.9t$ at the same t' and Δ as in panel (a). The hysteresis in δM hints towards the first order transition at the onset of HM_2 phase.

tron spin direction is identical to the net spin polarization δn , ‘up’ in this case, as seen in Fig. 4.4 (a). It also translates into $N_{\uparrow}(0) > N_{\downarrow}(0)$ for $T_S < T < T_P$, and can be viewed as thermal fluctuation-driven spin-asymmetric charge gap filling, as seen in Fig. 4.5 (a). The local moment distribution in Fig. 4.6 (c) becomes broad at intermediate temperatures exactly as in the previous chapter and acts as the source of scattering leading to the filling-up of the Mott gap. In Fig. 4.7 (b) we show data from heating and cooling cycles of δM which shows a large hysteresis window lending support to the first order transition from an antiferromagnetic insulator to a ferrimagnetic half metal. Similar hysteresis is seen on δn and S_{α}^z as well.

4.5 Phase diagrams

We now construct a $U - T$ phase diagram to put the various properties discussed so far for fixed $\Delta (= 1.0t)$ and $t'/t = -0.2$. We will discuss the effects of these

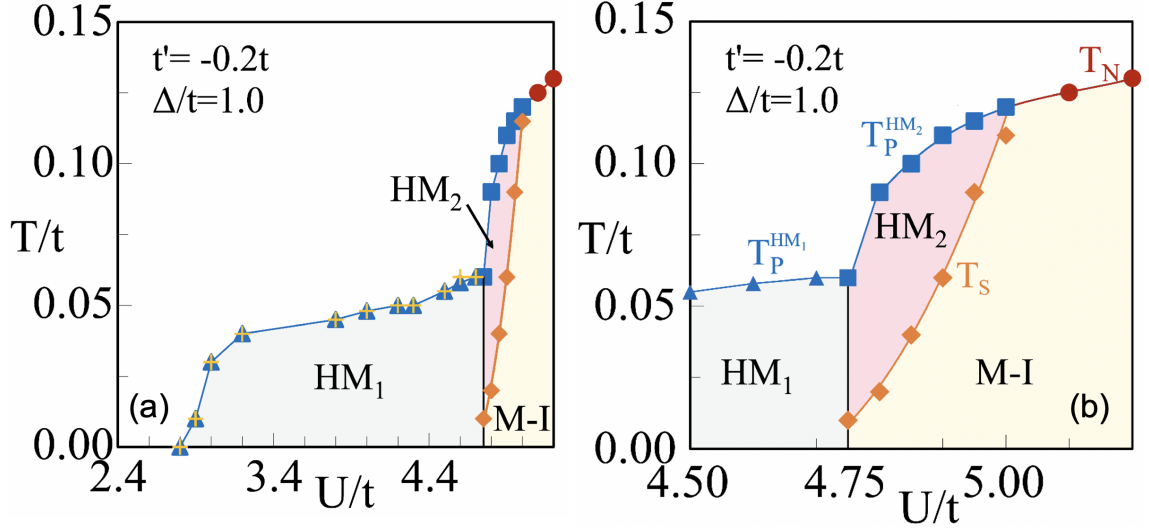


Figure 4.8: Panel (a) shows the full $U - T$ phase diagram for fixed $t' (= -0.2t)$ and $\Delta (= 1.0t)$. In panel (b) magnified version of the full phase diagram is shown focusing into the HM_2 phase. In both the figures, same colours scheme are used for indicating different phases. The gray and yellow regimes show the HM_1 and $M - I$ phases respectively. The red region is the finite T half-metallic phase, HM_2 . The details are discussed in the text.

parameters later. The full $U - T$ phase diagram is shown in Fig. 4.8 (a). The $U - T$ phase diagram shown in Fig. 4.8 (b) is the same figure, but focusses on the ‘finite- T ’ half metal. For brevity we will refer to the low- T half metal as HM_1 and the ‘finite- T ’ half metal as HM_2 while discussing the various phase diagrams.

In (a) we first see that for $T/t \leq 0.02$, $U (= 4.75t)$ separates HM_1 and Mott insulating (M-I) phases. We also see that HM_1 starts at $U = 2.8t$ and the T_P increases with U , reaching a maximum of $(0.055t)$ close to U_M where the triangles denote T_P while the plusses denote the T_N obtained from the staggered magnetization analysis, such as shown in Fig. 4.6 (a). Thus we conclude that HM_1 has an antiferromagnetic background and the magnetic transition temperature T_N , coincides with T_P . We discuss the rest of the phases by referring to panel (b). Here we see that the HM_2 phase emerges from the M-I in the range $4.75 < U < 5t$ and above a U dependent T_S , indicated by diamonds. The ferrimagnetic order in HM_2 is destabilized at the corresponding T_P values (squares), as seen for example, for $U = 4.8t$ in Fig. 4.6 (a). Circles represent the antiferromagnetic transition temperature for the M-I phase

beyond the HM_2 window or $U > 5t$.

For HM_2 , we can also see that T_S increases rapidly with U . The necessity for more thermal energy to fill the Mott gap at increasing U values explains this trend. As U increases, however, we travel deeper into the Mott state, suppressing the influence of Δ . As seen in Fig.4.6 (b) and (d), the more dominant role of U manifests itself in a systematic decline in the magnitudes of δn and δM . This can be concluded by comparing these quantities for the three U values shown. While the window of finite δM and δn moves to higher temperatures as U increases, their magnitudes are systematically reduced. As the sub-lattice moment magnitudes approach each other with increasing U , T_P and T_S merge into a single transition temperature T_N , of the (M-I) phase beyond $U = 5t$. As a marker of tunability of T_S , the temperature where the spin polarized conduction is 100%, we find that T_S increases by 350% over the window in U for which HM_2 is stable.

We can see in (a) that the window for HM_2 is quite narrow. As a result, we must determine whether this phase is the result of a numerical accident of fine tuning. For this reason, as well as to demonstrate a broad domain of stability for HM_2 , we will now discuss the effect of t' and Δ .

As mentioned at the start of the chapter, t' plays the role of an agency for frustration to G-type magnetic order and promoted metallicity. In our numerical calculations, we find that neither half metals occur for $|t'/t| < 0.05$. In Fig. 4.9 (a) we show the variation of T_S and T_P for a fixed Δ and U as indicated in the figure.

As seen in Fig. 4.9 (a), increasing the magnitude of t'/t above 0.05 systematically pushes the critical U for Mott transition to larger values to overcome frustration effects. Consequently T_S increases as the Mott state is shifted to higher U .

However, once the Mott state is pushed to large enough U with increasing $|t'/t|$, the reduced impact of Δ becomes inadequate to support HM_2 . This manifests as a symmetric temperature-driven gap-filling for both spin channels. For $\Delta/t = 1$, we find that HM_2 is no longer realized for $|t'/t| \geq 0.3$. Finally in panel (b), we show the U vs Δ phase diagram at low temperature, for $t' = -0.2t$. The solid line demarcates U_M , with the Mott insulating (M-I) phase lying above it. For simplicity, here, we

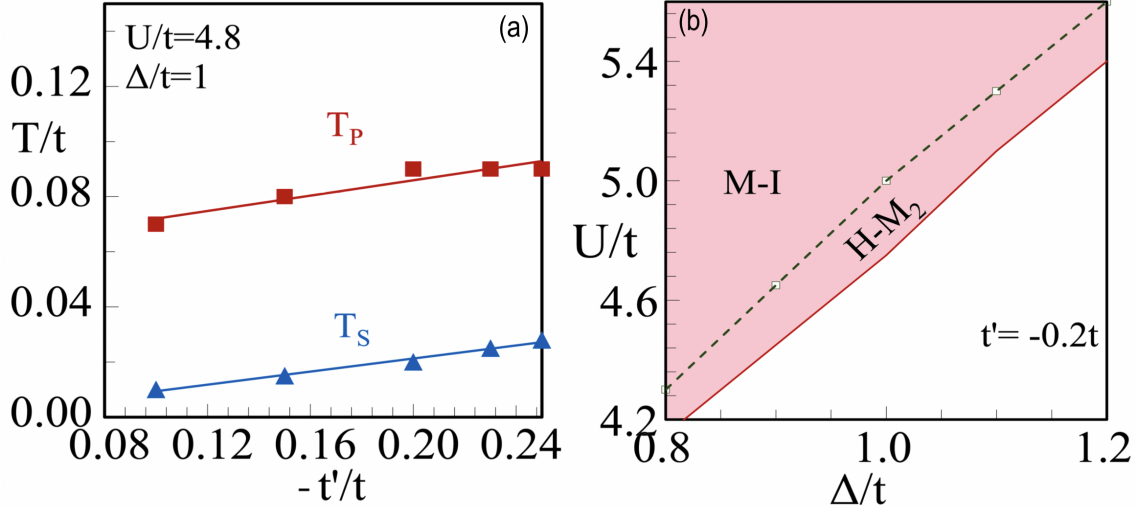


Figure 4.9: In this figure, panel (a) shows the tunneblity of HM_2 phase as a function of t'/t for fixed $U = 4.8t$ and $\Delta = 1.0t$. The solid blue line with uptriangles is the thermal scale T_s for onset of HM_2 and solid red line with squares denotes the polarization temperature T_p . In panel (b), the $\Delta - U$ phase diagram is shown at $t' = -0.2t$. The brown region is the $M - I$ phase and the window in between the black dashed line and the solid line is the HM_2 phase emerges up on heating the $M - I$ phase close to the Mott-metal transition. For simplicity the band and HM_1 phases are not shown here.

do not show HM_1 . The region between the dashed and the solid lines, following $\Delta/U \sim 0.3$, shows the regime of the Mott state, which at finite temperature supports HM_2 . These conclusions also hold for $t'/t \sim -0.1$ to -0.3 . From which we infer that HM_2 can be stabilized for Mott insulators with $\Delta/U \sim 0.2$ to 0.3 , over a large window of U and Δ .

4.6 Candidates for experimental realization

a. Correlated oxides: From the above discussion we gather the main features that can help identify possible ways to realize the novel ‘finite-T’ half metal. Firstly the ration of Δ to U has to be about 0.3. Secondly, a non zero next nearest neighbor hopping is essential to the stability of the half metallic phases. Keeping these facts in mind we consider epitaxial thin films of cubic double perovskites, X_2ABO_6 with A and B represent two species of transition metal (TM) atoms. X can be chosen

to be rare-earth, alkaline-earth, or alkali elements to control the electron filling as discussed below. We believe that the natural choice for the TM atoms should be made from the $4d$ elements. This prevents high U and strong Hund's coupling effects, unusual in $3d$ TM elements. In addition, not considering $5d$ TM elements avoids strong spin-orbit coupling.

In the $4d$ TM series, {Zr, Nb, Mo, Tc, Ru and Rh} starting with Zr, difference in the charge transfer energy (Δ) between successive elements range between 0.2eV to 1.0eV [105]. The onsite energies from the density functional calculations from [106] is reproduced in the table below, in the second row. Following the same reference, we list the values of Δ , as the difference between successive materials, if successive pairs of TM elements from the list to create the double perovskite. The local correlation strength U is moderate, ranging between 1eV and 3eV [107][108]. Hence, $\Delta/U \sim 0.3$ required for the 'finite-T' half metal, can be achieved easily. Assuming typical cubic

4d	SrZrO ₃	SrNbO ₃	SrMoO ₃	SrTcO ₃	SrRuO ₃	SrRhO ₃
ϵ_p (eV)	-6.23	-6.03	-5.31	-4.41	-3.40	-2.47
Δ (eV)		-0.23	-0.72	-0.9	-1.01	-0.93

double perovskites with octahedral crystal field, the $4d$ orbitals are known to split. For the $4d$ TM atom octahedral crystal field splits the $5d$ orbitals by $\Delta_{CEF} = 3\text{eV}$ to 4eV [109], into high energy e_g and low energy t_{2g} levels. Given these estimates, we have $\Delta \ll \Delta_{CEF}$, that implies that Δ does not induce any $t_{2g} - e_g$ hybridization. This facilitates the formation of partially filled t_{2g} bands. We suggest that suitable choice of X site element can be made for half-filled t_{2g} manifold. X also plays the role the parameter for tune U by controlling the electronic bandwidth. nnn hopping is also relevant for $4d$ TM elements[110][111] due to larger spatial extent of the $4d$ orbitals as compared to $3d$ TM elements. Hence one can potentially identify a number of candidates that are insulators with small charge gap, such as Sr₂RuMoO₆ [112]. Based on the above mentioned literature we can crudely estimate $U_{Re/Mo} \sim 3$ eV, $\Delta \sim 1 - 2$ eV and a $t_{2g} - e_g$ splitting of 3eV. These estimates yield $\Delta/U \sim 0.3 - 0.6$ eV, which is within the ballpark of the ratio needed for HM₂

for $\text{Sr}_2\text{RuMoO}_6$. We expect complete quenching of orbital angular momentum in a half-filled t_{2g} 4d orbital; however, one has to investigate the role of small Hund's coupling [113], prior to identifying realistic material candidates.

b. Cold atomic lattices: We now briefly discuss how the 'finite-T' half metal can be realized in cold atomic lattice. IHM has recently been realized for fermionic cold atomic systems for hexagonal lattice [114]. This experiment showed the band to Mott insulator transition by tracking suppression of double occupation over wide variations of Δ and U $[0, 41t]$ and $[0, 30t]$, respectively, in the units of nearest-neighbor hopping strength $t/h \sim 174\text{Hz}$. This range of parameter variation should be easily possible for the square lattice as well. t'/t ratio can be tuned over a large window on shaken optical lattices [115]. Also, the highest $T_S/t \sim 0.1$ is within the ballpark of the experimental temperature scales of $0.2t$ [116][117]. We suggest that, δn would be the natural quantity to measure as a signature of HM_2 , analogous to spin polarization measurements for metallic (Stoner) ferromagnets in cold atomic systems [116].

4.7 Conclusions

To summarize, we have shown that a subtle interplay of U and Δ can stabilize an antiferromagnetic Mott insulating ground state with unequal charge gaps for the two spin channels in half-filled IHM. We have demonstrated a temperature-driven transition from this antiferromagnetic Mott insulator to the novel ferrimagnetic half-metal, at a U dependent onset temperature. We have revealed that the spin polarization is 100% in the vicinity of the onset temperature within numerical accuracy. Finally, we have shown that enhancing the onset temperature by increasing U does not degrade the spin polarization. The mechanism of the finite T half metal is distinct from all previous low T half metals. In particular, unlike double exchange mechanism, there is no interaction between large Hund's coupled core spins and itinerant electrons. Also it is different from the Slater-Pauling rule in the Heusler alloys and clearly unlike the low T half metal HM_1 . Unlike all previous propos-

als where half metallicity is a ground state property, here we have demonstrated that a half-metal can emerge from a Mott insulating ground state. The insulating ground state ensures that the half-metal with 100% spin polarization occurs at a finite temperature and protects against temperature-induced depolarization effects. *Comparison with quantum approaches:* As discussed in chapter 2 that results found from s-MC study of Hubbard model in the unfrusted case are in good agreement with DQMC calculation of the model but the s-MC study underestimates the phase boundary (critical parameter value of a transition) due to lack of quantum coherence in the system. Similar conclusions can also be seen for the ionic Hubbard model in Phys. Rev. B **103**, 155132 (2021), which compares CDMFT phase boundary with Hartree-Fock (the low T limit of s-MC). While there is no reliable finite T quantum calculation data for the frustrated case, we believe the finite T magnetic boundaries will be underestimated in s-MC in this case as well.

The experimental realization of this unique finite-temperature half-metal will be a significant step toward the goal of creating spin-polarized current sources at room temperature,. We have identified a class of TM double perovskites where the finite T half metal can be realized.

Appendix A

Momentum space mean-field theory

Here, we will do the Fourier transformation of the Hubbard Hamiltonian in Eq.1.2. Using Eq.1.3 and Eq.1.4 (from chapter 1) to get the mean-field band dispersion.

Then, the Hamiltonian can be written as

$$\begin{aligned} H^{HF} = & -t \sum_{\langle ij \rangle, \sigma} c_{i\sigma}^{\dagger} c_{j\sigma} + UN(m^2 - \frac{1}{4}n^2) + Um \sum_i (-1)^{x_i+y_i} (n_{i\uparrow} - n_{i\downarrow}) \\ & - (\mu - \frac{1}{2}Un) \sum_i (n_{i\uparrow} + n_{i\downarrow}) \end{aligned} \quad (\text{A.1})$$

N is the total number of sites in the system. Now, Fourier transforming using $c_{i\sigma} = \frac{1}{\sqrt{N}} \sum_k c_k e^{-ik \cdot r_i}$ we get the Hamiltonian as

$$H^{HF} = \sum_{k, \sigma} H_{k\sigma} + UN(m^2 - \frac{1}{4}n^2) \quad (\text{A.2})$$

With

$$H_{k\sigma} = (\epsilon_k + \frac{1}{2}Un)n_{k\sigma} + (\epsilon_{k+\pi} + \frac{1}{2}Un)n_{k+\pi\sigma} - \sigma Um(c_{k\sigma}^{\dagger} c_{k+\pi\sigma} + c_{k+\pi\sigma}^{\dagger} c_{k\sigma}) \quad (\text{A.3})$$

k runs over the Brillouin zone with $|k_x \pm k_y| = \pi$. The density, n and staggered

magnetization, m are calculated self-consistently using the equations

$$n = \sum_k [f(E_k^+) + f(E_k^-)] \quad (\text{A.4})$$

$$m = \frac{Um}{N} \sum_k \frac{[f(E_k^+) + f(E_k^-)]}{[(\frac{1}{2}(\epsilon_k + \epsilon_{k+\pi}))^2 + U^2m^2]^{\frac{1}{2}}} \quad (\text{A.5})$$

$f(E_k^\sigma)$ is the Fermi function and non-interacting dispersion relation is

$\epsilon_k = -2t(\cos k_x + \cos k_y)$ on a square lattice.

Finally, we get the mean-field band dispersion which is given below.

$$E_k^\pm = \frac{1}{2}Un - \mu \pm \sqrt{[4t^2(\cos k_x + \cos k_y)^2 + U^2m^2]} \quad (\text{A.6})$$

'+' and '-' refer to the conduction and valance bands respectively and $m \neq 0$ implies G-type magnetic order.

Appendix B

Slater insulator at weak coupling

Here we derive the SDW energy gap in the weak coupling limit. For that, we write the Hamiltonian in Eq.1.9 (in chapter 1) in a basis γ to diagonalize it. The basis transformation is given below.

$$\begin{aligned}\gamma_{k\uparrow}^a &= u_k c_{k\uparrow} + v_k c_{k+Q\uparrow} \\ \gamma_{k\uparrow}^b &= v_k c_{k\uparrow} - u_k c_{k+Q\uparrow} \\ \gamma_{k\downarrow}^a &= u_k c_{k\downarrow} - v_k c_{k+Q\downarrow} \\ \gamma_{k\downarrow}^b &= v_k c_{k\downarrow} + u_k c_{k+Q\downarrow}\end{aligned}\tag{B.1}$$

The corresponding inverse basis transformation is given as follows.

$$\begin{aligned}c_{k\uparrow} &= u_k \gamma_{k\uparrow}^a - v_k \gamma_{k\uparrow}^b \\ c_{k+Q\uparrow} &= v_k \gamma_{k\uparrow}^a + u_k \gamma_{k\uparrow}^b \\ c_{k\downarrow} &= u_k \gamma_{k\downarrow}^a + v_k \gamma_{k\downarrow}^b \\ c_{k+Q\downarrow} &= -v_k \gamma_{k\downarrow}^a + u_k \gamma_{k\downarrow}^b\end{aligned}\tag{B.2}$$

Here, a and b stand for conduction and valance bands respectively. Using these transformation we get the following relation from the first term in the Eq.1.9 (in chapter 1).

$$\begin{aligned} n_{k\uparrow} - n_{k+Q\uparrow} &= (u_k^2 \gamma_{k\uparrow}^{a\dagger} \gamma_{k\uparrow}^a + v_k^2 \gamma_{k\uparrow}^{b\dagger} \gamma_{k\uparrow}^b - u_k v_k (\gamma_{k\uparrow}^{a\dagger} \gamma_{k\uparrow}^b + \gamma_{k\uparrow}^{b\dagger} \gamma_{k\uparrow}^a)) \\ &\quad - (v_k^2 \gamma_{k\uparrow}^{a\dagger} \gamma_{k\uparrow}^a + u_k^2 \gamma_{k\uparrow}^{b\dagger} \gamma_{k\uparrow}^b + u_k v_k (\gamma_{k\uparrow}^{a\dagger} \gamma_{k\uparrow}^b + \gamma_{k\uparrow}^{b\dagger} \gamma_{k\uparrow}^a)) \end{aligned} \quad (\text{B.3})$$

$$\begin{aligned} n_{k\downarrow} - n_{k+Q\downarrow} &= (u_k^2 \gamma_{k\downarrow}^{a\dagger} \gamma_{k\downarrow}^a + v_k^2 \gamma_{k\downarrow}^{b\dagger} \gamma_{k\downarrow}^b + u_k v_k (\gamma_{k\downarrow}^{a\dagger} \gamma_{k\downarrow}^b + \gamma_{k\downarrow}^{b\dagger} \gamma_{k\downarrow}^a)) \\ &\quad - (v_k^2 \gamma_{k\downarrow}^{a\dagger} \gamma_{k\downarrow}^a + u_k^2 \gamma_{k\downarrow}^{b\dagger} \gamma_{k\downarrow}^b - u_k v_k (\gamma_{k\downarrow}^{a\dagger} \gamma_{k\downarrow}^b + \gamma_{k\downarrow}^{b\dagger} \gamma_{k\downarrow}^a)) \end{aligned} \quad (\text{B.4})$$

Hence,

$$n_{k\uparrow} - n_{k+Q\uparrow} = (u_k^2 - v_k^2) (\gamma_{k\uparrow}^{a\dagger} \gamma_{k\uparrow}^a - \gamma_{k\uparrow}^{b\dagger} \gamma_{k\uparrow}^b) - 2u_k v_k (\gamma_{k\uparrow}^{a\dagger} \gamma_{k\uparrow}^b + \gamma_{k\uparrow}^{b\dagger} \gamma_{k\uparrow}^a) \quad (\text{B.5})$$

$$n_{k\downarrow} - n_{k+Q\downarrow} = (u_k^2 - v_k^2) (\gamma_{k\downarrow}^{a\dagger} \gamma_{k\downarrow}^a - \gamma_{k\downarrow}^{b\dagger} \gamma_{k\downarrow}^b) + 2u_k v_k (\gamma_{k\downarrow}^{a\dagger} \gamma_{k\downarrow}^b + \gamma_{k\downarrow}^{b\dagger} \gamma_{k\downarrow}^a) \quad (\text{B.6})$$

The second term gives

$$\begin{aligned} c_{k+Q\uparrow}^\dagger c_{k\uparrow} + c_{k\uparrow}^\dagger c_{k+Q\uparrow} &= 2u_k v_k (\gamma_{k\uparrow}^{a\dagger} \gamma_{k\uparrow}^a - \gamma_{k\uparrow}^{b\dagger} \gamma_{k\uparrow}^b) + (u_k^2 - v_k^2) (\gamma_{k\uparrow}^{a\dagger} \gamma_{k\uparrow}^b + \gamma_{k\uparrow}^{b\dagger} \gamma_{k\uparrow}^a) \\ c_{k+Q\downarrow}^\dagger c_{k\downarrow} + c_{k\downarrow}^\dagger c_{k+Q\downarrow} &= -2u_k v_k (\gamma_{k\downarrow}^{a\dagger} \gamma_{k\downarrow}^a - \gamma_{k\downarrow}^{b\dagger} \gamma_{k\downarrow}^b) + (u_k^2 - v_k^2) (\gamma_{k\downarrow}^{a\dagger} \gamma_{k\downarrow}^b + \gamma_{k\downarrow}^{b\dagger} \gamma_{k\downarrow}^a) \end{aligned} \quad (\text{B.7})$$

So, the effective Hamiltonian becomes

$$H_{eff} = \sum_{k,\sigma}^l [(\epsilon_k (u_k^2 - v_k^2) - 2USu_k v_k) (\gamma_{k\sigma}^{a\dagger} \gamma_{k\sigma}^a - \gamma_{k\sigma}^{b\dagger} \gamma_{k\sigma}^b) + \sigma (US(u_k^2 - v_k^2) - 2\epsilon_k u_k v_k) (\gamma_{k\sigma}^{a\dagger} \gamma_{k\sigma}^b + \gamma_{k\sigma}^{b\dagger} \gamma_{k\sigma}^a)] \quad (\text{B.8})$$

Setting the off-diagonal term zero we have

$$\Delta(u_k^2 - v_k^2) + 2\epsilon_k u_k v_k = 0 \quad (\text{B.9})$$

Where, $\Delta = -US$, is the SDW energy gap scale.

As $u_k^2 + v_k^2 = 1$, defining the relation $E_k = \sqrt{\epsilon_k^2 + \Delta^2}$ we found the coefficients as

$$\begin{aligned} u_k &= \left[\frac{1}{2} \left(1 + \frac{\epsilon_k}{E_k} \right) \right]^{\frac{1}{2}} \\ v_k &= \left[\frac{1}{2} \left(1 - \frac{\epsilon_k}{E_k} \right) \right]^{\frac{1}{2}} \end{aligned} \quad (\text{B.10})$$

Then the final effective Hamiltonian will have the following form.

$$H_{eff} = \sum_{k,\sigma} E_k (\gamma_{k\sigma}^{a\dagger} \gamma_{k\sigma}^a - \gamma_{k\sigma}^{b\dagger} \gamma_{k\sigma}^b) \quad (\text{B.11})$$

In the spin density wave ground state $\gamma_{k\sigma}^{b\dagger} |\Omega\rangle = \gamma_{k\sigma}^a |\Omega\rangle = 0$ and then the variational parameter can be calculated in the ground state.

$$\begin{aligned} \langle \Omega | S_Q^z | \Omega \rangle &= S = -\frac{1}{2N} 2 \sum_k u_k v_k \\ &= \frac{1}{4N} \sum_k \frac{\Delta}{E_k} = -\frac{\Delta}{U} \end{aligned} \quad (\text{B.12})$$

Changing the summation over k to integration of ϵ and using density of states that has singularity at $\epsilon = 0$ we get the gap equation in the weak coupling limit.

$$\Delta \sim t e^{-2\pi\sqrt{t/U}}$$

This is the SDW energy gap in the weak coupling limit.

Appendix C

Strong coupling Heisenberg limit

To get to the Heisenberg model, we do a toy calculation of Hubbard model ($H = -t \sum_{\langle i,j \rangle, \sigma} (c_{i\sigma}^\dagger c_{j\sigma} + h.c.) + U \sum_i n_{i\uparrow} n_{i\downarrow}$, the notations carry usual meaning) with two sites and two electrons. In this situation the possible basis states would be

$$\begin{aligned} |\uparrow, \downarrow\rangle &= c_{2\downarrow}^\dagger c_{1\uparrow}^\dagger |0\rangle \\ |\downarrow, \uparrow\rangle &= c_{2\uparrow}^\dagger c_{1\downarrow}^\dagger |0\rangle \\ |\uparrow\downarrow, \cdot\rangle &= c_{1\downarrow}^\dagger c_{1\uparrow}^\dagger |0\rangle \\ |\cdot, \uparrow\downarrow\rangle &= c_{2\downarrow}^\dagger c_{2\uparrow}^\dagger |0\rangle \end{aligned} \tag{C.1}$$

$|\uparrow, \downarrow\rangle$ and $|\downarrow, \uparrow\rangle$ are covalent states. Whereas, $|\uparrow\downarrow, \cdot\rangle$ and $|\cdot, \uparrow\downarrow\rangle$ are ionic states. The matrix form of the Hamiltonian in the basis will have the following form.

$$\mathbf{H} = \begin{array}{cccc|c} \langle \uparrow, \downarrow | & \langle \downarrow, \uparrow | & \langle \uparrow \downarrow, \cdot | & \langle \cdot, \uparrow \downarrow | & \\ \hline 0 & 0 & -t & -t & |\uparrow, \downarrow\rangle \\ 0 & 0 & +t & +t & |\downarrow, \uparrow\rangle \\ -t & +t & U & 0 & |\uparrow \downarrow, \cdot\rangle \\ -t & +t & 0 & U & |\cdot, \uparrow \downarrow\rangle \end{array}$$

After diagonalization we get the eigenvalues

$$\begin{aligned} \epsilon_{\pm} &= \frac{U}{2} \pm \frac{\sqrt{U^2 + 16t^2}}{2} & (C.2) \\ \epsilon_{cov} &= 0 \\ \epsilon_{ion} &= U \end{aligned}$$

And the correspondig eigenvectors are

$$\begin{aligned} \psi_{\pm} &= \frac{[|\uparrow, \downarrow\rangle - |\downarrow, \uparrow\rangle - \frac{\epsilon_{\pm}}{2t}(|\uparrow \downarrow, \cdot\rangle + |\cdot, \uparrow \downarrow\rangle)]}{\sqrt{2 + \frac{\epsilon_{\pm}^2}{2t^2}}} & (C.3) \\ \psi_{cov} &= \frac{1}{\sqrt{2}}(|\uparrow, \downarrow\rangle + |\downarrow, \uparrow\rangle) \\ \psi_{ion} &= \frac{1}{\sqrt{2}}(|\uparrow \downarrow, \cdot\rangle - |\cdot, \uparrow \downarrow\rangle) \end{aligned}$$

In the large U limit $\epsilon_{cov} = 0$ and $\epsilon_{-} \sim \frac{-4t^2}{U}$

Therefore, ψ_{-} is largely covalent with a small ionic admixture.

Now, we project out the low energy states of Hilbert space with the help of down-folding.

The block inversion of a matrix can be obtained in the following manner. Let's take

the matrix

$$\mathbf{A} = \begin{bmatrix} A0 & A1 \\ A2 & A3 \end{bmatrix}$$

Let's consider the inversion of the A matrix will be

$$\mathbf{A}^{-1} = \begin{bmatrix} B0 & B1 \\ B2 & B3 \end{bmatrix}$$

Then we can write the matrix elements of the inverse matrix A^{-1} in terms elements of original matrix A as given below.

$$B0 = (A0 - A1.A3^{-1}.A2)^{-1} \quad (\text{C.4})$$

$$B1 = -B0.A1.A3^{-1}$$

$$B2 = -A3^{-1}.A2.A3^{-1}$$

$$B3 = A3^{-1} - (B2 - A1.A3^{-1}.A2)^{-1}$$

We follow the same procedure to Hamiltonian in terms of block matrices and invert to calculate the Green's function.

$$\mathbf{H} = \begin{bmatrix} 0 & 0 & -t & -t \\ 0 & 0 & +t & +t \\ -t & +t & U & 0 \\ -t & +t & 0 & U \end{bmatrix}$$

$$\equiv \begin{bmatrix} H_{00} & T_{01} \\ T_{10} & H_{11} \end{bmatrix}$$

Where, H_{00} , H_{11} , and T_{ij} are covalent Hamiltonian, ionic Hamiltonian and covalent-ionic transitions respectively.

The Green's function can have the form

$$G(\epsilon) \equiv (\epsilon - H)^{-1} = \begin{bmatrix} \epsilon - H_{00} & -T_{01} \\ -T_{10} & \epsilon - H_{11} \end{bmatrix}^{-1} .$$

$$\equiv \begin{bmatrix} G_{00} & G_{01} \\ G_{10} & G_{11} \end{bmatrix}$$

The energy-dependent covalent part G_{00} can be written as

$$G_{00}(\epsilon) = (\epsilon - [H_{00} + T_{01}(\epsilon - H_{11})^{-1}T_{10}])^{-1}$$

This reduces to $G_{00}(\epsilon) = (\epsilon - H_{eff})^{-1}$, definition of Green's function. It can be easily found an effective Hamiltonian having the form

$$H_{eff}(\epsilon) = H_{00} + T_{01}(\epsilon - H_{11})^{-1}T_{10} \simeq H_{eff}(\epsilon_0) \text{ with } \epsilon_0 \text{ being the typical covalent energy. Here } \epsilon_0 = 0$$

So, the effective Hamiltonian in the covalent states becomes after plug in the block matrices

$$H_{eff}(0) = -\frac{2t^2}{U} \begin{array}{c} \langle \uparrow, \downarrow | \quad \langle \downarrow, \uparrow | \\ \left[\begin{array}{cc} 1 & -1 \\ -1 & 1 \end{array} \right] \begin{array}{c} | \uparrow, \downarrow \rangle \\ | \downarrow, \uparrow \rangle \end{array} \end{array}$$

After diagonalizing the 2×2 matrix we have eigenvalues and eigenvectors.

$$\epsilon_s = \frac{-4t^2}{U}; \psi_s \simeq \frac{1}{\sqrt{2}}(| \uparrow, \downarrow \rangle - | \downarrow, \uparrow \rangle) \text{ (}\psi_s \text{ has small ionic admixture.)}$$

and

$$\epsilon_t = 0; \psi_t = \frac{1}{\sqrt{2}}(| \uparrow, \downarrow \rangle + | \downarrow, \uparrow \rangle) ; \text{ Where 's' and 't' correspond to singlet and}$$

triplet states. The energy corresponds to the other triplet states $|\uparrow, \uparrow\rangle$ and $|\downarrow, \downarrow\rangle$ also are zero because of restriction of Pauli principle in the hopping of electrons. In terms of fermionic operators the effective Hamiltonian will look like as the following.

$$H_{eff} = -\frac{2t^2}{U}(c_{1\downarrow}^\dagger c_{1\downarrow} c_{2\uparrow}^\dagger c_{2\uparrow} - c_{1\uparrow}^\dagger c_{1\downarrow} c_{2\downarrow}^\dagger c_{2\uparrow} - c_{1\downarrow}^\dagger c_{1\uparrow} c_{2\uparrow}^\dagger c_{2\downarrow} + c_{1\uparrow}^\dagger c_{1\uparrow} c_{2\downarrow}^\dagger c_{2\downarrow}) \quad (C.5)$$

We can rewrite H_{eff} using the properties of Pauli spin matrices.

$$H_{eff} = \frac{4t^2}{U}(\mathbf{S}_1 \cdot \mathbf{S}_2 - \frac{\mathbf{n}_1 \mathbf{n}_2}{4}) \quad (C.6)$$

($n_i = n_{i\uparrow} + n_{i\downarrow}$ for i^{th} site) For half-filling the 2^{nd} term gives $\frac{1}{4}$ and hence ignoring that term we have

$$H_{eff} = \frac{4t^2}{U}(\mathbf{S}_1 \cdot \mathbf{S}_2) \quad (C.7)$$

In the Heisenberg Hamiltonian shown above J is the anti-ferromagnetic coupling constant with $J = \frac{4t^2}{U}$. The above calculation is a quick demonstration, the same result can also be derived from the degenerate perturbation calculation with more number of sites.

Appendix D

Inhomogeneous mean-field theory

Here, we derive the mean-field form of the Hubbard Hamiltonian. Let's consider the interaction term of the Hubbard model:

$$H_U = U \sum_i n_{i\uparrow} n_{i\downarrow}$$

Where, U is the repulsive Hubbard interaction strength and $n_{i\sigma}$ is the number operator at i^{th} site for the spin σ ($\sigma = \uparrow$ or \downarrow).

Hartree term:

The Hartree decomposition for the quadratic interaction term $n_{i\uparrow} n_{i\downarrow} = c_{i\uparrow}^\dagger c_{i\uparrow} c_{i\downarrow}^\dagger c_{i\downarrow}$ is given below. Here, $c_{i\sigma}^\dagger$ and $c_{i\sigma}$ are the creation and annihilation operator of electron at site 'i' of the spin σ ($\sigma = \uparrow$ or \downarrow).

$$\begin{aligned} n_{i\uparrow} n_{i\downarrow} &= n_{i\uparrow} \langle n_{i\downarrow} \rangle + n_{i\downarrow} \langle n_{i\uparrow} \rangle - \langle n_{i\downarrow} \rangle \langle n_{i\uparrow} \rangle \\ &= 1/2 (n_{i\uparrow} \langle n_i \rangle - n_{i\uparrow} \langle n_{i\uparrow} \rangle + n_{i\uparrow} \langle n_{i\downarrow} \rangle + \langle n_i \rangle n_{i\downarrow} - n_{i\downarrow} \langle n_{i\downarrow} \rangle + n_{i\downarrow} \langle n_{i\uparrow} \rangle - 2 \langle n_{i\downarrow} \rangle \langle n_{i\uparrow} \rangle) \\ &= 1/2 (n_i \langle n_i \rangle - n_{i\downarrow} \langle n_i \rangle - 2 S_{iz} \langle n_{i\uparrow} \rangle + n_{i\uparrow} \langle n_{i\downarrow} \rangle + n_{i\downarrow} \langle n_{i\uparrow} \rangle - 2 \langle n_{i\downarrow} \rangle \langle n_{i\uparrow} \rangle) \\ &= 1/2 (n_i \langle n_i \rangle - 4 S_{iz} \langle S_{iz} \rangle + 2 \langle S_{iz} \rangle^2 - 1/2 \langle n_i \rangle^2) \end{aligned} \tag{D.1}$$

The spin operator is $\mathbf{S}_i = \frac{\hbar}{2} \sum_{\alpha, \beta} c_{i, \alpha}^\dagger \sigma_{\alpha, \beta} c_{i, \beta}$ and $\{\sigma^x, \sigma^y, \sigma^z\}$ are the Pauli matrices. Here, S_{iz} is the z-component of the spin.

Fock term:

The Fock term of the interaction Hamiltonian is in the following.

$$\begin{aligned}
n_{i\uparrow}n_{i\downarrow} &= c_{i\uparrow}^\dagger c_{i\uparrow} c_{i\downarrow}^\dagger c_{i\downarrow} \\
&= -\langle c_{i\uparrow}^\dagger c_{i\downarrow} \rangle c_{i\downarrow}^\dagger c_{i\uparrow} - c_{i\uparrow}^\dagger c_{i\downarrow} \langle c_{i\downarrow}^\dagger c_{i\uparrow} \rangle + \langle c_{i\uparrow}^\dagger c_{i\downarrow} \rangle \langle c_{i\downarrow}^\dagger c_{i\uparrow} \rangle \\
&= -\langle S_i^+ \rangle S_i^- - S_i^+ \langle S_i^- \rangle + \langle S_i^+ \rangle \langle S_i^- \rangle \\
&= -2(S_{ix} \langle S_{ix} \rangle + S_{iy} \langle S_{iy} \rangle + \langle S_{ix} \rangle^2 + \langle S_{iy} \rangle^2)
\end{aligned} \tag{D.2}$$

S_{ix} and S_{iy} are x and y components of the spin respectively.

Then the effective Hubbard interaction becomes

$$\begin{aligned}
H_U^{HF} &= \text{Hartree} + \text{Fock} \\
&= U \sum_i \left[\frac{1}{2} (n_i \langle n_i \rangle - 4S_{iz} \langle S_{iz} \rangle + 2\langle S_{iz} \rangle^2 - 1/2 \langle n_i \rangle^2) - 2(S_{ix} \langle S_{ix} \rangle + S_{iy} \langle S_{iy} \rangle + \langle S_{ix} \rangle^2 + \langle S_{iy} \rangle^2) \right] \\
&= U/2 \sum_i [n_i \langle n_i \rangle + 2\langle \vec{S}_i \rangle^2 - 4\vec{S}_i \langle \vec{S}_i \rangle - 1/2 \langle n_i \rangle^2]
\end{aligned} \tag{D.3}$$

Therefore, the total effective mean-field Hubbard Hamiltonian in real space will be

$$H^{HF} = -t \sum_{\langle ij \rangle, \sigma} c_{i\sigma}^+ c_{j\sigma} + \frac{U}{2} \sum_i [n_i \langle n_i \rangle + 2\langle \vec{S}_i \rangle^2 - 4\vec{S}_i \langle \vec{S}_i \rangle - 1/2 \langle n_i \rangle^2] \tag{D.4}$$

Appendix E

Definitions of indicators

Here, we define the indicators (observables) used in this thesis. We use 200 copies out of 2000 thermalized configurations leaving 10 MC sweeps to avoid self-correlations in the data to calculate all the observables. Again, the results found from 10-20 different runs with distinct random seeds are averaged over to obtain final results for each of the observables at every temperature.

a. Static magnetic structure factor:

The static magnetic structure factor S_q is the Fourier transform of spin-spin correlation and is defined as the following.

$$S_q = \frac{1}{N} \sum_{i,j} e^{i\mathbf{q}\cdot(\mathbf{r}_i - \mathbf{r}_j)} \langle \mathbf{S}_i \cdot \mathbf{S}_j \rangle, \quad (\text{E.1})$$

Where i and j run over all the sites on the lattice and N is the total number of sites in the system.

b. Total density of states (DOS) and the spin resolved form of the DOS:

The total density of states is defined as

$$N(\omega) = \sum_{\gamma} \delta(\omega - \epsilon_{\gamma}) \quad (\text{E.2})$$

Where, ϵ_{γ} are the eigenvalues of the fermionic sector and the summation runs over

all the eigenvalues of $H_e f f$.

The spin resolved form of DOS is given by

$$N_{\alpha,\sigma}(\omega) = \sum_{\gamma} |\langle \alpha, \sigma | \Psi_{\gamma} \rangle|^2 \delta(\omega - \epsilon_{\gamma}) \quad (\text{E.3})$$

Here $\alpha \in \{A, B\}$, the two sub-lattices and σ is the spin index. $|\Psi_{\gamma}\rangle$ are the eigenvectors corresponds to the eigenvalues ϵ_{γ} . Lorentzian representation of the above δ function is used to compute DOS. The broadening of the Lorentzian is $\sim BW/2N$. Where BW is the non-interacting bandwidth and N is the total number of lattice sites in the system.

c. Optical conductivity:

The total d.c conductivity σ_{dc} along x-direction is calculated using the Kubo-Greenwood formalism [118] for optical conductivity.

$$\sigma(\omega) = \frac{\pi e^2}{N \hbar a_0} \sum_{\alpha,\beta} (n_{\alpha} - n_{\beta}) \frac{|f_{\alpha\beta}|^2}{\epsilon_{\beta} - \epsilon_{\alpha}} \delta(\omega - (\epsilon_{\beta} - \epsilon_{\alpha})). \quad (\text{E.4})$$

Where, $f_{\alpha\beta}$ are the matrix elements for the current operator and has the form of $\langle \psi_{\alpha} | j_x | \psi_{\beta} \rangle$. The non-interacting current operator is defined by $j_x = ia_0 \sum_{i,\sigma} [t(c_{i,\sigma}^{\dagger} c_{i+a_0\hat{x},\sigma} - h.c) + t'(c_{i,\sigma}^{\dagger} c_{i+a_0\hat{x}+a_0\hat{y},\sigma} - h.c)]$. Here, ψ_{α} and ϵ_{α} indicate the single-particle eigenstates and corresponding eigenvalues respectively. $n_{\alpha} = f(\mu - \epsilon_{\alpha})$ is the Fermi function. We calculate the average d.c. conductivity by integrating over small frequency window as $\sigma_{dc} = (\Delta\omega)^{-1} \int_0^{\Delta\omega} \sigma(\omega) d\omega$. The interval is taken as $\Delta\omega \sim 0.005t$. The spin resolved conductivity, σ_{dc} is calculated using appropriate spin resolved states and operators by constructing $f_{\alpha\beta}^{\sigma} = \langle \psi_{\alpha} | j_x^{\sigma} | \psi_{\beta} \rangle$ in the conductivity formula. The resistivity is found from the inverse of the average dc conductivity. The conduction electron polarization, $P(T)$ is computed from $\frac{\sigma_{dc,\uparrow}(\mu) - \sigma_{dc,\downarrow}(\mu)}{\sigma_{dc,\uparrow}(\mu) + \sigma_{dc,\downarrow}(\mu)}$ using the relation $J_x^{\sigma} \propto \sigma_{dc,\sigma}^{xx}$. Here, up refers to the electron spin channel which delocalizes to form the half-metal.

d. Local moment and it's real space distribution and double occupancy:

The double occupation (D) and local moment (M) are defined as the following.

$$D = \langle n_{\uparrow} n_{\downarrow} \rangle \quad (\text{E.5})$$

$$\begin{aligned} M &= \langle (n_{\uparrow} - n_{\downarrow})^2 \rangle \\ &= \langle n \rangle - 2\langle n_{\uparrow} n_{\downarrow} \rangle \end{aligned}$$

Where n_{\uparrow} and n_{\downarrow} are the number operators for up and down electrons.

The sublattice resolved double occupancy and local moment have the following form.

$$D^{\alpha} = \langle n_{\uparrow}^{\alpha} n_{\downarrow}^{\alpha} \rangle \quad (\text{E.6})$$

$$\begin{aligned} M^{\alpha} &= \langle (n_{\uparrow}^{\alpha} - n_{\downarrow}^{\alpha})^2 \rangle \\ &= \langle n^{\alpha} \rangle - 2\langle n_{\uparrow}^{\alpha} n_{\downarrow}^{\alpha} \rangle \end{aligned}$$

Here, $\alpha \in \{A, B\}$, the sublattices. The distribution of local moment is given by

$$P(M) = \sum_{M_i} \delta(M - M_i) \quad (\text{E.7})$$

The notations carry usual meaning and are defined before.

e. The spin and sub-lattice resolved density:

The expression for average spin and sub-lattice resolved density is given by

$$\langle n_{\alpha\sigma} \rangle = \frac{2}{N} \sum_{i \in \alpha, \gamma} |\langle i\sigma | \Psi_{\gamma} \rangle|^2 f(\epsilon_{\gamma} - \mu) \quad (\text{E.8})$$

where, $\alpha \in \{A, B\}$, σ is the spin index and ϵ_{γ} is the eigenvalue corresponding to the eigenvector γ . $f(\epsilon_{\gamma} - \mu)$ is the Fermi function and μ denotes the chemical potential.

The sub-lattice resolved occupation is calculated by summing over density for A and

B , for each spin independently. The sublattice magnetization is calculated using the up and down densities.

e. Real space spin correlation:

The spin correlation function is defined as,

$$C(|\mathbf{r}|) = \frac{1}{P} \sum_{|\mathbf{r}|=|\mathbf{i}-\mathbf{j}|, a} (-1)^{|\mathbf{i}-\mathbf{j}|} \langle S_i^a S_j^a \rangle. \quad (\text{E.9})$$

In $C(|\mathbf{r}|)$ the summation runs over all P pairs of sites at a Manhattan distance $|\mathbf{r}|$ and is normalized accordingly. The sum over a runs over the three directions x , y , and z .

References

- [1] J. Hubbard and Brian Hilton Flowers. “Electron correlations in narrow energy bands”. In: *Proceedings of the Royal Society of London. Series A. Mathematical and Physical Sciences* 276.1365 (1963), pp. 238–257. eprint: <https://royalsocietypublishing.org/doi/pdf/10.1098/rspa.1963.0204>.
- [2] V. J. Emery and S. A. Kivelson. “Superconductivity in Bad Metals”. In: *Phys. Rev. Lett.* 74 (16 1995), pp. 3253–3256.
- [3] Y. Xia et al. “Observation of a large-gap topological-insulator class with a single Dirac cone on the surface”. In: *Nature Physics* 5.6 (2009), pp. 398–402. ISSN: 1745-2481.
- [4] J. S. Kim et al. “Specific heat in high magnetic fields and non-Fermi-liquid behavior in CeMIn_5 ($M = \text{Ir, Co}$)”. In: *Phys. Rev. B* 64 (13 2001), p. 134524.
- [5] S. Nakatsuji et al. “Intersite Coupling Effects in a Kondo Lattice”. In: *Phys. Rev. Lett.* 89 (10 2002), p. 106402.
- [6] Susanne Stemmer and S James Allen. “Non-Fermi liquids in oxide heterostructures”. en. In: *Rep Prog Phys* 81.6 (Apr. 2018), p. 062502.
- [7] Hiroshi Ishida and Ansgar Liebsch. “Fermi-liquid, non-Fermi-liquid, and Mott phases in iron pnictides and cuprates”. In: *Phys. Rev. B* 81 (5 2010), p. 054513.
- [8] M. Brian Maple et al. “Non-Fermi Liquid Regimes and Superconductivity in the Low Temperature Phase Diagrams of Strongly Correlated d- and f-

- Electron Materials”. In: *Journal of Low Temperature Physics* 161.1 (2010), pp. 4–54. ISSN: 1573-7357.
- [9] Tao Hu et al. “Non-Fermi liquid regimes with and without quantum criticality in $\text{Ce}_{1-x}\text{Y}_x\text{CoIn}_5$ ”. In: *Proceedings of the National Academy of Sciences* 110.18 (2013), pp. 7160–7164. ISSN: 0027-8424. eprint: <https://www.pnas.org/content/110/18/7160.full.pdf>.
- [10] M V Sadovskii. “Planckian relaxation delusion in metals”. In: *Physics-Uspekhi* 64.2 (2021), pp. 175–190.
- [11] Philip W. Anderson. “In praise of unstable fixed points: the way things actually work”. In: *Physica B-condensed Matter* 318 (2002), pp. 28–32.
- [12] Edwin W. Huang et al. “Stripe order from the perspective of the Hubbard model”. In: *npj Quantum Materials* 3.1 (2018), p. 22. ISSN: 2397-4648.
- [13] Ke Liu et al. “The pairing symmetries in the two-dimensional Hubbard model”. In: *Physics Letters A* 392 (2021), p. 127153. ISSN: 0375-9601.
- [14] Rubem Mondaini et al. “Determinant quantum Monte Carlo study of the enhancement of d -wave pairing by charge inhomogeneity”. In: *Phys. Rev. B* 86 (18 2012), p. 184506.
- [15] Peizhi Mai et al. “Intertwined spin, charge, and pair correlations in the two-dimensional Hubbard model in the thermodynamic limit”. In: *Proceedings of the National Academy of Sciences* 119.7 (2022), e2112806119. eprint: <https://www.pnas.org/doi/pdf/10.1073/pnas.2112806119>.
- [16] Astrid T. Rømer et al. “Pairing in the two-dimensional Hubbard model from weak to strong coupling”. In: *Phys. Rev. Research* 2 (1 2020), p. 013108.
- [17] Emanuel Gull et al. “Momentum-sector-selective metal-insulator transition in the eight-site dynamical mean-field approximation to the Hubbard model in two dimensions”. In: *Phys. Rev. B* 80 (24 2009), p. 245102.

- [18] Chandan Setty and Philip W. Phillips. “Non-Fermi-liquid behavior from partial nesting in multiorbital superconductors”. In: *Phys. Rev. B* 93 (9 2016), p. 094516.
- [19] Hirokazu Fujiwara et al. “Origins of Thermal Spin Depolarization in Half-Metallic Ferromagnet CrO₂”. In: *Phys. Rev. Lett.* 121 (25 2018), p. 257201.
- [20] Naoto Nagaosa and Jun-ichi Takimoto. “Theory of Neutral-Ionic Transition in Organic Crystals. I. Monte Carlo Simulation of Modified Hubbard Model”. In: *Journal of the Physical Society of Japan* 55.8 (1986), pp. 2735–2744. eprint: <https://doi.org/10.1143/JPSJ.55.2735>.
- [21] T. Egami, S. Ishihara, and M. Tachiki. “Lattice Effect of Strong Electron Correlation: Implication for Ferroelectricity and Superconductivity”. In: *Science* 261.5126 (1993), pp. 1307–1310.
- [22] M. I. Katsnelson et al. “Half-metallic ferromagnets: From band structure to many-body effects”. In: *Rev. Mod. Phys.* 80 (2 2008), pp. 315–378.
- [23] Y. K. Wang, P. H. Lee, and G. Y. Guo. “Half-metallic antiferromagnetic nature of La₂VTcO₆ and La₂VCuO₆ from ab initio calculations”. In: *Phys. Rev. B* 80 (22 2009), p. 224418.
- [24] Onur Erten et al. “Theory of Half-Metallic Ferrimagnetism in Double Perovskites”. In: *Phys. Rev. Lett.* 107 (25 2011), p. 257201.
- [25] Jian Xu et al. “Prediction of room-temperature half-metallicity in layered halide double perovskites”. In: *npj Computational Materials* 5.1 (2019), p. 114. ISSN: 2057-3960.
- [26] Ashis Kundu et al. “New quaternary half-metallic ferromagnets with large Curie temperatures”. In: *Scientific Reports* 7.1 (2017), p. 1803. ISSN: 2045-2322.

- [27] Yi Ren et al. “Half metal phase in the zigzag phosphorene nanoribbon”. In: *Scientific Reports* 8.1 (2018), p. 2932. ISSN: 2045-2322.
- [28] S. Chaudhuri et al. “Half metallicity in Cr substituted Fe₂TiSn”. In: *Scientific Reports* 11.1 (2021), p. 524. ISSN: 2045-2322.
- [29] Arqum Hashmi et al. “Ising ferromagnetism and robust half-metallicity in two-dimensional honeycomb-kagome Cr₂O₃ layer”. In: *npj 2D Materials and Applications* 4.1 (2020), p. 39. ISSN: 2397-7132.
- [30] Yung-mau Nie and Xiao Hu. “Possible Half Metallic Antiferromagnet in a Hole-Doped Perovskite Cuprate Predicted By First-Principles Calculations”. In: *Phys. Rev. Lett.* 100 (11 2008), p. 117203.
- [31] Georg M. Müller et al. “Spin polarization in half-metals probed by femtosecond spin excitation”. In: *Nature Materials* 8.1 (2009), pp. 56–61. ISSN: 1476-4660.
- [32] M. Jourdan et al. “Direct observation of half-metallicity in the Heusler compound Co₂MnSi”. In: *Nature Communications* 5.1 (2014), p. 3974. ISSN: 2041-1723.
- [33] M. Battiato et al. “Distinctive Picosecond Spin Polarization Dynamics in Bulk Half Metals”. In: *Phys. Rev. Lett.* 121 (7 2018), p. 077205.
- [34] “Special Delivery”. In: *Science* 299.5607 (2003), pp. 627–627.
- [35] Elbio Dagotto and Gonzalo Alvarez. “Nanoscale phase separation and colossal magnetoresistance : the physics of manganites and related compounds”. In: 2003.
- [36] D. Ködderitzsch et al. “Vacancy-induced half-metallicity in MnO and NiO”. In: *Phys. Rev. B* 68 (12 2003), p. 125114.

- [37] E. J. Kan et al. “Prediction for room-temperature half-metallic ferromagnetism in the half-fluorinated single layers of BN and ZnO”. In: *Applied Physics Letters* 97.12 (2010), p. 122503. eprint: <https://doi.org/10.1063/1.3491416>.
- [38] Min Wu et al. “A first-principles study of the effect of vacancy defects on the electronic structures of greigite (Fe₃S₄)”. In: *Scientific Reports* 8.1 (2018), p. 11408. ISSN: 2045-2322.
- [39] L. Chioncel et al. “Nonquasiparticle states in the half-metallic ferromagnet NiMnSb”. In: *Phys. Rev. B* 68 (14 2003), p. 144425.
- [40] Piers Coleman. *Introduction to Many-Body Physics*. Cambridge University Press, 2015.
- [41] Lev P. Pitaevskii. “ZERO SOUND IN LIQUID He₃”. In: *Soviet Physics Uspekhi* 10.1 (1967), pp. 100–101. ISSN: 0038-5670.
- [42] H. Q. Lin and J. E. Hirsch. “Two-dimensional Hubbard model with nearest- and next-nearest-neighbor hopping”. In: *Phys. Rev. B* 35 (7 1987), pp. 3359–3368.
- [43] Luca F. Tocchio et al. “Role of backflow correlations for the nonmagnetic phase of the $t-t'$ Hubbard model”. In: *Phys. Rev. B* 78 (4 2008), p. 041101.
- [44] Andriy H. Nevidomskyy et al. “Magnetism and d -wave superconductivity on the half-filled square lattice with frustration”. In: *Phys. Rev. B* 77 (6 2008), p. 064427.
- [45] Hisatoshi Yokoyama, Masao Ogata, and Yukio Tanaka. “Mott Transitions and d -Wave Superconductivity in Half-Filled-Band Hubbard Model on Square Lattice with Geometric Frustration”. In: *Journal of the Physical Society of Japan* 75.11 (2006), p. 114706. eprint: <https://doi.org/10.1143/JPSJ.75.114706>.

-
- [46] L. Fratino et al. “Effects of interaction strength, doping, and frustration on the antiferromagnetic phase of the two-dimensional Hubbard model”. In: *Phys. Rev. B* 96 (24 2017), p. 241109.
- [47] Soumen Bag, Arti Garg, and H. R. Krishnamurthy. “Correlation driven metallic and half-metallic phases in a band insulator”. In: *Phys. Rev. B* 103 (15 2021), p. 155132.
- [48] Arti Garg, H. R. Krishnamurthy, and Mohit Randeria. “Can Correlations Drive a Band Insulator Metallic?” In: *Phys. Rev. Lett.* 97 (4 2006), p. 046403.
- [49] N. Paris et al. “Quantum Monte Carlo Study of an Interaction-Driven Band-Insulator-to-Metal Transition”. In: *Phys. Rev. Lett.* 98 (4 2007), p. 046403.
- [50] S. S. Kancharla and E. Dagotto. “Correlated Insulated Phase Suggests Bond Order between Band and Mott Insulators in Two Dimensions”. In: *Phys. Rev. Lett.* 98 (1 2007), p. 016402.
- [51] Soumen Bag, Arti Garg, and H. R. Krishnamurthy. “Phase diagram of the half-filled ionic Hubbard model”. In: *Phys. Rev. B* 91 (23 2015), p. 235108.
- [52] Arti Garg, H. R. Krishnamurthy, and Mohit Randeria. “Doping a Correlated Band Insulator: A New Route to Half-Metallic Behavior”. In: *Phys. Rev. Lett.* 112 (10 2014), p. 106406.
- [53] Elbio Dagotto. “Correlated electrons in high-temperature superconductors”. In: *Rev. Mod. Phys.* 66 (3 1994), pp. 763–840.
- [54] N. M. Plakida. “Theory of antiferromagnetic pairing in cuprate superconductors (Review article)”. In: *Low Temperature Physics* 32.4 (2006), pp. 363–374.
- [55] Takeshi Aimi and Masatoshi Imada. “Does Simple Two-Dimensional Hubbard Model Account for High-Tc Superconductivity in Copper Oxides?” In: *Journal of the Physical Society of Japan* 76.11 (2007), p. 113708. ISSN: 1347-4073.

-
- [56] T Yanagisawa. “Physics of the Hubbard model and high temperature superconductivity”. In: *Journal of Physics: Conference Series* 108 (2008), p. 012010.
- [57] X. Y. Zhang, M. J. Rozenberg, and G. Kotliar. “Mott transition in the $d=\infty$ Hubbard model at zero temperature”. In: *Phys. Rev. Lett.* 70 (11 1993), pp. 1666–1669.
- [58] Marcelo J. Rozenberg, R. Chitra, and Gabriel Kotliar. “Finite Temperature Mott Transition in the Hubbard Model in Infinite Dimensions”. In: *Phys. Rev. Lett.* 83 (17 1999), pp. 3498–3501.
- [59] Z. B. Huang, H. Q. Lin, and J. E. Gubernatis. “Quantum Monte Carlo study of Spin, Charge, and Pairing correlations in the $t - t' - U$ Hubbard model”. In: *Phys. Rev. B* 64 (20 2001), p. 205101.
- [60] H. Q. Lin and J. E. Hirsch. “Two-dimensional Hubbard model with nearest- and next-nearest-neighbor hopping”. In: *Phys. Rev. B* 35 (7 1987), pp. 3359–3368.
- [61] Evgeny Mikheev et al. “Tuning bad metal and non-Fermi liquid behavior in a Mott material: Rare-earth nickelate thin films”. In: *Science Advances* 1.10 (2015).
- [62] Jian Liu et al. “Heterointerface engineered electronic and magnetic phases of NdNiO₃ thin films”. In: *Nature Communications* 4 (2013), p. 2714.
- [63] V. Eswara Phanindra, Piyush Agarwal, and D. S. Rana. “Terahertz spectroscopic evidence of non-Fermi-liquid-like behavior in structurally modulated PrNiO₃ thin films”. In: *Phys. Rev. Materials* 2 (1 2018), p. 015001.
- [64] Elias Lahoud et al. “Emergence of a Novel Pseudogap Metallic State in a Disordered 2D Mott Insulator”. In: *Phys. Rev. Lett.* 112 (20 2014), p. 206402.
- [65] J M Zhang and R X Dong. “Exact diagonalization: the Bose–Hubbard model as an example”. In: *European Journal of Physics* 31.3 (2010), pp. 591–602.

- [66] S. A. Jafari. *Introduction to Hubbard Model and Exact Diagonalization*. 2008. arXiv: [0807.4878](https://arxiv.org/abs/0807.4878) [[cond-mat.str-el](#)].
- [67] Federico Becca, Alberto Parola, and Sandro Sorella. “Ground-state properties of the Hubbard model by Lanczos diagonalizations”. In: *Phys. Rev. B* **61** (24 2000), R16287–R16290.
- [68] P. W. Leung and Paul E. Oppenheimer. “Implementation of the Lanczos algorithm for the Hubbard model on the Connection Machine system”. In: *Computers in Physics* **6.6** (1992), pp. 603–609. eprint: <https://aip.scitation.org/doi/pdf/10.1063/1.168440>.
- [69] T. D. Kühner and H. Monien. “Phases of the one-dimensional Bose-Hubbard model”. In: *Phys. Rev. B* **58** (22 1998), R14741–R14744.
- [70] Jordan Venderley and E. A. Kim. “A DMRG Study of Superconductivity in the Triangular Lattice Hubbard Model”. In: *arXiv e-prints*, arXiv:1901.11034 (Jan. 2019), arXiv:1901.11034. arXiv: [1901.11034](https://arxiv.org/abs/1901.11034) [[cond-mat.supr-con](#)].
- [71] Z. B. Huang, H. Q. Lin, and J. E. Gubernatis. “Quantum Monte Carlo study of Spin, Charge, and Pairing correlations in the $t - t' - U$ Hubbard model”. In: *Phys. Rev. B* **64** (20 2001), p. 205101.
- [72] Ichiya Sadakata. “A Variational Method to the Hubbard Model”. In: *Journal of the Physical Society of Japan* **42.6** (1977), pp. 1810–1815. eprint: <https://doi.org/10.1143/JPSJ.42.1810>.
- [73] Federico Becca, Luca F Tocchio, and Sandro Sorella. “Metal-insulator transition and strong-coupling spin liquid in the $t-t'$ Hubbard model”. In: *Journal of Physics: Conference Series* **145.1** (2009), p. 012016.
- [74] R. Chitra and G. Kotliar. “Dynamical Mean Field Theory of the Antiferromagnetic Metal to Antiferromagnetic Insulator Transition”. In: *Phys. Rev. Lett.* **83** (12 1999), pp. 2386–2389.

-
- [75] Philipp Werner et al. “Momentum-selective metal-insulator transition in the two-dimensional Hubbard model: An 8-site dynamical cluster approximation study”. In: *Phys. Rev. B* 80 (4 2009), p. 045120.
- [76] M. Ferrero et al. “Valence bond dynamical mean-field theory of doped Mott insulators with nodal/antinodal differentiation”. In: *EPL (Europhysics Letters)* 85.5 (2009), p. 57009.
- [77] A. Liebsch, H. Ishida, and J. Merino. “Multisite versus multiorbital Coulomb correlations studied within finite-temperature exact diagonalization dynamical mean-field theory”. In: *Phys. Rev. B* 78 (16 2008), p. 165123.
- [78] Imseok Yang, Ekkehard Lange, and Gabriel Kotliar. “Impact of magnetic frustration on the Mott transition within a slave-boson mean-field theory”. In: *Phys. Rev. B* 61 (4 2000), pp. 2521–2524.
- [79] Manuela Capello et al. “Variational Description of Mott Insulators”. In: *Phys. Rev. Lett.* 94 (2 2005), p. 026406.
- [80] Gidopoulos, N., Sorella, S., and Tosatti, E. “Born effective charge reversal and metallic threshold state at a band insulator-Mott insulator transition”. In: *Eur. Phys. J. B* 14.2 (2000), pp. 217–226.
- [81] Arne Neumayr and Walter Metzner. “Renormalized perturbation theory for Fermi systems: Fermi surface deformation and superconductivity in the two-dimensional Hubbard model”. In: *Phys. Rev. B* 67 (3 2003), p. 035112.
- [82] Arno Schindlmayr, Thomas J. Pollehn, and R. W. Godby. “Spectra and total energies from self-consistent many-body perturbation theory”. In: *Phys. Rev. B* 58 (19 1998), pp. 12684–12690.
- [83] Patrick Fazekas. *Lecture Notes on Electron Correlation and Magnetism*. WORLD SCIENTIFIC, 1999. eprint: <https://www.worldscientific.com/doi/pdf/10.1142/2945>.

-
- [84] Antoine Georges et al. “Dynamical mean-field theory of strongly correlated fermion systems and the limit of infinite dimensions”. In: *Rev. Mod. Phys.* 68 (1 1996), pp. 13–125.
- [85] U. Schollwöck. “The density-matrix renormalization group”. In: *Rev. Mod. Phys.* 77 (1 2005), pp. 259–315.
- [86] Adrian E. Feiguin and Steven R. White. “Finite-temperature density matrix renormalization using an enlarged Hilbert space”. In: *Phys. Rev. B* 72 (22 2005), p. 220401.
- [87] C. Karrasch, J. H. Bardarson, and J. E. Moore. “Finite-Temperature Dynamical Density Matrix Renormalization Group and the Drude Weight of Spin-1/2 Chains”. In: *Phys. Rev. Lett.* 108 (22 2012), p. 227206.
- [88] W. M. C. Foulkes et al. “Quantum Monte Carlo simulations of solids”. In: *Rev. Mod. Phys.* 73 (1 2001), pp. 33–83.
- [89] Anamitra Mukherjee et al. “Testing the Monte Carlo–mean field approximation in the one-band Hubbard model”. In: *Phys. Rev. B* 90 (20 2014), p. 205133.
- [90] Anamitra Mukherjee et al. “Parallelized traveling cluster approximation to study numerically spin-fermion models on large lattices”. In: *Phys. Rev. E* 91 (6 2015), p. 063303.
- [91] S. Kumar and P. Majumdar. “A travelling cluster approximation for lattice fermions strongly coupled to classical degrees of freedom”. In: *The European Physical Journal B - Condensed Matter and Complex Systems* 50.4 (2006), pp. 571–579. ISSN: 1434-6036.
- [92] Staudt, R., Dzierzawa, M., and Muramatsu, A. “Phase diagram of the three-dimensional Hubbard model at half filling”. In: *Eur. Phys. J. B* 17.3 (2000), pp. 411–415.

-
- [93] J. Oitmaa and J. A. Henderson. “Large- U expansions for the Hubbard model at $T=0$ ”. In: *Phys. Rev. B* 44 (14 1991), pp. 7433–7436.
- [94] Rajarshi Tiwari and Pinaki Majumdar. *Mott Transition and Glassiness in the Face Centered Cubic Lattice*. 2013. arXiv: [1302.2922 \[cond-mat.str-el\]](#).
- [95] Anamitra Mukherjee et al. “Orbital selective directional conductor in the two-orbital Hubbard model”. In: *Phys. Rev. B* 93 (8 2016), p. 085144.
- [96] Niravkumar D. Patel et al. “Non-Fermi Liquid Behavior and Continuously Tunable Resistivity Exponents in the Anderson-Hubbard Model at Finite Temperature”. In: *Phys. Rev. Lett.* 119 (8 2017), p. 086601.
- [97] Rajarshi Tiwari and Pinaki Majumdar. *The Crossover from a Bad Metal to a Frustrated Mott Insulator*. 2013. arXiv: [1301.5026 \[cond-mat.str-el\]](#).
- [98] Sabyasachi Tarat and Pinaki Majumdar. “A real space auxiliary field approach to the BCS-BEC crossover”. In: *The European Physical Journal B* 88.3 (2015), p. 68. ISSN: 1434-6036.
- [99] N. D. Mermin and H. Wagner. “Absence of Ferromagnetism or Antiferromagnetism in One- or Two-Dimensional Isotropic Heisenberg Models”. In: *Phys. Rev. Lett.* 17 (22 1966), pp. 1133–1136.
- [100] Thereza Paiva et al. “Fermions in 2D Optical Lattices: Temperature and Entropy Scales for Observing Antiferromagnetism and Superfluidity”. In: *Phys. Rev. Lett.* 104 (6 2010), p. 066406.
- [101] J.-Y. P. Delannoy et al. “Low-energy theory of the $t - t' - t'' - U$ Hubbard model at half-filling: Interaction strengths in cuprate superconductors and an effective spin-only description of La_2CuO_4 ”. In: *Phys. Rev. B* 79 (23 2009), p. 235130.

- [102] Zeng-Qiang Yu and Lan Yin. “Collinear antiferromagnetic state in a two-dimensional Hubbard model at half filling”. In: *Phys. Rev. B* 81 (19 2010), p. 195122.
- [103] R F Bishop et al. “The quantum J_1 – J_1' – J_2 spin-1/2 Heisenberg model: influence of the interchain coupling on the ground-state magnetic ordering in two dimensions”. In: *Journal of Physics: Condensed Matter* 20.25 (2008), p. 255251.
- [104] P. Chandra and B. Douçot. “Possible spin-liquid state at large S for the frustrated square Heisenberg lattice”. In: *Phys. Rev. B* 38 (13 1988), pp. 9335–9338.
- [105] Zhicheng Zhong and Philipp Hansmann. “Band Alignment and Charge Transfer in Complex Oxide Interfaces”. In: *Phys. Rev. X* 7 (1 2017), p. 011023.
- [106] Zhicheng Zhong and Philipp Hansmann. “Band Alignment and Charge Transfer in Complex Oxide Interfaces”. In: *Phys. Rev. X* 7 (1 2017), p. 011023.
- [107] Somia et al. “First-Principles Study of Perovskite Molybdates AMoO_3 ($A = \text{Ca}, \text{Sr}, \text{Ba}$)”. In: *Journal of Electronic Materials* 48.3 (2019), pp. 1730–1739. ISSN: 1543-186X.
- [108] M. Musa Saad H.-E. “First-principles DFT study new series of ruthenates double perovskites Ba_2MRuO_6 with $M = \text{Sc}, \text{Ti}, \text{V}, \text{Cr}, \text{Mn}, \text{Fe}$ and Co ”. In: *Materials Chemistry and Physics* 204 (2018), pp. 350–360. ISSN: 0254-0584.
- [109] Tomohiro Takayama et al. “Spin–Orbit–Entangled Electronic Phases in 4d and 5d Transition-Metal Compounds”. In: *Journal of the Physical Society of Japan* 90.6 (2021), p. 062001. eprint: <https://doi.org/10.7566/JPSJ.90.062001>.

- [110] Otto Mustonen et al. “Magnetic interactions in the $S = 1/2$ square-lattice antiferromagnets $\text{Ba}_2\text{CuTeO}_6$ and Ba_2CuWO_6 : parent phases of a possible spin liquid”. In: *Chem. Commun.* 55 (8 2019), pp. 1132–1135.
- [111] D. D. Sarma et al. “Electronic Structure of $\text{Sr}_2\text{FeMoO}_6$ ”. In: *Phys. Rev. Lett.* 85 (12 2000), pp. 2549–2552.
- [112] Michael L. Agiorgousis et al. “Machine Learning Augmented Discovery of Chalcogenide Double Perovskites for Photovoltaics”. In: *Advanced Theory and Simulations* 3.1 (2020), p. 1900200. eprint: <https://onlinelibrary.wiley.com/doi/pdf/10.1002/adts.201900200>.
- [113] Antoine Georges, Luca de’ Medici, and Jernej Mravlje. “Strong Correlations from Hund’s Coupling”. In: *Annual Review of Condensed Matter Physics* 4.1 (2013), pp. 137–178. eprint: <https://doi.org/10.1146/annurev-conmatphys-020911-125045>.
- [114] Michael Messer et al. “Exploring Competing Density Order in the Ionic Hubbard Model with Ultracold Fermions”. In: *Phys. Rev. Lett.* 115 (11 2015), p. 115303.
- [115] J. Struck et al. “Tunable Gauge Potential for Neutral and Spinless Particles in Driven Optical Lattices”. In: *Phys. Rev. Lett.* 108 (22 2012), p. 225304.
- [116] Daniel Greif et al. “Short-Range Quantum Magnetism of Ultracold Fermions in an Optical Lattice”. In: *Science* 340.6138 (2013), pp. 1307–1310.
- [117] Anton Mazurenko et al. “A cold-atom Fermi-Hubbard antiferromagnet”. In: *Nature* 545.7655 (2017), pp. 462–466. ISSN: 0028-0836.
- [118] G. Mahan. *Many Particle Physics*. Kluwer Academic, 1958.